NTNU
Norwegian University of
Science and Technology

In Situ Tensile Testing During Continuous EBSD Mapping of Super Duplex Stainless Steel Containing Sigma Phase

Kim Ronny Elstad

Materials Science and Engineering
Submission date: July 2016
Supervisor: Jarle Hjelen, IMTE
Co-supervisor: Morten Karlsen, IMT
Ida Westermann, IMT

Norwegian University of Science and Technology
Department of Materials Science and Engineering

Preface

The present thesis and experimental work is submitted to the Norwegian University of Science and Technology (NTNU), Department of Materials Science and Engineering and is a part of TMT4905 - Materials Technology, Master's Thesis. The author hope that the presented work will contribute to the field of materials science.

I wish to thank my supervisors Professor Jarle Hjelen, Professor II Morten Karlsen and Associate Professor Ida Westermann that have given me motivation and guidance through this project. For the help with the in situ equipment I would like to thank PhD Candidate Christian Oen Paulsen and Senior Engineer Sergey Khromov. For guidance in the laboratories I would like to thank Senior Engineers Yingda Yu, Trygve Schanche and Wilhelm Dahl. Further I would like to thank Dr. René de Kloe, application specialist at EDAX for help with indexing and analysis after the EBSD acquisition.

Trondheim, July 2016

Kim Ronny Elstad

Abstract

Super duplex stainless steels (SDSS) are materials which comprise an extraordinary combination of mechanical properties, corrosion resistance and relatively low cost. SDSS were developed on the basis for use in the North Sea. However, formation of intermetallic phases e.g. sigma phase in super duplex stainless steels decrease the mechanical properties. The sigma phase grows from the α/γ-interphase and into the ferrite leaving brittle zones depleted of Cr and Mo. This makes the material prone to cracks, fracture or severe corrosion attacks.

The material was characterised both as received and heat treated material containing sigma phase. In regards to index the sigma phase before EBSD characterisation several finalising sample preparation techniques were tested. During in situ deformation continuously electron backscatter diffraction (EBSD) mapping was performed and from this the deformation was investigated. When the material is deformed there is an evolution of orientation gradients in the structure, grain rotation and crack propagation.

The examination of the orientation gradients and grain rotation was performed parallel to the tensile direction. This was done since the individual grains show a reduced rotation tendency in the normal direction while the opposite behaviour is observed in the tensile direction [1]. There is shown that in both the austenite and the ferrite (FCC and BCC) the grain rotation is strongly dependent on the initial orientation of the grains.

In austenite the grains tend to rotate from the [101] direction and towards [$\bar{1}$12] and [111] directions. The opposite behaviour is observed in ferrite. Ferrite tends to rotate against the [101] parallel to the tensile direction. Multiple slip lines were found preferably within the austenite phase in various samples but there were also found slip lines in the ferrite. The slip lines in the ferrite were only found in the base material which did not contain any sigma phase. During this project the crack propagation after the deformation was investigated. There were only found cracks in the sigma phase and not in the ferrite or austenite. Cracking in the material follow a classical brittle behaviour and propagate perpendicular to the tensile direction.

Sammendrag

Super duplex rustfrie stål (SDSS) er metaller som innehar en ekstraordinær kombinasjon av blant annet gode mekaniske egenskaper og korrosjonsbestandighet ved relativt lave kostnader. SDSS ble utviklet for bruk i Nordsjøen. Dannelsen av intermetalliske faser, f.eks sigma i SDSS reduserer de mekaniske egenskapene. Sigmafasen vokser fra α/γ-grenseflaten og inn i ferritten som resulterer i sprø soner utarmet av Cr og Mo. Dette medfører at materialet blir utsatt for sprekkdannelser, brudd eller alvorlige korrosjonsangrep.

Metallet ble karakterisert både i ubehandlet tilstand og i varmebehandlet tilstand med innhold av sigma-fase. I henhold til indekseringen av sigma-fase før EBSD-karakterisering ble flere prøveprepareringsteknikker testet. I løpet av in situ deformasjon ble kontinuerlig EBSD-karakterisering utført, og fra dette ble deformasjonsmekanismen undersøkt. Når materialet deformeres blir det dannet orienteringsgradienter i strukturen, kornrotasjoner og sprekkforplantninger.

Undersøkelsen av kornrotasjonene ble utført parallelt med strekkretningen ettersom nomalretningen viser en redusert tendens til rotasjoner, mens motsatt oppførsel observeres i strekkretningen [1]. Det er vist at kornrotasjonene i henholdsvis austenitt og ferritt (FCC og BCC) er sterkt avhengig av den opprinnelige retningen av kornene.

I austenitt har korn en tendens til å rotere fra [101] mot $[\bar{1}12]$ og [111]. Den motsatte situasjonen kan sees i ferritt. Ferritt har en tendens til å rotere mot [101] parallelt med strekkretningen. Det ble funnet flere sliplinjer, hovedsakelig i austenittfasen, men også noen i ferrit. Sliplinjene i ferrittfasen ble bare funnet i grunnmaterialet som ikke inneholder noe sigmafase. I løpet av dette prosjektet har sprekkforplantning i metallet som følger av deformasjon blitt undersøkt. Det ble funnet sprekker kun i sigmafasen og ikke i ferritt eller austenitt. sprekkdannelser i materialet følger en klassisk sprø karakter og forplanter seg vinkelrett på strekkretningen.

Contents

1 Introduction

Duplex stainless steels (DSS) and super duplex stainless steels (SDSS) are metals which comprise an extraordinary combination of mechanical properties, corrosion resistance and relatively low cost. SDSS were developed on the basis for use in the North Sea. In offshore applications DSS are used in flow lines, process piping systems and equipment like separators, scrubbers and pumps. DSS are also widely used in subsea applications mainly in umbilicals, downhole production tubings, christmas three components, flow lines and pipelines containing corrosive fluids. DSS also play a significant role in architecture where it is necessary to combine corrosion resistance with load bearing strength. Additionally, DSS are commonly used in the desalination industry where the material is exposed to high chloride and high temperature corrosive environments [2].

When metals are used in constructions the deformation behaviour is important, both on a macroscopic and microscopic scale. This is especially important when the material is used offshore in the North Sea. During heat treatment or welding procedures intermetallic phases may occur in the material, e.g. sigma phase. These intermetallic phases change the mechanical properties and deformation behaviour in the steel. To determine the mechanical properties and effect of deformation in these steels EBSD is a powerful characterisation tool. With the combination of fast EBSD pattern acquisition and low engineering strain rate there is a possibility to perform electron backscatter diffraction (EBSD) mapping continuously during tensile testing. Previously this characterisation have been performed ”semi-in-situ” where the process has to be stopped each time an EBSD acquisition is performed. During this process important data may be lost.

The purpose of this work was to characterise SDSS containing sigma phase and its deformation behaviour. The main focus was to perform in situ tensile testing and study the development of orientation gradients and also document the grain rotations. Furthermore, the slip activity and the crack propagation through the metal was also examined.

2 Theoretical background

In this part of the thesis a theoretical background required for discussion of the results is presented. Herein necessary information regarding the base material, sigma phase, deformation behaviour during tensile testing and previous published cases is provided.

2.1 Super duplex stainless steels (SDSS)

Duplex stainless steels (DSS) and super duplex stainless steels (SDSS) are high alloyed steels developed to combine high corrosion resistance, strength and toughness. These material properties come from a microstructure containing approximate equal amounts of austenite (γ) islands embedded in a ferrite (α) matrix. In theory a ferrite matrix gives the material strength and the austenite islands provide ductility. The properties in DSS make the material a good choice in regards to chemical and oil and gas industry. Since DSS exhibit high strength combined with high corrosion resistance, less material can be used that further contribute to weight and cost savings [2].

The mechanical properties vary in DSS and SDSS. An example of the mechanical properties is given in Table 2.1, where $R_{p_{0.2}}$ is the offset yield stress, i.e. the stress at which the material experience 0.2 % permanent plastic elongation. R_M is the ultimate tensile strength (UTS), which is the maximum stress the material can resist before necking and A_5 is the permanent elongation after fracture.

Table 2.1: Overview of the mechanical properties for UNS 32760 (Zeron 100) [3].

Grade	$R_{p_{0.2}}$	R_M	A_5	Brinell hardness
S32760	550	750	25	270

The alloying elements are important in DSS. Chromium is added in stainless steels to promote the formation of a passive film that increases the corrosion resistance. To prevent atmospheric corrosion at least 10.5 wt.% Cr is needed. In DSS a minimum of 20 wt.% Cr is needed. Chromium also changes the phase balance in the steel since it is a ferrite stabiliser that promotes the formation of the body centred cubic (BCC) structure. In Figure 2.1 the transformation between BCC and face centred cubic (FCC) is shown, where two random austenite and ferrite stabilisers are shown as an example. When adding an austenite stabiliser, e.g. nickel, the formation of FCC is promoted. By adding a ferrite stabiliser, e.g. chromium, the formation of BCC is promoted [2].

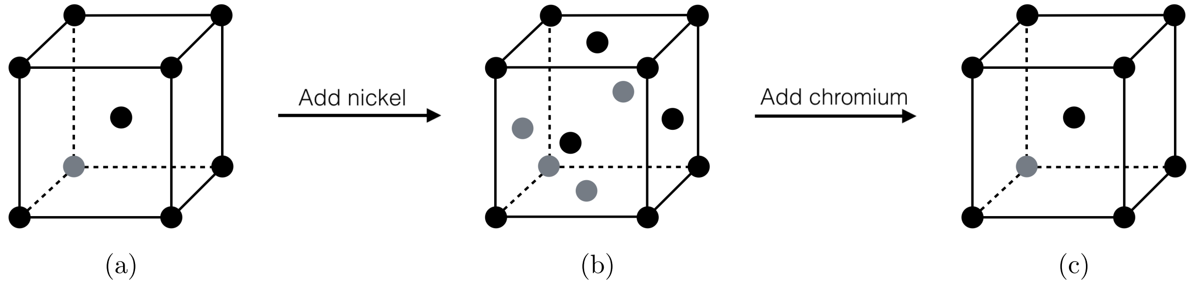

Figure 2.1: Transformation between BCC and FCC by adding austenite and ferrite stabilisers. When starting with BCC structure in (a) and adding austenite stabilisers e.g. Ni, the transformation to FCC occurs in (b). By adding ferrite stabilisers e.g. Cr the unit cell transforms to BCC in (c).

Pitting resistance equivalent number (PREN) is a measure of the resistance against pitting corrosion. The PREN is given in Equation 1 and represents a better pitting resistance with the higher PREN number. Molybdenum is added in DSS in order to increase the resistance of localised corrosion, i.e. pitting and crevice corrosion. From Equation 1 it is shown that molybdenum is three times as effective as chromium for counteracting localised corrosion in chloride containing environments. Molybdenum is, like chromium, a ferrite stabiliser that promotes the formation of ferrite by closing the γ-field in the phase diagram. An illustration showing different effects of the alloying elements in the gamma field is given in Figure 2.2. A disadvantage by adding more molybdenum is formation of intermetallic phases, e.g. sigma (σ) phase [2].

$$PREN = Cr + 3.3 \cdot (Mo + 0.5W) + 16N \tag{1}$$

Nitrogen is an inexpensive alloying element that promotes formation of austenite by expanding the γ-field in the phase diagram (Figure 2.2). Small fractions of nitrogen is added to the material. These additions increase the resistance for pitting and crevice corrosion (see Equation 1) and is one of the most effective solid solution strengthening elements. Nickel is an important alloying element in DSS which promotes the formation of austenite by opening the γ-field (Figure 2.2a) and increases the material's toughness [2].

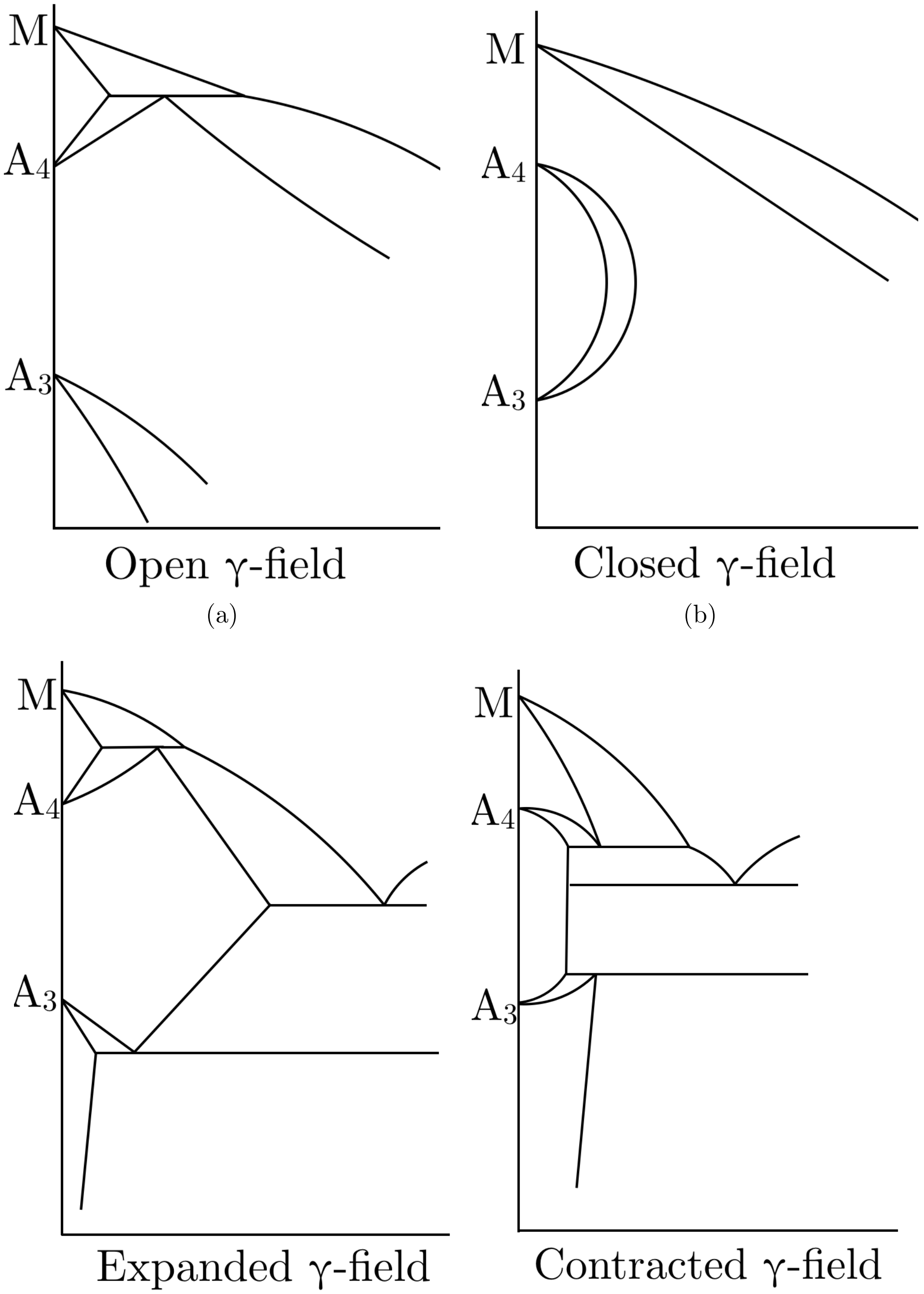

(a) (b)

(c) (d)

Figure 2.2: Illustration of the different effects by adding ferrite and austenite formers where (a) shows an open γ-field, (b) closed γ-field, (c) expanded γ-field and (d) contracted γ-field [4].

The easiest way to achieve a duplex structure is by thermo-mechanical controlled processing (TMCP). A fully ferritic structure is produced, followed by an intercritical annealing in the $\gamma - \alpha$ region. This allows formation of austenite where the temperature, holding time and amount of alloying elements decide the final content of austenite and ferrite. The complexity of the microstructure and the high amount of alloying elements makes the material prone to phase transformation and embrittlement upon heat treatment. The isothermal TTT-diagram in Figure 2.3 shows that the formation of various intermetallic phases occur at a wide range of temperature regimes in a 2205 DSS alloy. The intermetallic phases are harmful to the mechanical properties and lowers the corrosion resistance [5].

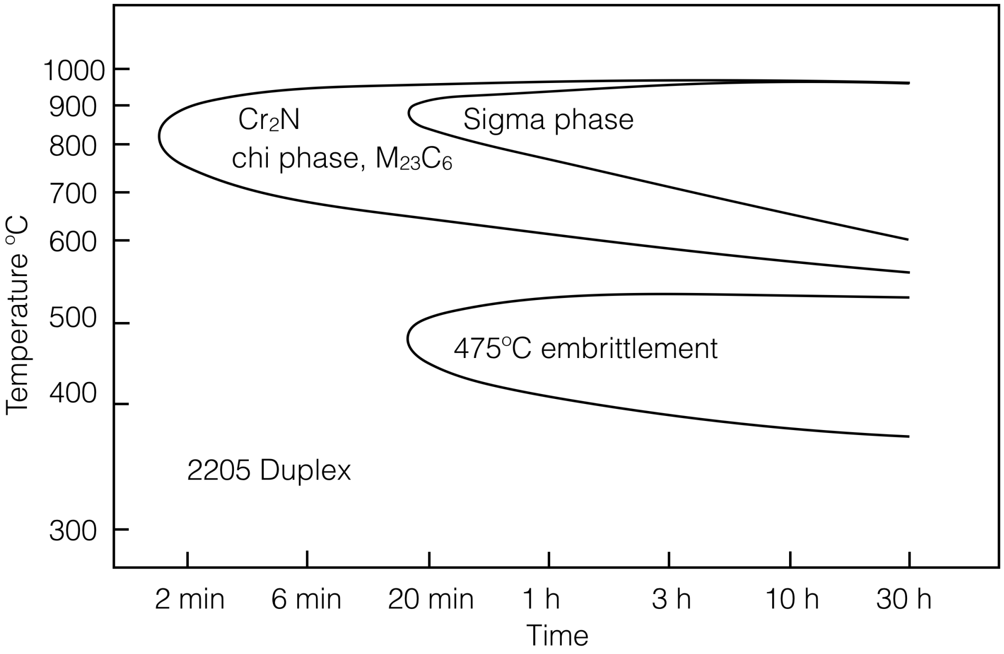

Figure 2.3: Isothermal TTT-diagram for a 2205 DSS alloy [5].

Figure 2.4 shows the effect of different alloying elements on formation of intermetallic phases in DSS. Cr decreases the time needed to precipitate intermetallic phases in the steel. Mo, W and Si change the transformation in two ways, i.e. they increase the transformation temperature and decrease the time needed for precipitation. Cr, Mo, Cu and W all have an effect on precipitating phases at lower temperatures. These alloying elements decrease the transformation time and temperature for π, ϵ and α' phase, where α' is the well known 475 °C embrittlement [6].

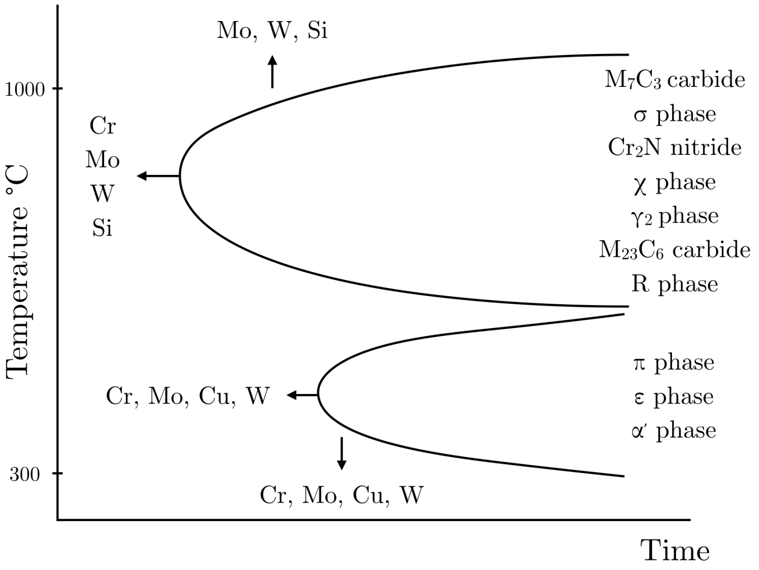

Figure 2.4: Effect of alloying elements on the formation of intermetallic phases [6].

2.1.1 Sigma phase

Heat treatment in the area 600-900 °C promotes the formation of an iron-chrome-molybdenum intermetallic phase, known as the sigma phase. The sigma phase strongly reduces the corrosion resistance due to depletion of chromium and molybdenum in the surrounding areas. Since chromium gives general corrosion resistance and molybdenum gives protection against localised corrosion, the surrounding areas suffer from a substantial reduction in localised corrosion resistance. This intermetallic phase increases the hardness of the steel with a simultaneous decrease in toughness and ductility due to the brittle behaviour of the sigma phase [2].

The crystal data for the sigma phase is given in Table 2.2. In contrast to the regular DSS that consist of FCC and BCC which are cubic, the sigma phase is tetragonal [7].

Table 2.2: Crystal data for sigma phase [7].

Unit formula	Cr_6Fe_7
Pearson symbol	tP30
Structural type	$D8_b$
Space group	$P4_2/mnm$
Unit cell parameters (Å)	8.785 4.579

The formation is illustrated in Figure 2.5. The sigma phase which is rich in chromium and molybdenum, starts its formation preferably at the interface between the austenite and the ferrite (Figure 2.5a). Initially, the formation the sigma phase grows from areas in the ferrite phase with high Cr-concentrations. Further, the sigma will continue to grow into the ferrite leaving zones depleted of chromium and molybdenum as shown in Figure 2.5b [8].

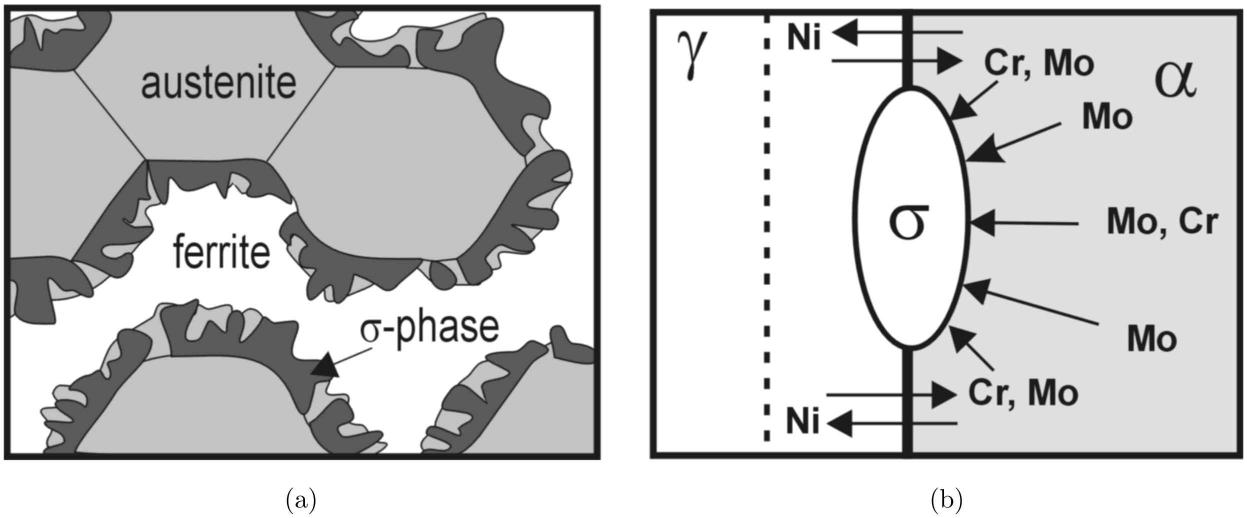

(a) (b)

Figure 2.5: Formation of sigma phase at ferrite and austenite interface in (a), (b) shows the distribution of alloying elements during the formation of sigma phase [9].

In addition to sigma phase formation there is also formed a small fraction of secondary austenite. In addition to direct transformation from ferrite to austenite the secondary austenite transformation also occurs by an eutectoid reaction as shown in Equation 2. This eutectoid reaction typically occurs in the temperature range 700-900 °C. The secondary austenite has been found to contain small levels of chromium [10].

$$\alpha \rightarrow \sigma + \gamma \tag{2}$$

From an investigation by Pohl et al. [11] it has been shown that the morphology of sigma phase changes at different annealing temperatures. They described the morphology as coral-like at 750 °C, see Figure 2.6c. At higher temperatures the sigma phase becomes larger and more compact, as shown in Figure 2.6a.

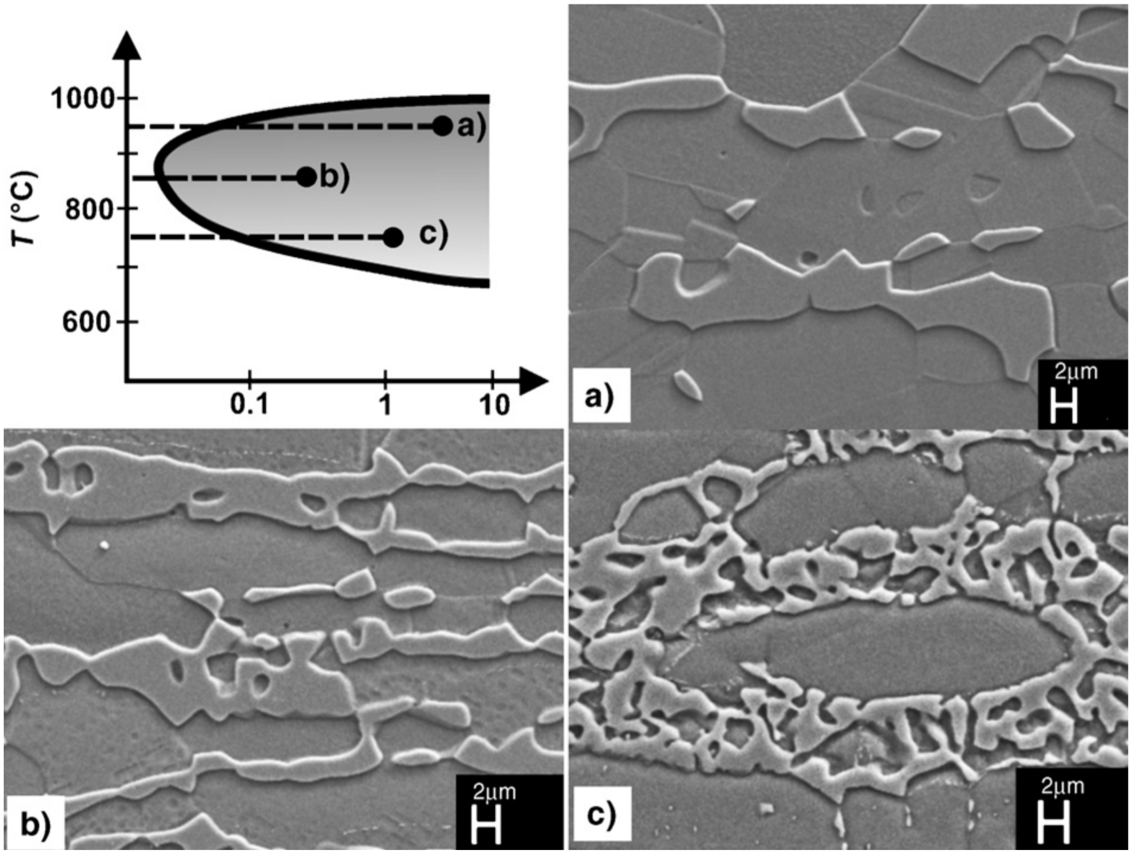

Figure 2.6: Different morphologies of sigma phase at different annealing temperatures [11].

Several studies performed on austenitic stainless steels have concluded that the formation of sigma phase depends heavily on grain size and grain shape [12]. As the grain size decreases the density of nucleation sites for sigma increase since there is a larger total grain boundary area for the sigma phase to grow from [13]. Sato et al. [14] have concluded that the formation of sigma phase in DSS greatly depends on the crystallographic misorientation between austenite and ferrite. They also concluded that a coherent interface between austenite and ferrite may suppress and delay sigma phase formation. Materials containing sigma phase can be more prone to cleavage fracture and cracking. Investigations by Børvik et al. [15] have shown a reduction in fracture strain with increasing levels of sigma phase inn a DSS 2205 (UNS S31803). Already at 1 vol.% sigma phase the material has lost most of its impact toughness shown by Charpy impact testing. There has also been reported that an amount of 0.5 vol.% sigma phase in DSS has caused a reduction of the impact toughness of 50 %.

2.1.2 Mechanical properties

Mechanical properties are very important when choosing a steel for its application. These mechanical properties are ascertained by performing examinations in simulated environments. A standard stress-strain test is tensile testing, also called tension testing, see Figure 2.7. The tensile test exercises a uniaxial tensile force on each side of the specimen until fracture. Tensile testing can give measures of important material properties such as ultimate tensile strength, elongation to fracture and reduction in area. From these properties Young's modulus, Poisson's ratio, yield strength and strain-hardening characteristics can be calculated and determined [16].

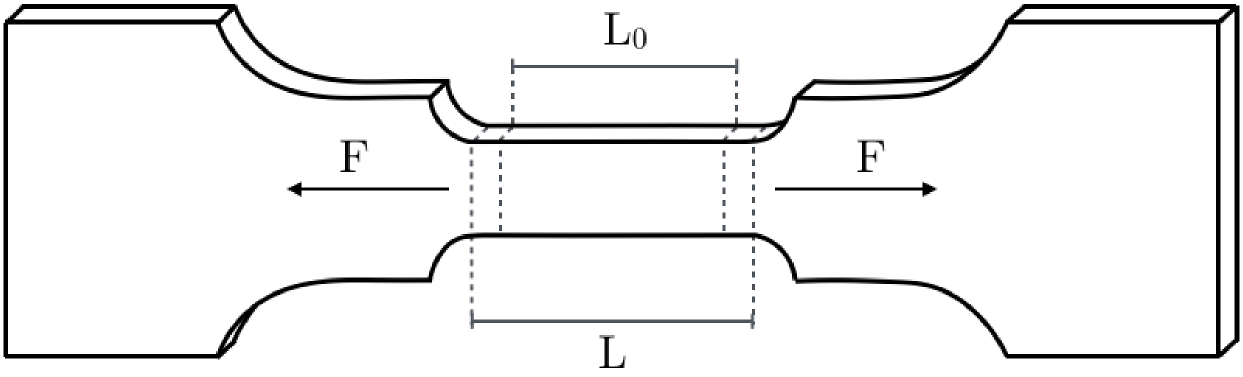

Figure 2.7: Illustration of the well known tensile test.

Slip is an important factor that occurs during dislocation movement and lead to plastic deformation of materials. Dislocations is a crystal defect that occurs during e.g. solidification. There are two common kinds of dislocations, respectively edge- and screw-dislocations, see Figures 2.8 and 2.9. Edge dislocations have an extra half plane introduced in the crystal, see Figure 2.8. The edge dislocations are represented by the symbol $\perp$ which indicates the position of the dislocation line. When a force is applied dislocation movement will occur, see Figures 2.8b and 2.8c. When multiple dislocations move, the material will experience plastic deformation [16].

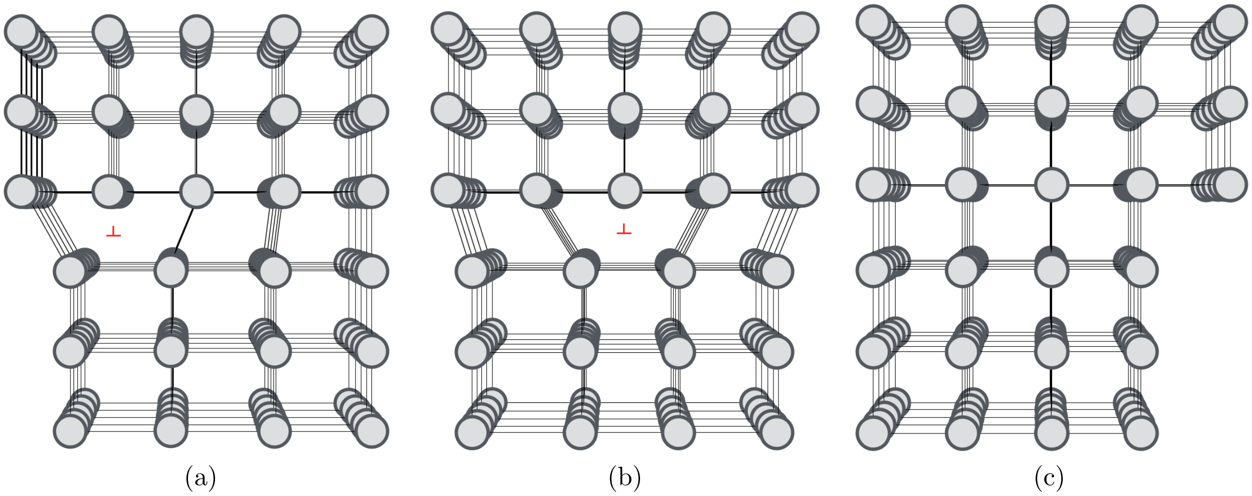
(a) (b) (c)

Figure 2.8: Edge dislocation with movement of the dislocation line in (b) and (c) [16].

The screw dislocation is illustrated in Figure 2.9. The screw dislocation is similar to the edge dislocation, but the screw dislocation line moves normal to the direction of the applied stress while the edge dislocation line moves in the same direction as the stress. With the screw dislocation the distortion is one atomic distance relative to the slip plane [17].

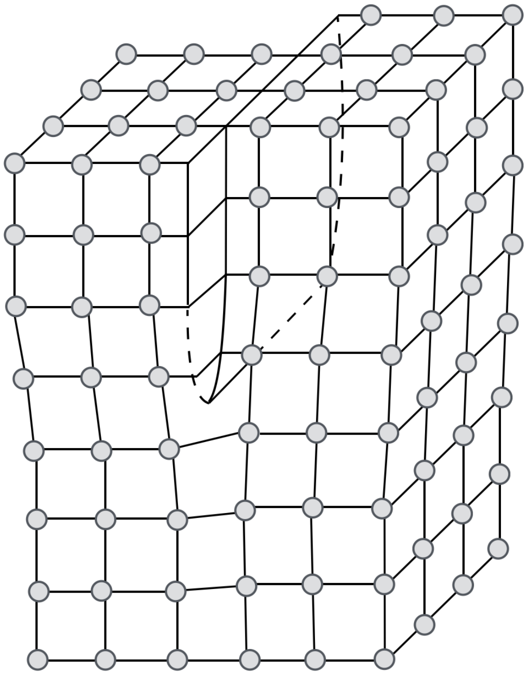

Figure 2.9: Illustration of a screw dislocation [16].

Different crystal structures have different slip systems which include slip planes and slip directions. A slip plane is the plane in which the atoms are most dense packed. The slip direction is the direction in the slip plane where the atoms are most densely packed. DSS consist of austenite (FCC) and ferrite (BCC). FCC can have slip in the $\{111\}$ planes and with $\langle 1\bar{1}0\rangle$ family of directions which correspond to 12 slip systems, see Figure 2.10. The BCC on the other hand, is more complex. BCC contains three slip planes: $\{110\}$, $\{211\}$ and $\{321\}$. Each slip plane exhibits a family of $\langle\bar{1}11\rangle$ directions which correspond to 12, 12 and 24 slip systems, respectively, i.e. 48 slip systems. With the BCC crystal structure, some of the slip systems will only be operable at elevated temperatures [16].

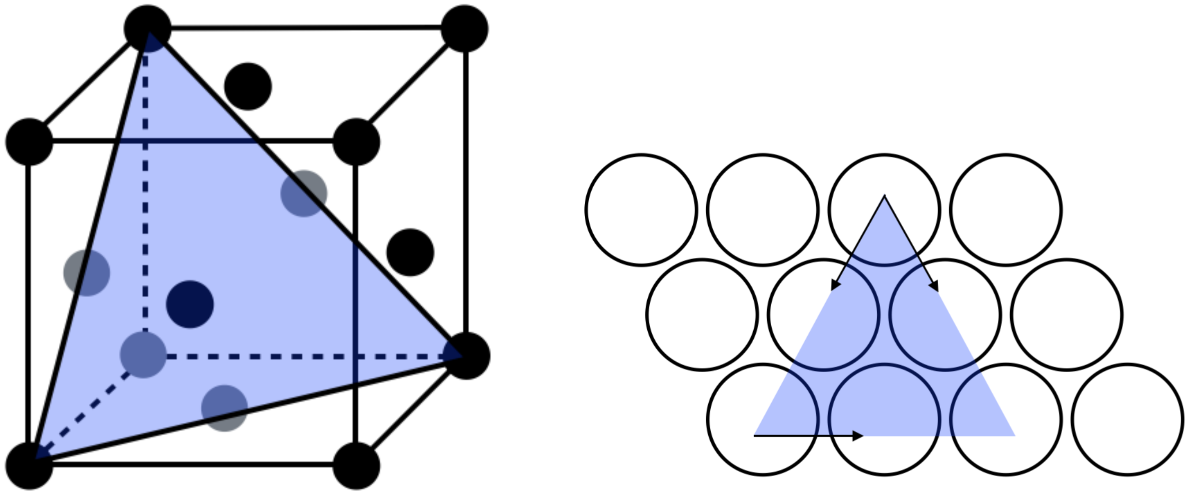

(a) (b)

Figure 2.10: FCC crystal structure with the $\{111\}$ plane in (a) and the same plane in (b) showing the possible slip systems [16].

Previous investigations have shown that dislocations can be activated in ferrite by local shear stresses generated by dislocation pile ups on the austenite phase boundary. There was also concluded that when dislocations accumulate on the austenite grain boundaries, shear may occur in the ferrite phase [18].

2.2 Texture

Crystallographic orientation refers to the orientation of the crystal lattice with respect to a reference frame. Crystallographic orientation is rarely randomly distributed but almost always possesses some degree of preferred orientation, i.e. texture. Texture is the study of the distribution of crystallographic orientation in a polycrystalline material [19]. The texture in the material strongly influences the material's mechanical properties, e.g. yield strength, ductility and transformation strain. When the material is deformed, e.g. by tensile testing, the texture of the material changes. The degree of deformation and deformation mechanism decides the texture, e.g. a high degree of deformation will increase the texture, and vice versa [20].

As known from section 2.1.2, plastic deformation mainly occurs by slip and is more predominant in the FCC than in BCC structures since FCC is more densely packed, i.e. more operable slip systems. During plastic deformation the grains rotate with increasing deformation, i.e. the degree of misorientation between the crystals increase [20]. Grain rotation can be simplified by applying an illustration of a single crystal (Figure 2.11). In the figure a single crystal is deformed, and during the tensile deformation the crystal will gradually rotate from the slip direction towards the tensile direction. Figure 2.11a shows the undeformed crystal. When this crystal is deformed with some lateral movement the specimen will be deformed as shown in Figure 2.11b. However, there is no lateral movement which cause rotation and bending of the lattice [21].

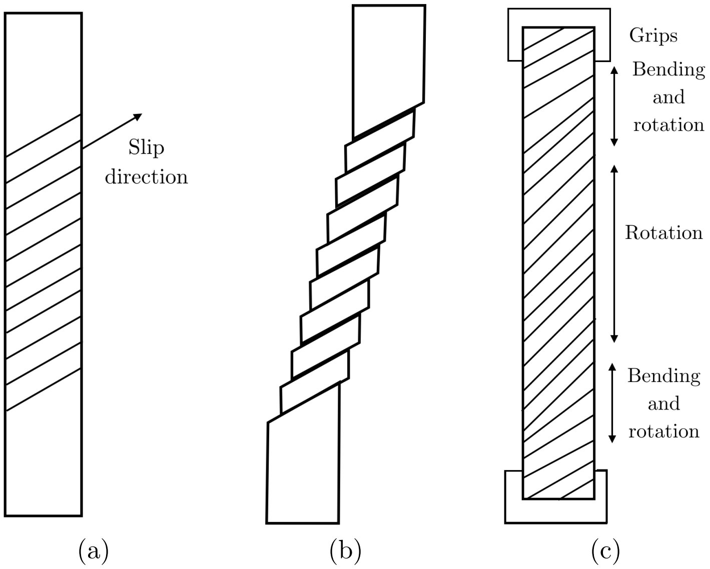

Figure 2.11: Illustration of the rotation behaviour in a single crystal where an undeformed crystal gets deformed with lateral movement in (b) and no lateral movement in (c) [21].

Deformation of a polycrystalline material is more complex since each crystal is surrounded by neighbouring crystals. Since the crystal is dependent on the deformation of its neighbouring crystals the lattice rotations are no longer uniform [1]. Han et al. [1] concluded that in polycrystalline aluminium (FCC structure) there were no tendencies of rotation in the normal plane direction. They also concluded that the grain rotations were dependent on the initial orientation in the tensile direction [1]. Bjerkaas [21] performed in situ tensile testing of an Al-Mg-Si alloy and concluded that grains having an [101] orientation parallel to the tensile direction rotate more than three times as much as [111] and [001].

Han et al. [1] have also shown that grains have a tendency to rotate against preferred directions during deformation in the tensile direction. Figure 2.12 shows the theoretical rotation in a single FCC crystal (Figure 2.12a) and experimental investigation done by Han et al. (Figure 2.12b). From the theoretical rotation the grain rotation is directed towards [$\bar{1}$12] and [$\bar{1}$11]. Investigations from Han et al. also showed the same tendency where the grains rotated from [101] towards [111] and [$\bar{1}$12]. In addition, close to the [001] direction the orientation rotation hardly changes during deformation. This is also supported by Bjerkaas [21] where the grains rotated from [101] and towards [111] and [$\bar{1}$12]. However, these investigations show more tendency to rotate in the [001] direction, mainly towards the pole of the inverse pole figure.

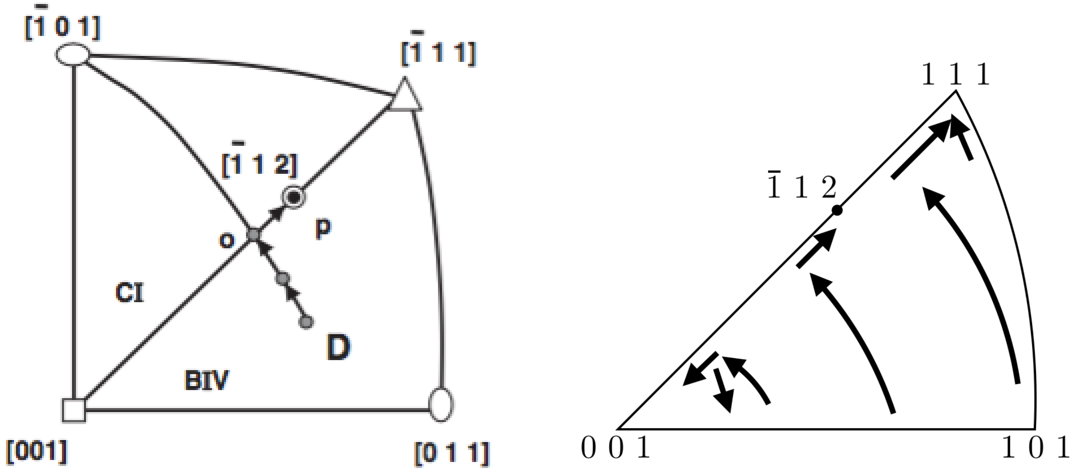

(a) (b)

Figure 2.12: Illustration of the grain rotation in an FCC single crystal (a) and (b) investigations by Han et al. performed on aluminium alloy 1050 [1].

During deformation the misorientation within the crystal changes, i.e. formation of crystallite structure in the deformed grains. With further deformation a subgrain structure is developed. If the deformation process proceeds, the misorientation differences inside these crystallites increase and high angle grain boundaries may form. The misorientation within the grains occurs as a result of the distortion differences inside each grain, i.e. heterogeneous strains [22]. Heterogeneous strains can be enhanced by crystallographic texture, grain size and shape and second phase particles. Bjerkaas [21] showed how heterogeneous strains affect the deformation of grains. This investigation was carried out on an aluminium alloy 6063. The alloy consisted of both soft and hard grains where the first mentioned grain activates more slip system while the latter provides less. From these investigations it became clear that the soft grains had to compensate for the hard grains which predominantly resulted in deformation of soft grains.

2.3 Electron backscatter diffraction

Electron backscatter diffraction (EBSD) is a characterisation technique used to determine crystallographic orientation in a material using a scanning electron microscope (SEM). As shown in Figure 2.13 a stationary electron beam is focused on a crystalline specimen and backscattered diffracted electrons interact with the crystal structure close to the surface, about 20 nm. An elastic spread of electrons occurs which makes the primary electrons change direction and the energy loss is negligible [23].

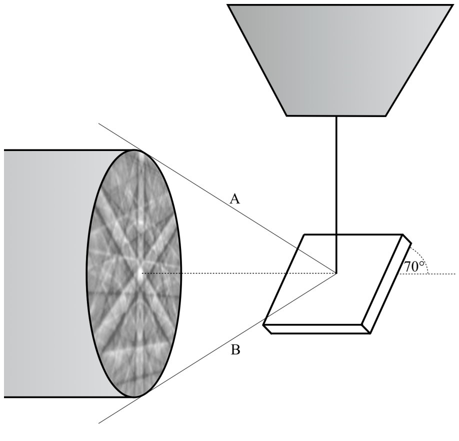

Figure 2.13: Principle of EBSD [23].

Since it is desirable that the interactions occur close to the surface, the specimen is tilted 70°. When the specimen's tilt angle is less than 70° relative to the incident beam, the amount of backscatter electrons will decrease. This is shown by a schematic drawing in Figure 2.14, where a larger tilt angle creates more interactions closer to the surface and by that eliminates the channeling effect [23].

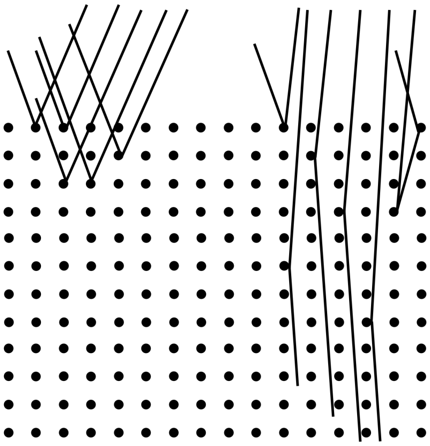

Figure 2.14: Schematic illustration of the effect of tilt angle [24].

Probe current is of great importance when deciding the amount of secondary and backscatter electrons emitted. The probe current can be calculated from Equation 3 [24].

$$i_p = \delta \cdot i_p + \eta \cdot i_p + i_{AE} \tag{3}$$

In the equation, δ and η is the fraction of secondary and backscatter electrons and i_{AE} is the absorbed current. While the fraction of secondary electrons is estimated to be 0.1, the fraction of backscatter electrons changes with the alloy composition and can be calculated by applying Equation 4 [24].

$$\eta = -0.0254 + 0,016 \cdot Z - 1.86 \cdot 10^{-4} \cdot Z^2 + 8.3 \cdot 10^{-7} \cdot Z^3 \tag{4}$$

Where Z is the atom number of the specimen. Using the atom number for SDSS and combining Equations 3 and 4, Equation 5 can be applied to determine the probe current [24].

$$i_p = 0.1 \cdot i_{AE} + 0.26 \cdot i_{AE} + i_{AE} = 1.36 \cdot i_{AE} \tag{5}$$

The electrons are diffracted according to the Bragg's law of diffraction as shown in Equation 6. An electron backscatter pattern (EBSP) is formed on a fluorescent phosphor screen. An EBSP consists of bright bands, referred to as Kikuchi bands that is captured by a charge-couple device (CCD) camera [23].

$$n \cdot \lambda = 2 \cdot d \cdot \sin(\theta_b) \tag{6}$$

In the equation, n is a integer, λ is the wavelength, d is the interplanar spacing and θ_b is the Bragg-angle, see Figure 2.15 [25].

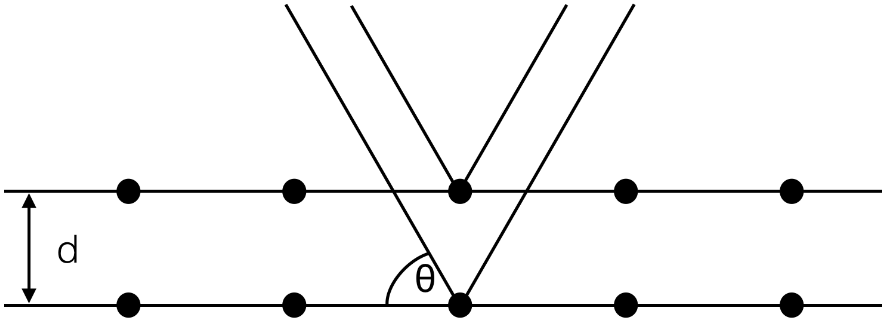

Figure 2.15: Illustration of Bragg diffraction [23].

Figure 2.16 shows an more detailed illustration of the formation of an EBSP. An electron beam is emitted on the diffraction plane and cones of intense electrons are emitted. These cones have an angle of 180° - $2\theta_b$ and are the edges of the Kikuchi bands. The plane in the centre of the cones are the projection of the diffracting plane on to the phosphor screen [26].

By indexing these diffraction patterns the crystal structure and orientations can be obtained. The bands correspond to the crystal plane (hkl) with a width corresponding to the interplanar spacing (d_{hkl}). The angle between each band represents the angle between the respective planes. Additionally the intersection between the bands is an intersection between planes (zone axis). The position of the bands equals the crystallographic orientation [26].

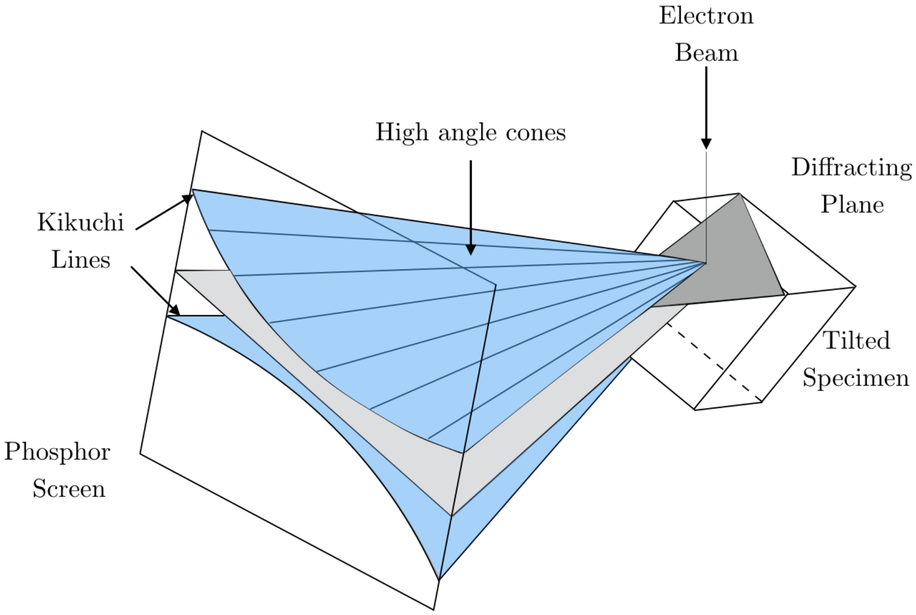

Figure 2.16: Formation of an EBSP [23].

2.3.1 Indexing diffraction patterns

When indexing diffraction patterns the Hough transformation is important. Since the human eye easily can see and recognise lines but which is a difficult task for computers, the Hough transformation is used. In the Hough transformation the lines in the diffraction pattern are transformed to pixels in the Hough space. Each pixel (x_i,y_i) in the Hough space is parameterised with the coordinates ρ and α and transformed to a sinus curve, see Equation 7 [19].

$$\rho(\alpha) = x_i \cos(\alpha) + y_i \sin(\alpha) \tag{7}$$

If ρ is plotted as a function of α for every pixel (x_i,y_i) it is possible to achieve series of sinus curves that all have the same intersection point, see Figure 2.17a. The intersection point will be shown as bright points on a dark matrix. These point can be detected and will have a distance ρ from origo with an angle θ_b. Further, the points can be transformed back to lines in the diffraction patterns, see Figure 2.17b [23].

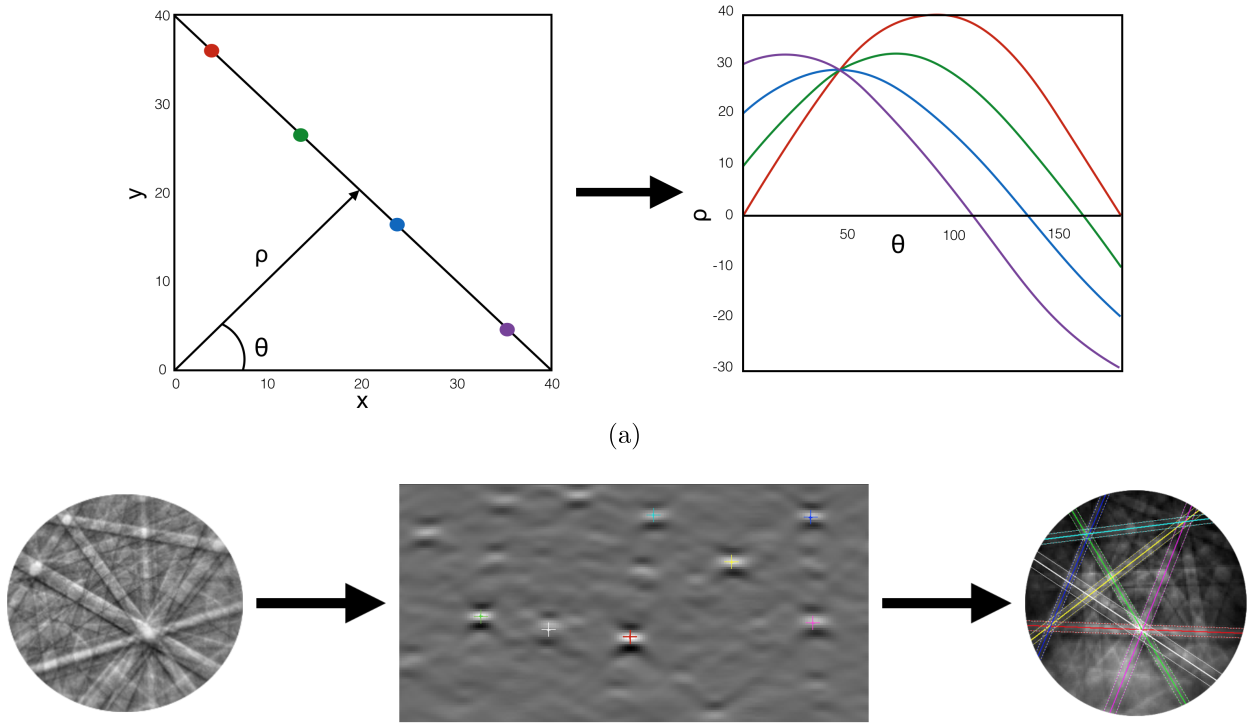

(a)

(b)

Figure 2.17: Illustration of the Hough transformation where (a) the straight lines are parameterised to a set of sinus curves and (b) the transformation from lines to points in the Hough space occurs where the tops in intensity is transformed back to lines [25].

Confidence index (CI) is defined by Equation 8 and is a measure of the reliability of the indexed crystal orientation [27].

$$CI = \frac{V_1 - V_2}{V_{Tot}} \tag{8}$$

Where V_1 and V_2 is the best and the next best solution, respectively and V_{tot} is the total number of solutions. The CI value varies between 0 and 1, where the increasing value gives an increase in the probability for correct indexed pattern. Image quality (IQ) map is a grayscale map which gives an indication of the quality of the indexed pattern. The IQ maps describe the quality by varying the contrast in the picture, where the quality increases with increasing brightness. To present data, inverse pole figure (IPF) maps are used. These maps represent the orientation of the grains, which generally is perpendicular to the plane and is referred to as an IPF, where colours represent the different orientations [28].

When indexing diffraction patterns the Hough settings are important. These settings affect both the speed and quality of the indexing. The binned pattern size and theta step size changes the indexing time but may increase the indexing quality. The binned pattern size change the pixel density. Lowered binned pattern size gives shorter indexing time but can give negative results on the indexing quality. The theta step size changes the angular spacing of the Hough transformation. If the theta step size is increased, the indexing time will be reduced and the indexing quality can be affected in a negative manner [27].

The peak count can be useful for some crystal structures. Usually a minimum value is used, but the max peak count can be adjusted, e.g. if the crystal structure is tetragonal, monoclinic etc. The maximum peak count allows more bands to be detected. The minimum peak magnitude sets a tolerance of the height between the detected peaks. A low minimum peak magnitude means that more of the points in the Hough transformation are detectable [27].

The peak distance defines the minimum distance among the peaks. If one peak is detected, the remaining peaks at a certain distance given in pixels are ignored. Another peak setting that can be done is the peak symmetry. The peak symmetry decides how symmetric a peak need to be. The classic Hough type utilises a convolution mask to emphasise peaks. The convolution mask depends greatly on the band width of the diffraction pattern. Increasing the convolution mask will increase the indexing time. It is recommended to increase the convolution mask for wider bands, and decrease for more narrow bands [27].

2.3.2 Cleanup

The patterns acquired may need some processing. Usually the pattern indexing is quite effective but when the patterns are of a low quality, one or several cleanup procedures may be necessary. This can be at for example at grain boundaries where the patterns are made up of two superposed diffraction patterns from different crystal lattices [28]. Grain CI standardisation is illustrated in Figure 2.18. Grain CI standardisation changes and upgrades the CI for all the pixels in one grain to the highest CI within the grain. This does not change the orientation of phase distributions [28].

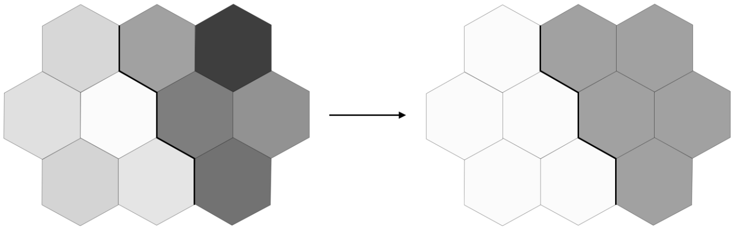

Figure 2.18: Illustration of Grain CI standardisation [28].

Neighbour CI correlation however, change the phase distribution and orientation. This cleanup method is illustrated in Figure 2.19. If a pixel in a grain is below a set value, the CI values of the neighbouring pixels are checked. The CI is upgraded to the highest CI and the orientation and phase information is changed to match this pixel [28].

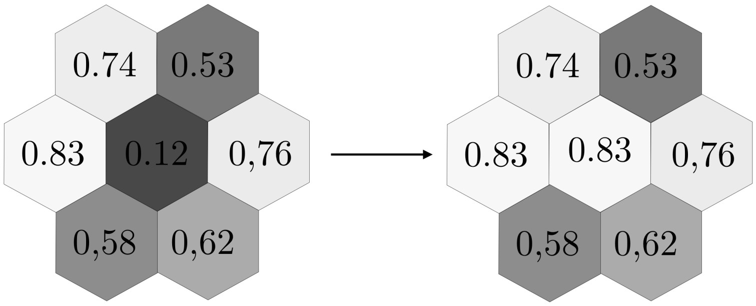

Figure 2.19: Illustration of Neighbour CI correlation [28].

Grain dilation is a cleanup method that changes the orientation to a point that do not belong to any grains. The cleanup method is illustrated in Figure 2.20. The white hexagonal pixel in the figure does not belong to any grain, but with the use of grain dilation the orientation is changed to match the largest grain [28].

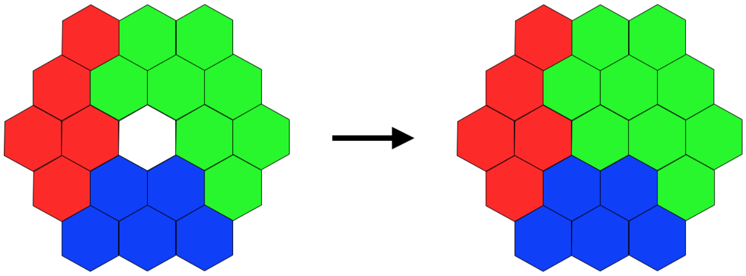

Figure 2.20: Illustration of grain dilation [28].

2.3.3 Sample preparation

To obtain good diffraction patterns the sample preparation are of importance. Since the electrons interact close to the surface (20 nm), it is important that the deformation layer is removed. From previous work done by Elstad et al. [29] it was proven that the amount of retained austenite in supermartensitic steels varied a factor 4 only on the sample preparation technique. Figure 2.21 illustrates the importance of an accurate preparation. In the figure the electron beam is focused on the specimen and the red area illustrates the deformation layer on the specimen. This figure is drawn as an illustration, which means that the size of the deformation layer and the EBSD interaction volume is not in scale.

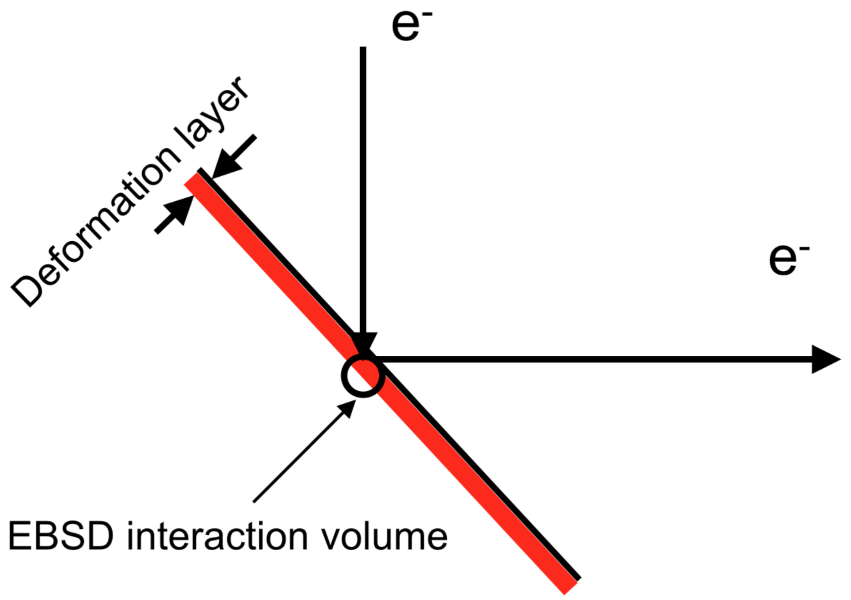

Figure 2.21: Schematic illustration of the sample preparation with EBSD interaction volume.

Electropolishing is one of the most used preparation techniques for steel. Electropolishing is an electrochemical process where the specimen is made anodic and a chemical reactive fluid, together with induced current, that removes the deformation layer at the surface at a controlled rate. Figure 2.22 schematically describes this method. Figure 2.22a shows the material after mechanical polishing with a large deformation layer. In Figures 2.22b and 2.22c the reactive fluid and induced current react with the metal surface causing removal of the deformed layer. In Figure 2.22d an ideal surface without deformation is shown [29] [30].

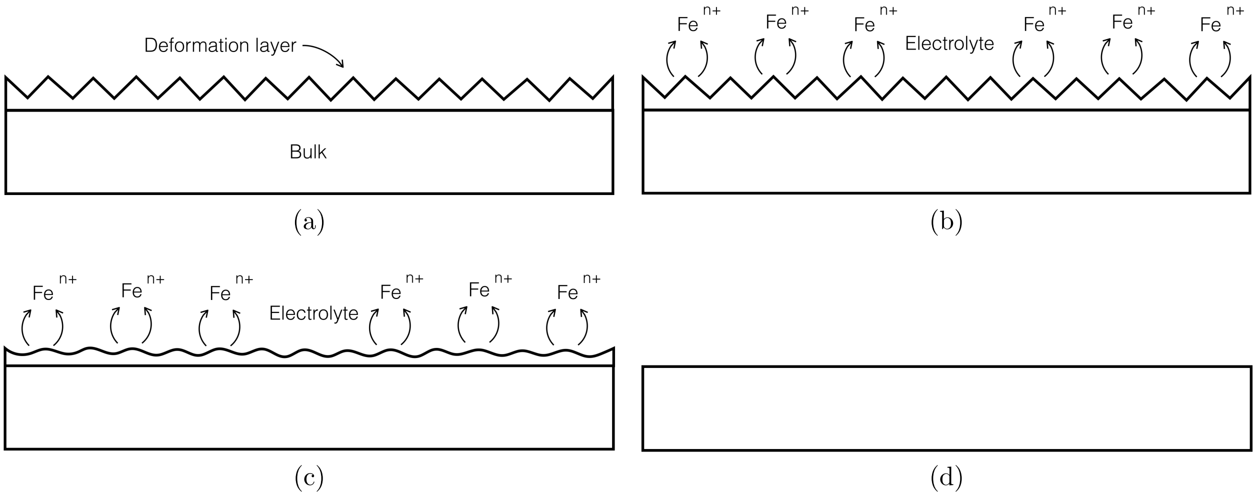

Figure 2.22: Principle of electropolishing where (a) shows the material with deformation layer, (b) and (c) show the electrolyte with current removing the deformed surface and (d) shows the a ideal surface [30].

When electropolishing the current vs. voltage curve in Figure 2.23 is exploited. Point A (before gas evolution and pitting) in the curve is considered to be the optimum area for polishing of the specimens [31].

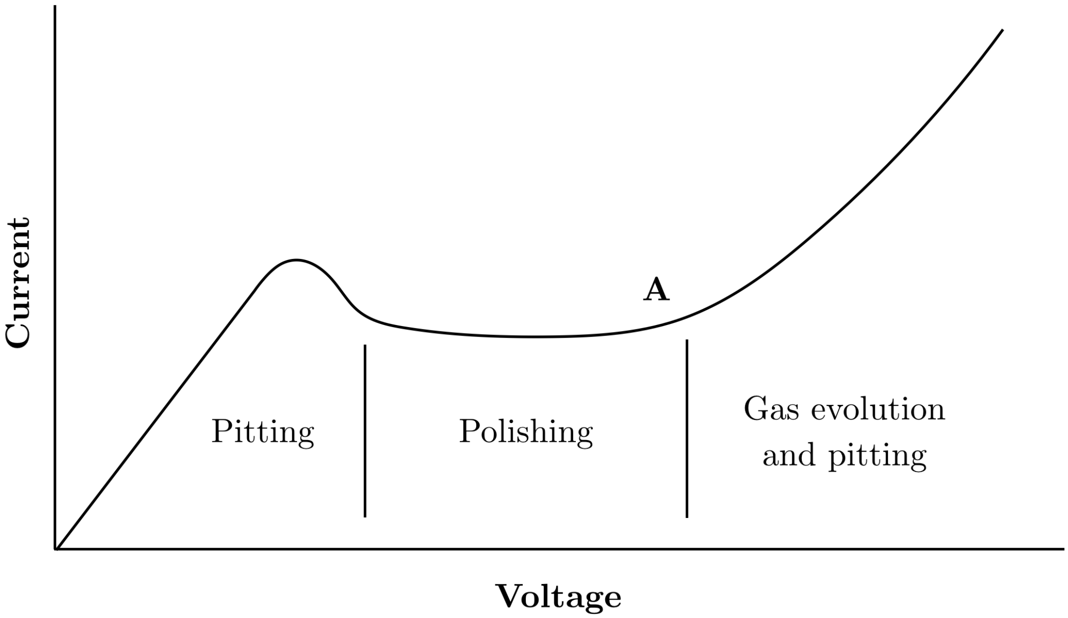

Figure 2.23: Ideal current vs. voltage curve illustrating the three distinct zones. The optimum polishing condition is considered to be at point A [31].

Chemical mechanical polishing (CMP) is commonly used as a replacement for electropolishing. During CMP a chemical is used together with mechanical polishing to remove the deformation layer on the specimen's surface. Different suspensions are used during the polishing. These suspensions contain different chemical reactivities, pH and abrasives. Figure 2.24 shows a schematic illustration of the polishing method where a force is applied on the specimen on the polishing plate. The suspension is applied and the sample holder and polishing plate rotate with an equal rotation speed [30].

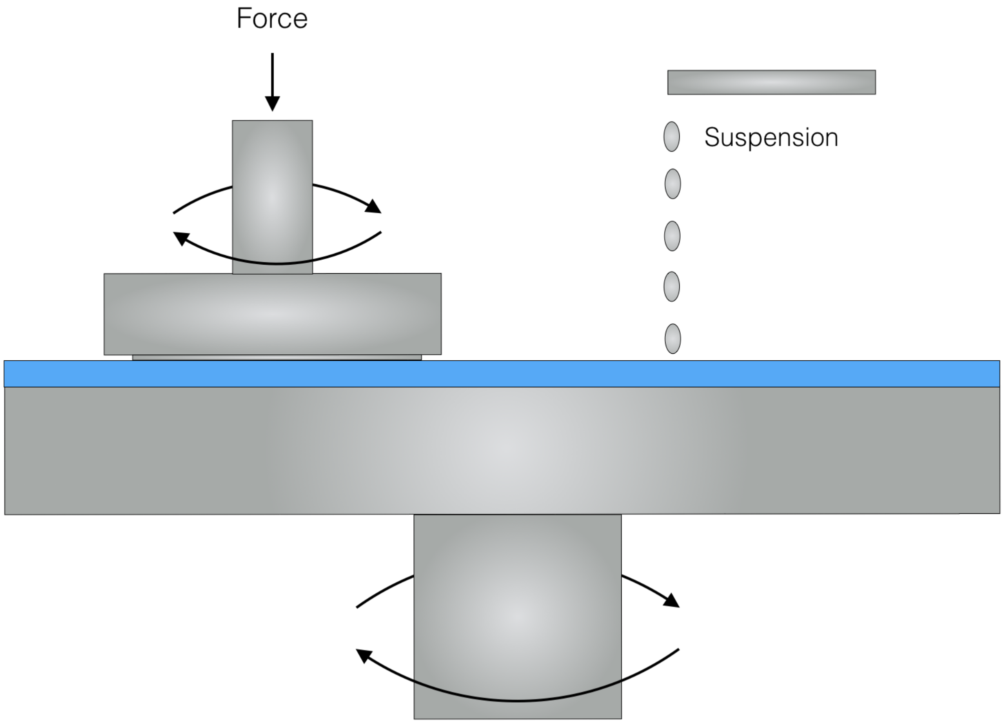

Figure 2.24: Schematic illustration of chemical mechanical polishing [30].

3 Experimental

3.1 The material

Table 3.1 shows the composition of the base material. Note that the content of nitrogen is not measured, but for this SDSS it is supposed to contain about 0.2 to 0.3 wt%. The material used in this thesis was supplied by Statoil. The material was analysed with optical emission spectrometry (OES) to determine the chemical composition. The analysis of the material showed a good compliance with UNS S32760 (Zeron 100).

Table 3.1: Overview of the chemical composition in the SDSS material.

Element	C	Si	Mn	P	S	Cr	Mo	Ni	Cu	W	Ni
Wt %	0.018	0.42	0.52	0.017	0.001	25.55	3.46	8.28	0.72	052	0.2-0.3

3.2 Sample preparation

Sample preparation is crucial during EBSD analysis since the electrons interact close to the surface, at a depth of approximately 20 nm. In the following sections several finalising preparation techniques have been tested and the most suitable technique was used during the in situ examinations. The samples for in situ testing were prepared with the following steps:

- Automatic grinding with water as lubricant and SiC paper with decreasing grit size: 800, 1200, 2000 and 4000.
- Diamond polish with lubricant (ethanol based): 3 μm and 1 μm.
- Electropolishing with A3 electrolyte, parameters are given in Table 3.2 and information about the electrolyte is given in Table 3.4.
- Ultrasonic acetone bath (5 minutes).
- Plasma cleaned for 5 minutes in a Fischione Model 1020 plasma cleaner.

To find the suitable preparation technique, A2 electrolyte and chemical mechanical polishing were also tested. For electropolishing with A2, the parameters used and the content in the electrolyte are given in Table 3.2 and 3.3.

Table 3.2: Overview of the parameters used during electropolishing.

Electrolyte	A3	A2
Area	0.5 cm^2	0.5 cm^2
Voltage	27 V	20 V
Flow rate	10	10
Time	25 sec	12 sec

Table 3.3: Chemicals and amount used in the A2 electrolyte.

Content	Amount
Perchloric acid 60 %	78 mL
Distilled water	120 mL
Ethanol	700 mL
Butylcellosolve	100 mL

Table 3.4: Chemicals and amount used in the A3 electrolyte.

Content	Amount
Perchloric acid	60 mL
Metahnol	600 mL
Butylcellosolve	360 mL

During the chemical mechanical polishing two different suspensions (OP-S and OP-U) for two different preparation times (3 minutes and 9 minutes) were tested. For both of the suspensions an abrasive that consisted of SiO_2 with grain size of 0.04 μm were used. The main difference between these two suspensions was an addition of additives in OP-S. These additives increase the chemical activity and can consist of e.g. acid (acetic acid), alkaline (potassium hydroxide), oxidation (hydrogen peroxide) and lubricating (glycerine) [32]. After this polishing sequence, the specimens were mechanically polished for 10 seconds in clean water in order to remove the suspension.

3.3 SEM

The electron microscope used during the investigations was a Zeiss Gemini Ultra 55 Field Emission SEM (FE-SEM). The parameters used for the SEM examinations are listed in Table 3.5 was used. The absorbed current was measured and the corresponding probe current was calculated in accordance with Equation 5 from section 2.3.

Table 3.5: Overview of the parameters used for the SEM examinations.

Accelerating voltage	20 kV
Working distance	23 - 27 mm
Tilt angle	70°
Aperture	300 μm
Probe current	65 - 70 nA

3.3.1 EBSD

The offline EBSD raw data collections were acquired by a NORDIF UF-1100 EBSD. To index the diffraction patterns and for analysis, EDAX/TSL OIM Data Collection 7.2.0 and EDAX/TSL OIM Analysis 7.2.0 were used, respectively. The acquisition and calibration settings used during the EBSD investigations are given in Table 3.6. The applied calibration settings had lower frame rate, higher resolution and longer exposure time than the acquisition settings. The reason for this is to ensure that the patterns applied to find the pattern centre, i.e. calibration patterns, were of good quality. By using these settings for the acquisition process the scan time will increase.

Table 3.6: Overview of the acquisition and calibration settings used during the EBSD investigations.

Parameter	Acquisition setting	Calibration setting
Frame rate	300 fps	80 fps
Resolution	120x120 px	240x240 px
Exposure time	2500 μs	11500 μs
Gain	3	4

3.4 Characterisation of the material

3.4.1 Base material and heat treatment

The base material with the chemical composition from Table 3.1 was analysed both in the deformation direction and transverse direction using the specimen geometry in Figure 3.1. Further, the material was heat treated for different times in a furnace at 850 °C. This was done in order to find a suitable heat treatment procedure used later in the in situ investigations and also to characterise the sigma phase. Multiple area scans across the surface of one of the specimens were performed to quantify how the amount of phases change at different positions within the specimens.

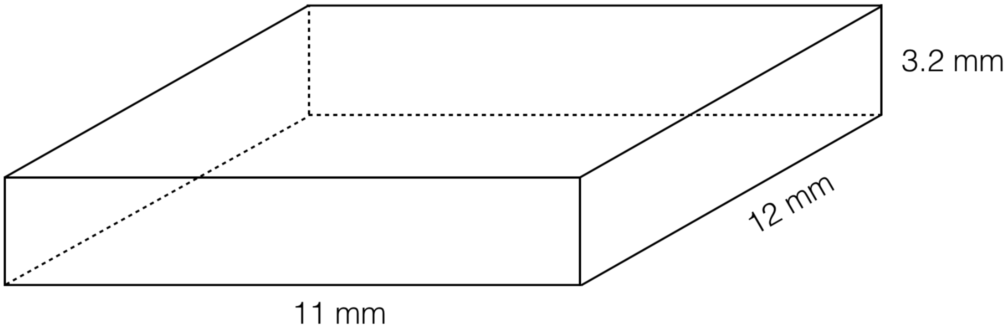

Figure 3.1: Sample geometry used during characterisation of the base material and heat treatment.

3.5 In situ tensile testing

During the in situ tensile testing in this thesis, a special stage was inserted in the SEM, see Figure 3.2. This stage enabled the tensile testing to be performed in situ. By this the amount of contamination was reduced and the same area could be investigated during tensile testing. With the use of this stage it was also possible to use a low engineering strain rate at 0.01-0.02 ${}^{\mu m}/_{s}$. Low engineering strain rate combined with fast EBSD acquisition made it possible to perform EBSD mapping continuously during tensile testing.

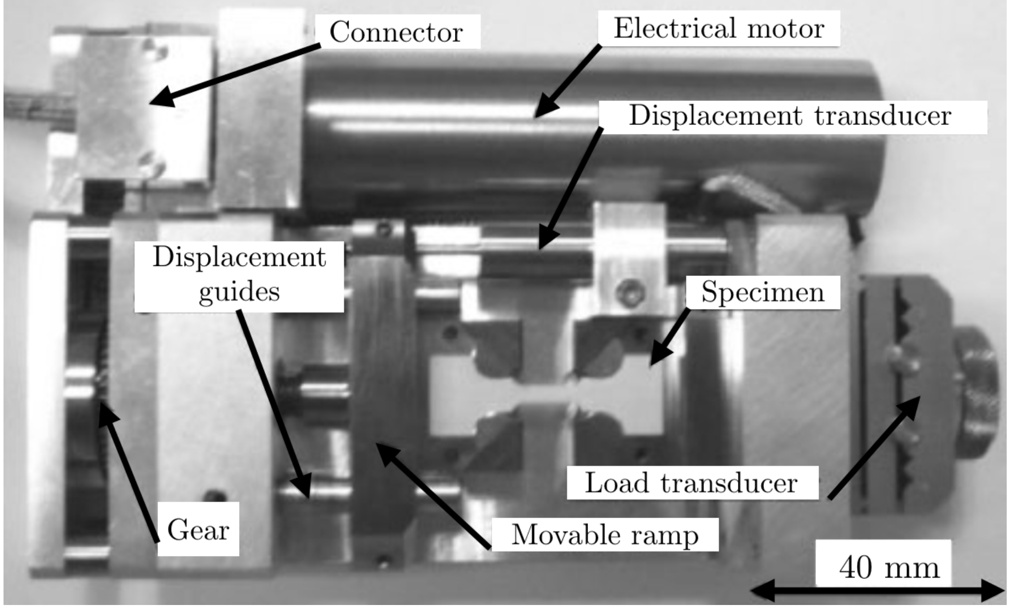

Figure 3.2: Picture of the tensile stage used during the experimental work.

Before tensile testing five samples were prepared for heat treatment in order to achieve a duplex structure containing varying amounts of sigma phase. These samples were cut in rectangular pieces (dimensions 60 mm x 15 mm x 5 mm). Further, four of the samples ere placed in a furnace and heat treated at 850 °C for 14, 17, 20 and 25 minutes, respectively, while one of the samples was not heat treated. All of the heat treated samples were quenched. The tensile samples were machined at Nomek AS Trondheim. The geometry of the tensile samples used in the tensile test is given in Figure 3.3. Before EBSD investigations the samples were prepared with the preparation technique presented in section 3.2.

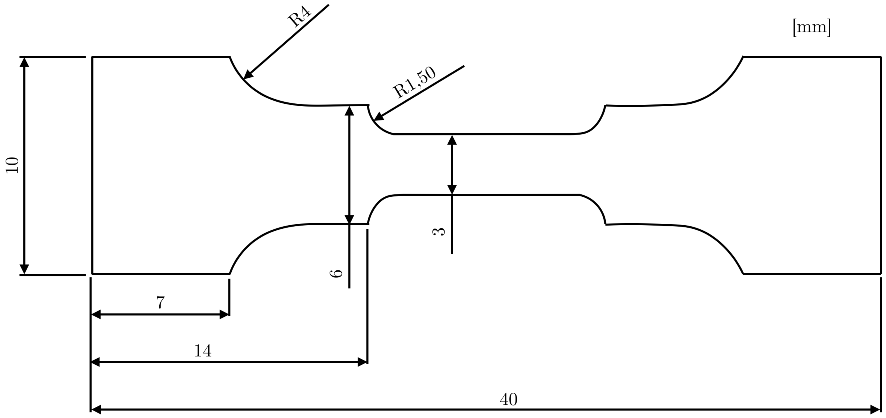

Figure 3.3: 1 mm thick tensile samples used during in situ investigations.

4 Results

In this part of the thesis the results will be presented. First, the characterisation of the material will be introduced with focus on heat treatment, sample preparation and optimisation of parameters. The main part of the results is the in situ tensile testing regarding orientation gradients, grain rotation and slip activity.

During this section some maps are used to present results. These are inverse pole figure (IPF) maps, image quality (IQ) maps, and phase maps. The phase map is also combined with the IQ map, which will cause slightly changes in the colours, but is together with a legend. The IPF maps represent the orientation of the grains referred to the IPF in Figure 4.1. As already mentioned in section 2.3.1 the colours in the IPF represent the orientation which is parallel to the tensile direction in this thesis.

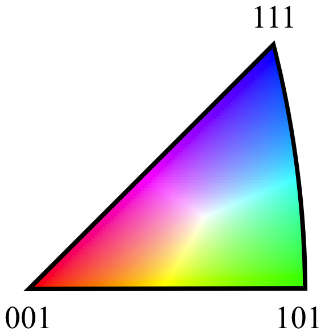

Figure 4.1: Illustration of an inverse pole figure [28].

4.1 Characterisation of the material

4.1.1 Base material and heat treatment

The phase distribution for both transverse direction and deformation direction is given in Figure 4.2, where green is austenite and red is ferrite. From the figure it can seen a more elongated phase distribution in the deformation direction than in the transverse direction. The patterns used to make the figure is not correctly modelled in 3D, but serves as an illustration.

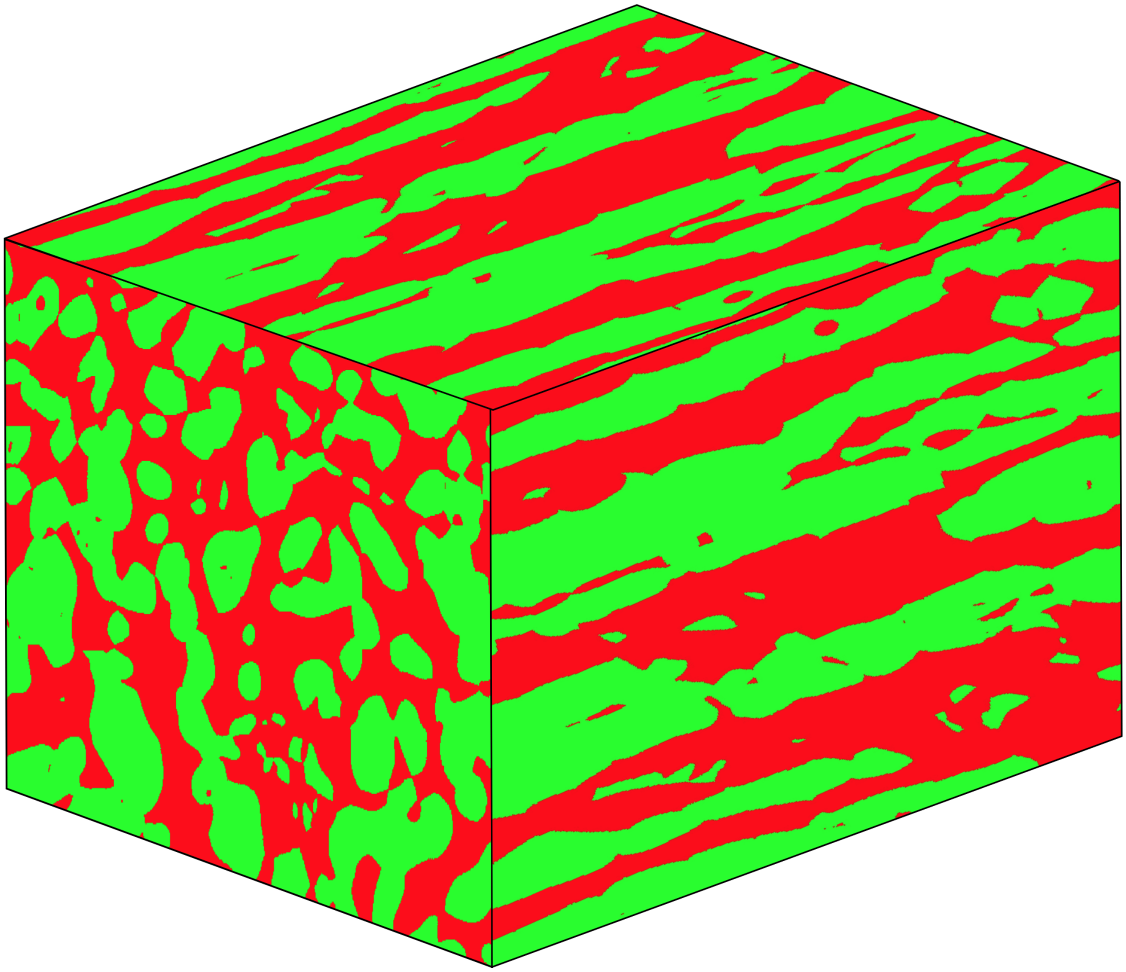

Figure 4.2: Illustration of the different microstructures in different directions in the base material. The phase distribution is elongated in the deformation direction.

Figure 4.3 shows the analysis of the base material where 4.3a, 4.3c and 4.3b, 4.3d is transverse and deformation direction, respectively. The amounts of ferrite and austenite found in each of the directions are given in Table 4.1. The IPF maps show more elongated grains in the deformation direction than in the transverse direction.

Table 4.1: Amount of ferrite and austenite in both directions.

Phase	Ferrite	Austenite
Transverse direction	47 vol.%	53 vol.%
Deformation direction	48 vol.%	52 vol.%

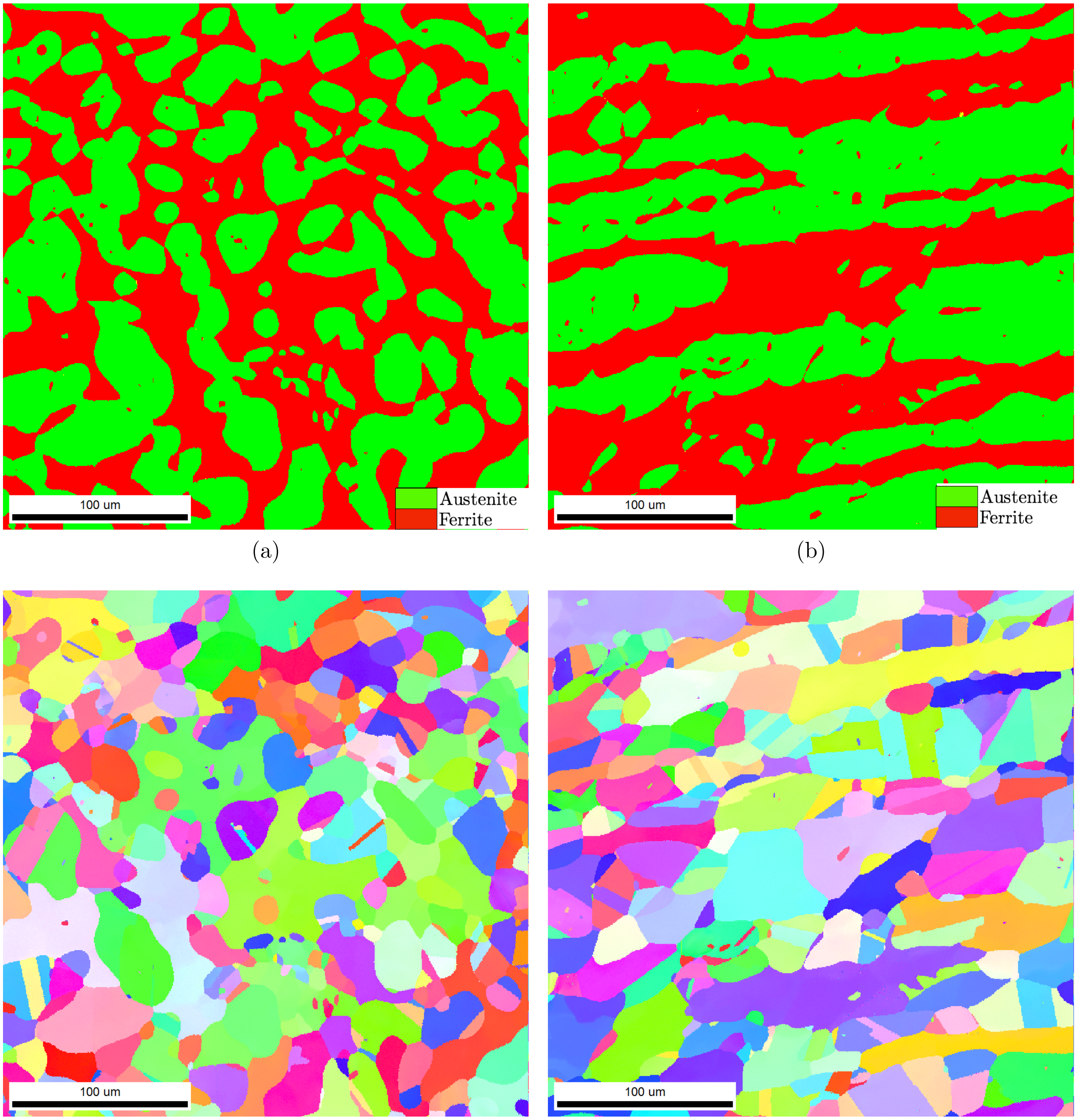

(a) (b)

(c) (d)

Figure 4.3: Phase and IPF maps of the base material where (a) and (b) show the phase distribution where green is austenite and red is ferrite. (c) and (d) show the IPF maps in the transverse and deformation direction, respectively.

Heat treatment was performed at 850 °C for 6, 12, 15, 22, 30, 45 and 60 minutes. It should be noted that the furnace used in the experiments did not hold a stable temperature. It also took 2 minutes for the sample to reach 850 °C. Table A.1 in Appendix A.1 shows the phase distribution for all the samples with the corresponding confidence index for all the phases and the sigma phase separately. The phase distribution as a function of annealing time at 850 °C is given in Figure 4.4. With increasing annealing time the amount of ferrite decreases, while the amount of sigma and austenite increases.

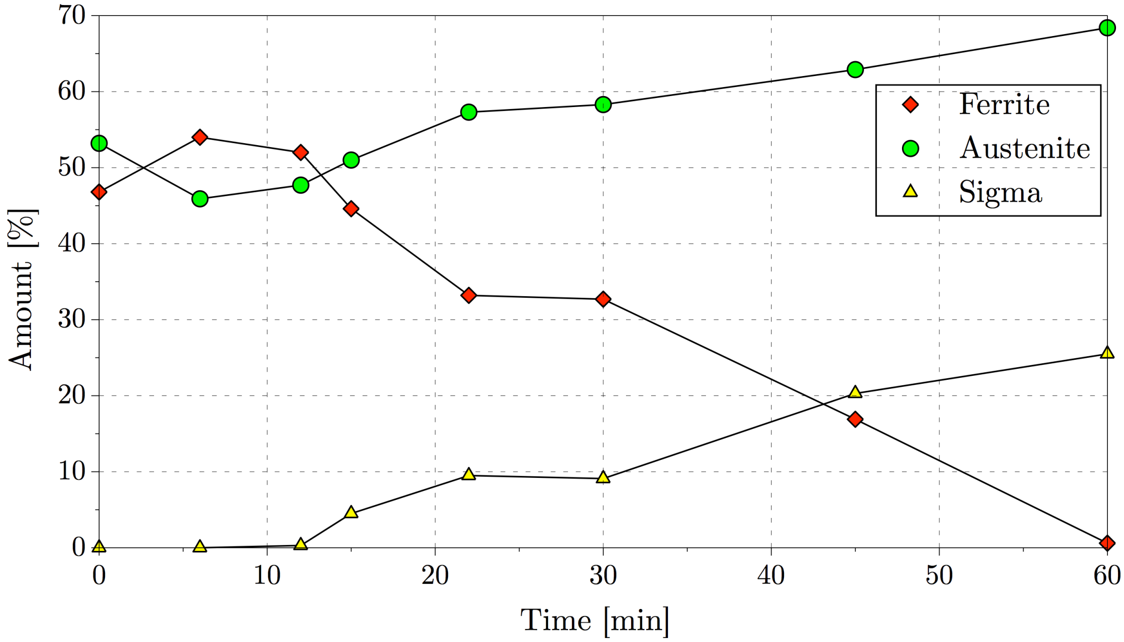

Figure 4.4: Phase distribution as a function of annealing time at 850 °C.

Figure 4.5 shows a few selected maps from the heat treatment where the samples in Figures 4.5a, 4.5c and 4.5b, 4.5d were annealed for 12 and 22 minutes, respectively. From Figure 4.5a it can be seen that the transformation from ferrite to sigma starts. In the points 1-4 marked with circles the nucleation preferably starts at the austenite-ferrite interface and grows into the ferrite. In Figure 4.5b more sigma and austenite are formed while the ferrite content is strongly reduced. From the IQ maps in Figures 4.5c and 4.5d the sigma phase appears to have low quality in contrast to ferrite and austenite. This is supported with a relatively low pattern quality (see Figure 4.9b).

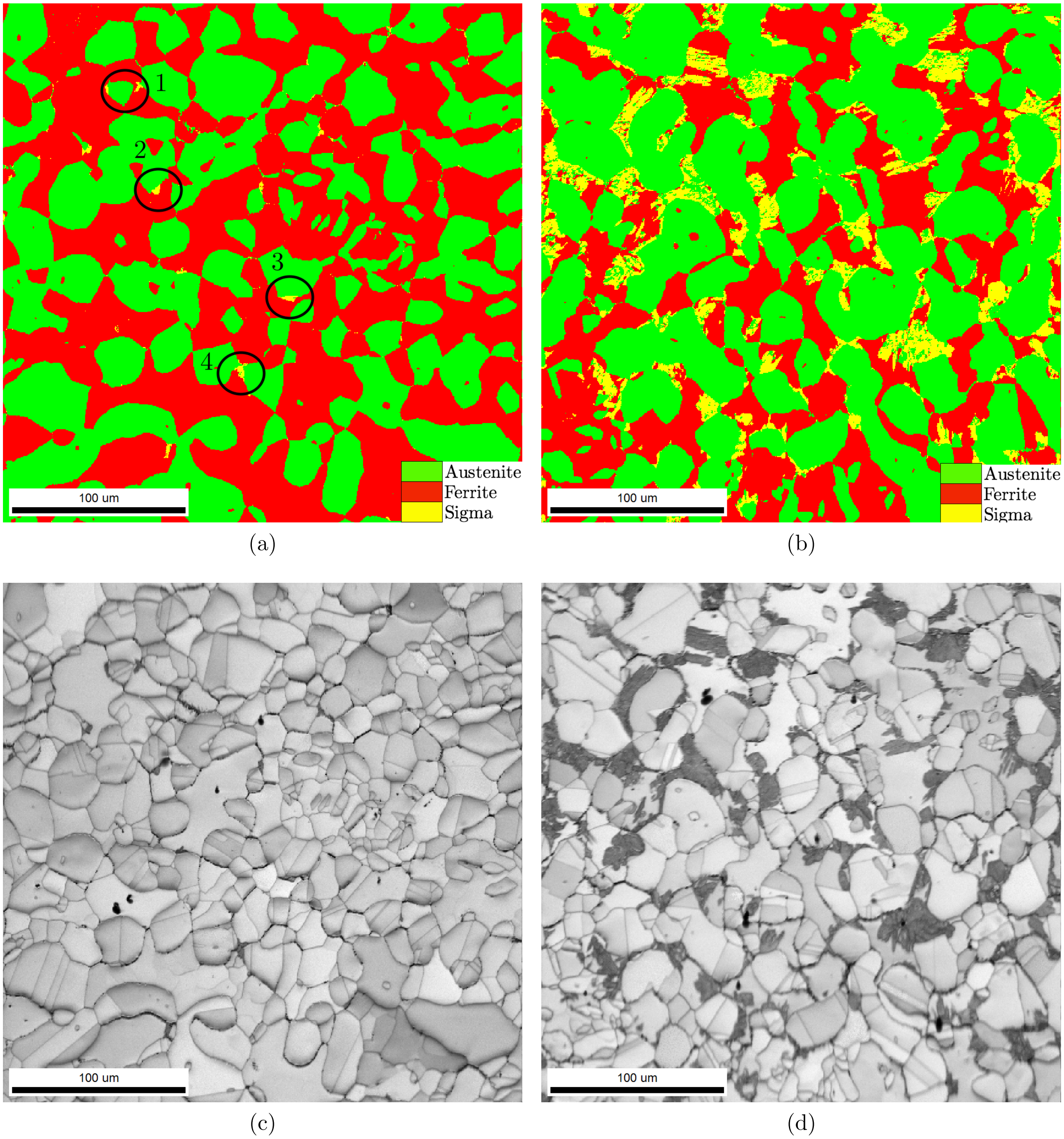

(a) (b)

(c) (d)

Figure 4.5: Phase and IQ maps of the material annealed at 850 °C for 12 and 22 minutes. In (a), the transformation to sigma starts and in (b) more sigma and austenite are formed, while the ferrite content is decreased. (c) and (d) show IQ maps where increasing annealing times result in more sigma and reduced image quality.

Figure 4.6 shows the amount of phases in each area scanned across the surface of the sample annealed at 850 °C for 30 minutes. An overview of the scanned areas is given in Figure 4.7 where each of the squares correspond to a region of interest. Each of these areas are 300 μm^2. This was done to find the variance in the measured data. As shown in the figure there are small variances in the measurements shown by standard deviations calculated for the whole set of data. These were found to be 1.3, 2.1 and 2.8 for sigma, ferrite and austenite, respectively.

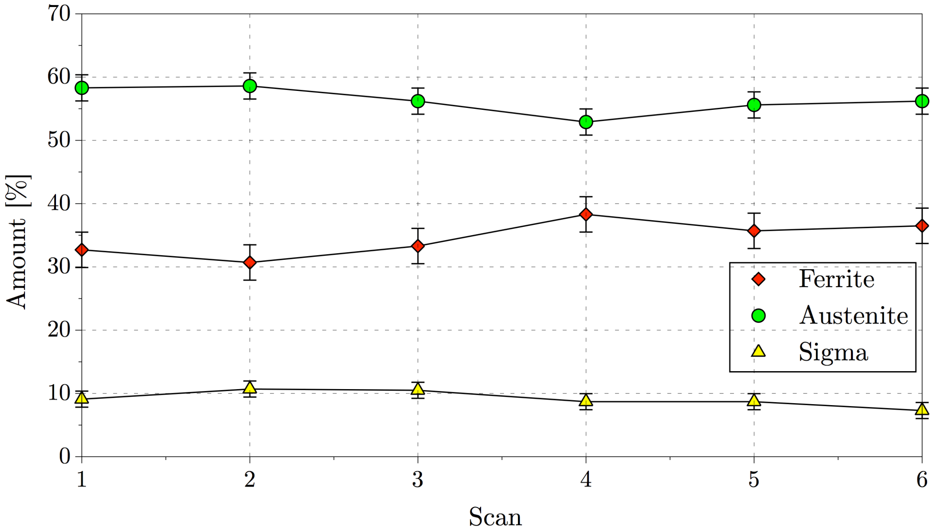

Figure 4.6: Plot of the area scan showing the amount of ferrite, austenite and sigma on the y-axis and the area number on the x-axis.

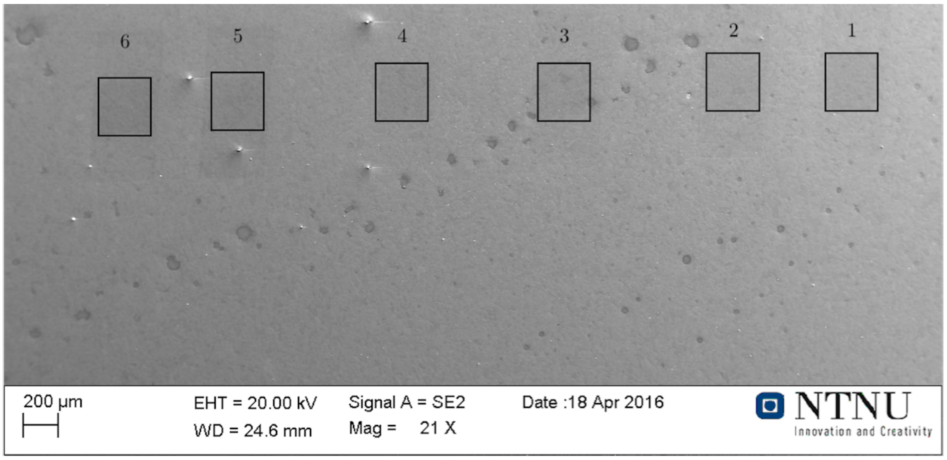

Figure 4.7: Illustration of the area scan where each of the squares in the figure correspond to a region of interest (ROI).

4.1.2 Sample preparation

Figure 4.8 shows IPF maps illustrating the varying amounts of sigma phase arising from different preparation techniques and preparation parameters. The orientation differences within this phase give an indication on the reliability of the indexing. As a function of finalising preparation techniques small differences in the orientation spread can be seen in these IPF maps. It seems like there is less orientation spread, i.e. less misindexing when the sample is electropolished (Figures 4.8a and 4.8b). However, these IPF maps are not from the same sample and there are different amounts of sigma phase within each sample.

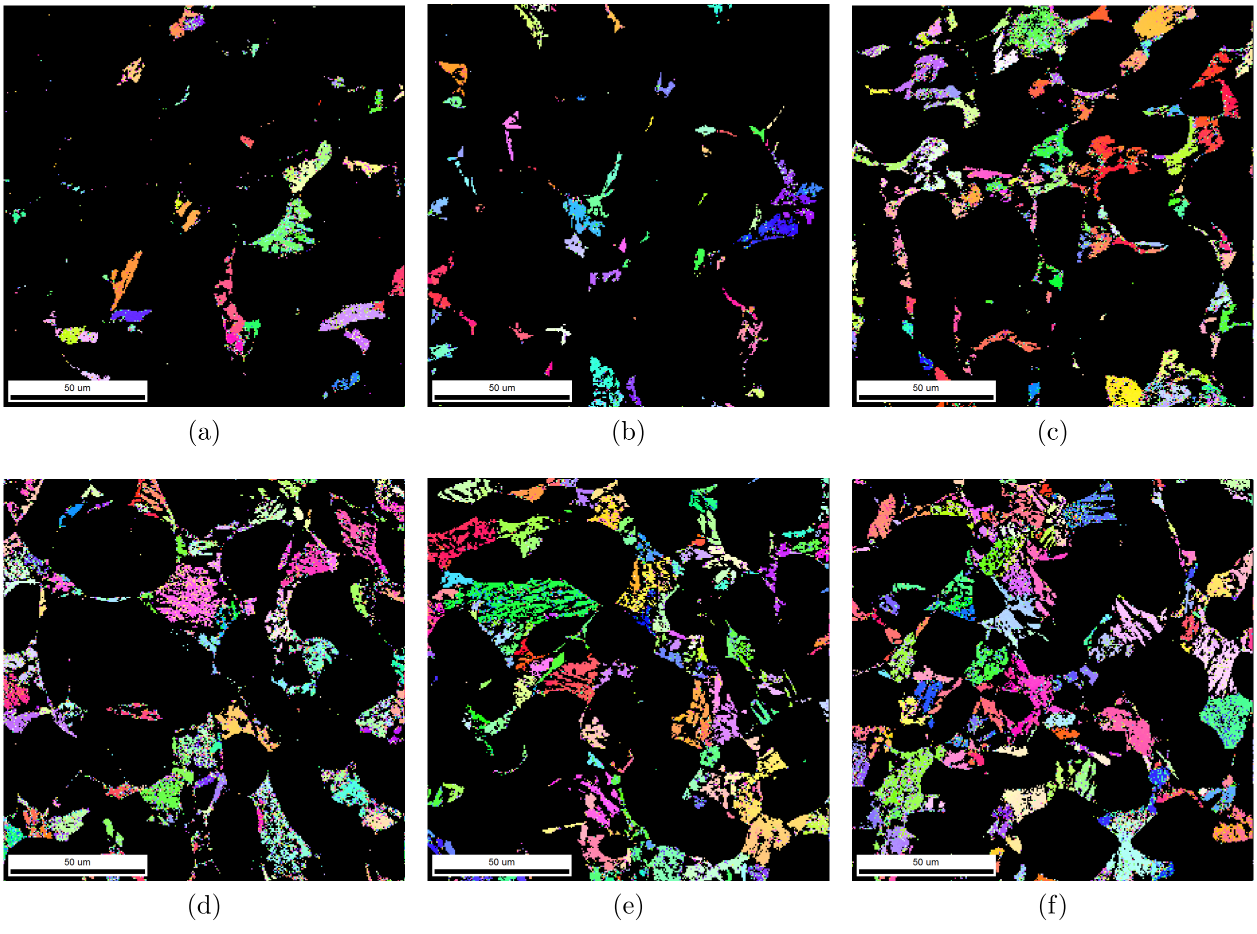

(a) (b) (c)

(d) (e) (f)

Figure 4.8: IPF maps of the sigma phase where the applied preparation techniques are (a) A2, (b) A3, (c) OP-S 3 minutes, (d) OP-S 9 minutes, (e) OP-U 3 minutes, (f) OP-U 9 minutes. Austenite and ferrite is excluded from the maps.

The difference in pattern quality of the two different phases is given in Figure 4.9. The acquisition pattern for (a) austenite and (b) sigma phase show good and poor pattern quality, respectively.

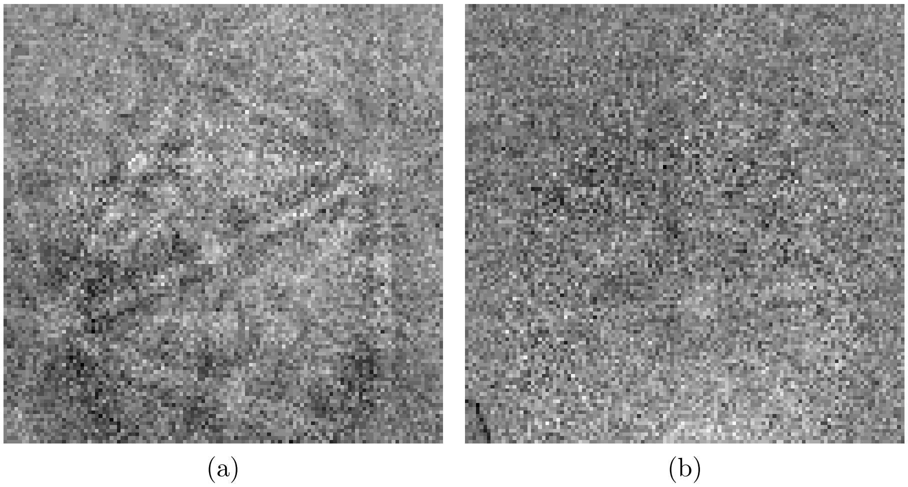
(a) (b)

Figure 4.9: Difference in pattern quality of (a) austenite pattern and (b) sigma phase pattern.

The CI as a function of preparation method is given in Figure 4.10. In the plot both average CI for the whole scan and CI for only the sigma phase are given. The electropolishing methods got the highest average CI. From the sigma phase alone only A3 electrolyte deviate.

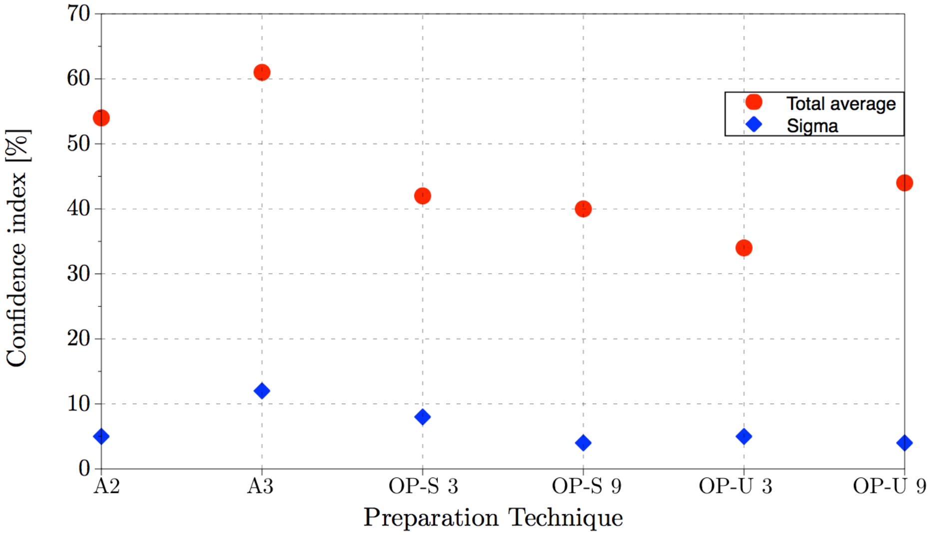

Figure 4.10: Confidence index for the whole scan the sigma phase separately.

Image quality maps are given in Appendix A.2. These IQ maps show a better quality for the electropolished samples (applying to Figures A.1a and A.1b).

4.1.3 Optimisation of parameters

Since the pattern quality of the sigma phase remained poor after using different finalising preparation techniques the parameters were optimised. The sigma phase identification and characterisation were carried out by using an extracted ROI. The ROI was applied using the new developed NORDIF EBSD Extraction Software [33], together with optimisation of EBSD Hough parameters. A manual regarding the different functions in the NORDIF Extraction Software is given in Appendix C.3. Since the sigma phase was shown with a low quality it was crucial to optimise the parameters used during indexing. The Hough settings before and after optimisation are given in Table 4.2.

Table 4.2: Hough settings before and after optimisation [34].

Parameter	Before	After
Binned pattern size	120	120
Theta step size	1	1
Rho fraction	85 %	89 %
Min/max peak count	3/7	3/14
Min peak magnitude	5	1
Min peak distance	15	10
Peak symmetry	0.50	0.70

The Hough parameters were adjusted and resulted in more reliable indexing. Figure 4.11a shows an image quality map with the corresponding ROI. The dark areas (low pattern quality) in the ROI contain sigma phase. Figures 4.11b and 4.11c show IPF maps before and after the Hough optimisation based on the patterns in the ROI.

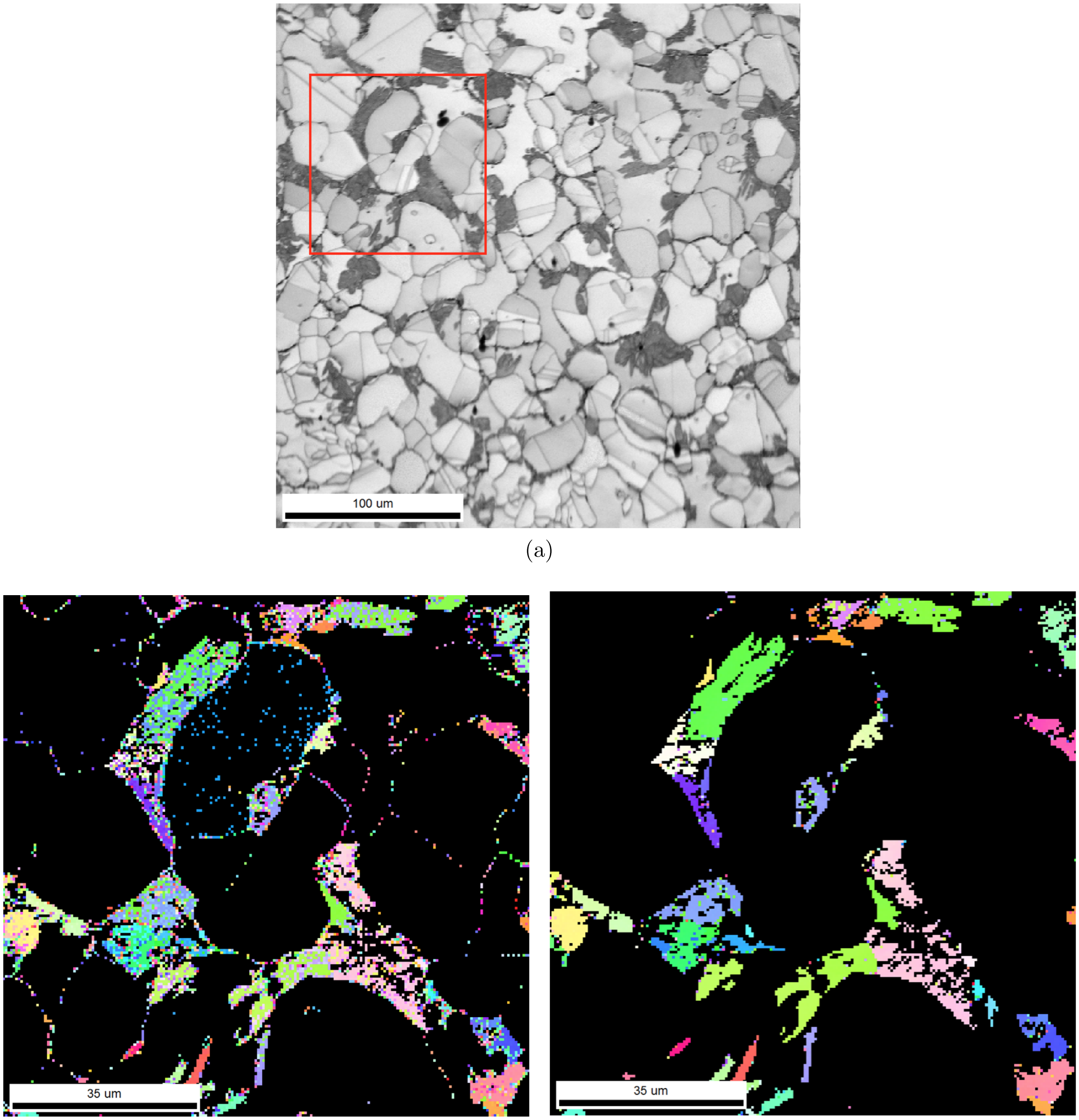

(a)

(b) (c)

Figure 4.11: IQ maps where dark areas consist of sigma phase in (a). In (b) and (c) an IPF map showing the sigma phase before and after Hough optimisation is presented [34].

4.2 In situ tensile testing

During this thesis continuous EBSD mapping was performed during in situ tensile testing of SDSS. In the following sections there will be presented data that will be discussed later on. Five different specimens were tested with the distribution of ferrite, austenite and sigma phase given in Table 4.3.

Table 4.3: Phase distribution at 850 °C as a function of annealing time.

Phase	Annealing time [min]				
	0	14	17	20	25
Ferrite	50.4	46.2	41.3	35.9	27.3
Austenite	46.9	51.0	53.1	55.5	60.1
Sigma	0	2.8	5.6	8.5	12.5

During heating of the specimens, the samples used some minutes to reach 850 °C (see Figure 4.12). From the figure it is evident that the specimens used about 400 seconds to reach the temperature. However, the sigma phase formation will begin prior to this desired temperature.

The stress strain curves for the in situ investigations are given in Figure B.8, Appendix B.8. From these curves it can be seen that the mechanical properties vary with the different heat treatments. Both the tensile strength and yield strength increase with increasing annealing time, an exception is the sample annealed for 17 minutes which obtain an high tensile strength even with low annealing time, i.e. low amounts of sigma phase. The offset yield stress and the calculated Young's modulus are given in Table 4.4.

Table 4.4: Proof stress and Young's modulus.

Mechanical properties	Annealing time [min]				
	0	14	17	20	25
Offset yield stress [MPa]	50	70	61	61	63
Young's modulus [GPa]	27	37	30	35	36

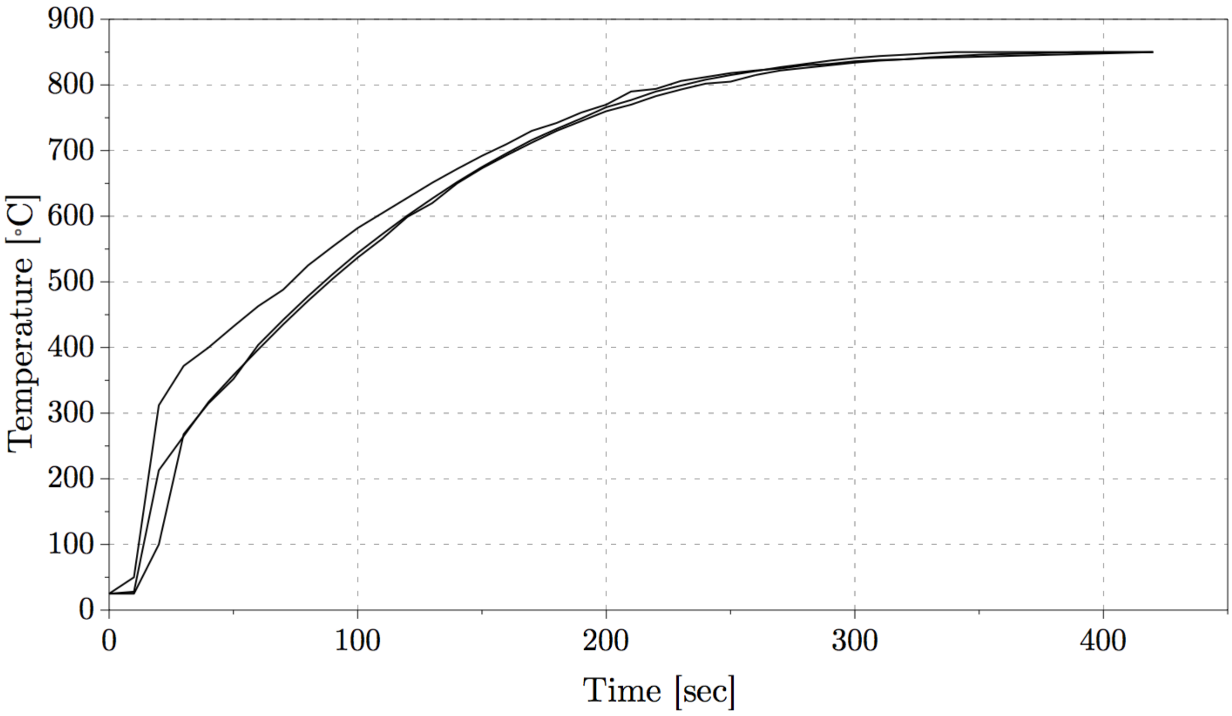

Figure 4.12: Heat curve up to 850 °C.

4.2.1 Orientation gradients

Throughout the rest of this section there are given several IPF maps which display the deformation during the tensile testing. Figures 4.13 and 4.14 display IPF maps where the crystallographic orientations are aligned parallel with the tensile direction. These crystallographic orientations are referred to the IPF in Figure 4.1. In the IPF the colours represent the orientations parallel to the tensile direction.

From Figure 4.13 five IPF maps of the base material are given with increasing strain from Figure 4.13a to 4.13e. All of these IPF maps are cleaned with grain dilation (as described in section 2.3.2) and the raw maps can be found in Figure B.1, Appendix B.1. During the deformation some orientation gradients are formed within the grains. The circles in Figure 4.13e show areas which prominent orientation gradients close to the [001] pole in the IPF. The same correlation can be seen in Figure 4.14 where the IPF maps from the sample annealed for 25 minutes with approximate 13 vol.% sigma is given with increasing strain. The IPF maps of the other samples are given in Figures B.2, B.3 and B.4, Appendices B.2 - B.4.

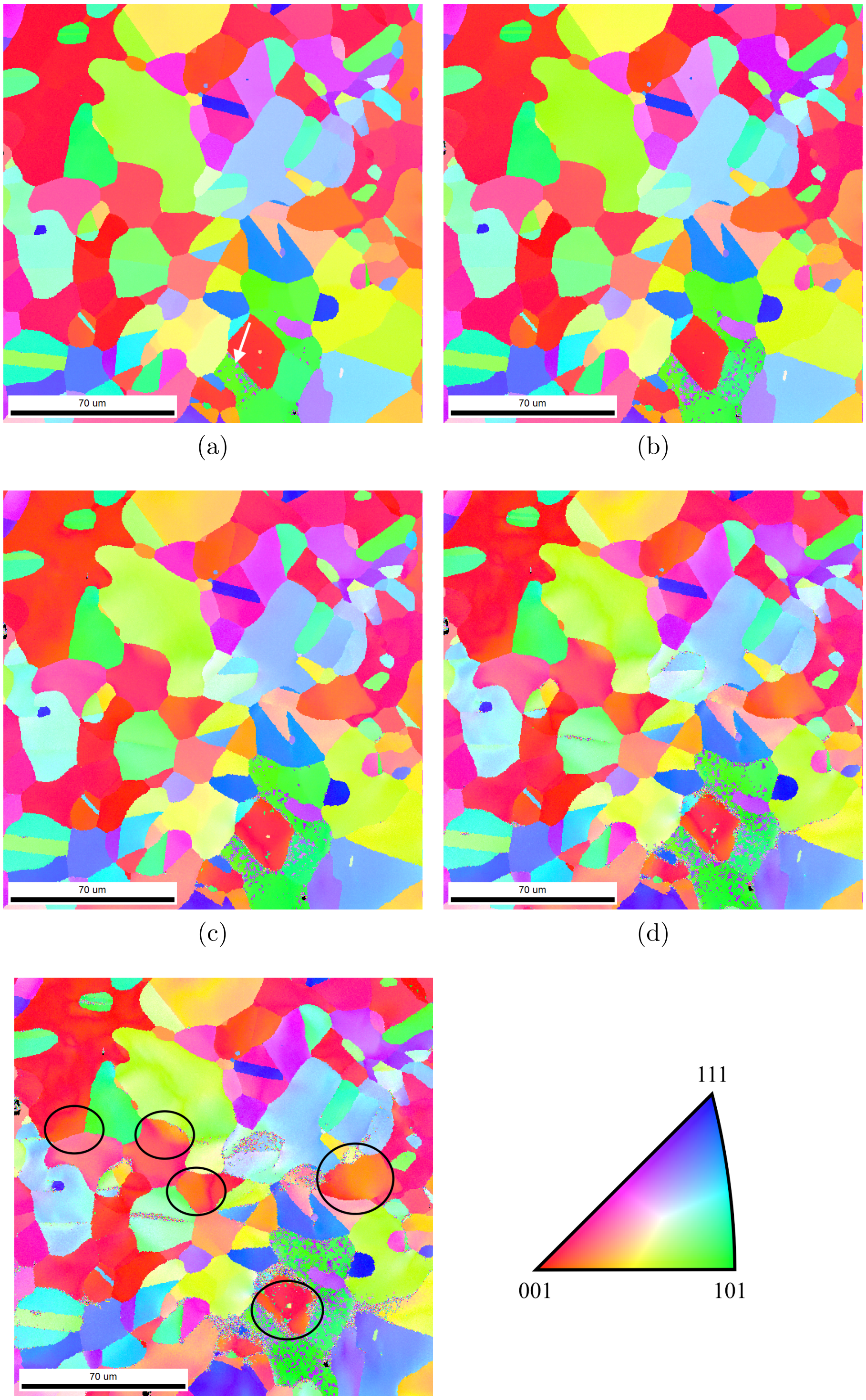

(a) (b)

(c) (d)

(e) (f)

Figure 4.13: IPF maps of the base material with increasing strain where (a) 0 %, (b) 2 %, (c) 4 %, (d) 6 %, (e) 8 % and the legend is given in (f). The white arrow in (a) shows misorientation within a grain which will be discussed in section 5.2. In (e) the circles show areas which contain prominent orientation gradients.

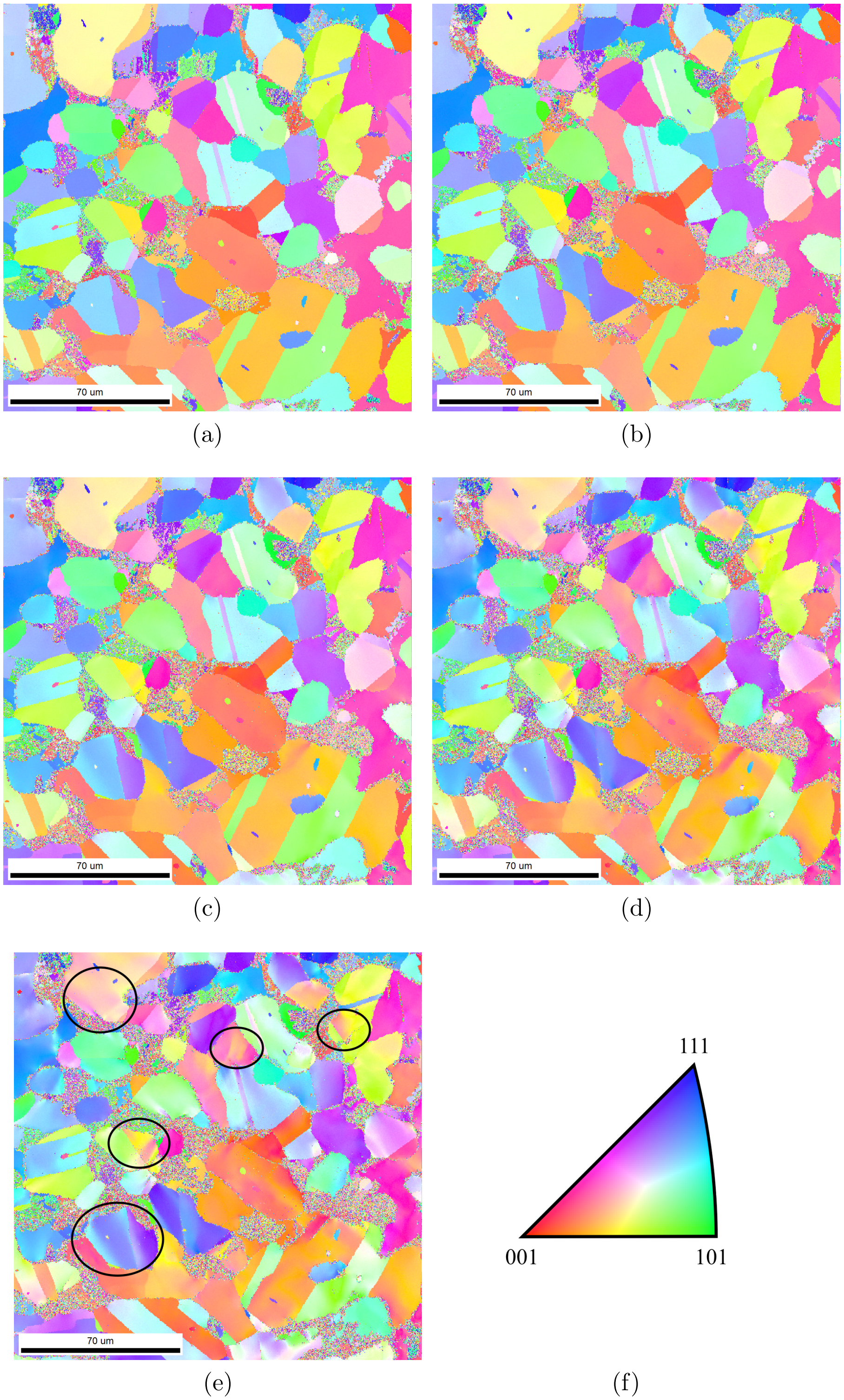

(a) (b)

(c) (d)

(e) (f)

Figure 4.14: IPF maps of the material annealed for 25 minutes containing approximately 13 vol.% sigma with increasing strain where (a) 0 %, (b) 2 %, (c) 4 %, (d) 6 %, (e) 8 % and the legend is given in (f). Circles in (e) show areas which contain prominent orientation gradients.

From Figures 4.17 and 4.18 orientation gradients within single grains can be seen. The corresponding area in the base material where the misorientations are extracted from is given in Figure 4.15. Ferrite and austenite grains are marked with ”F + grain number” and ”A + grain number”, respectively. The other IPF maps in which the misorientations are extracted from is given in Figure B.9, Appendix B.9.

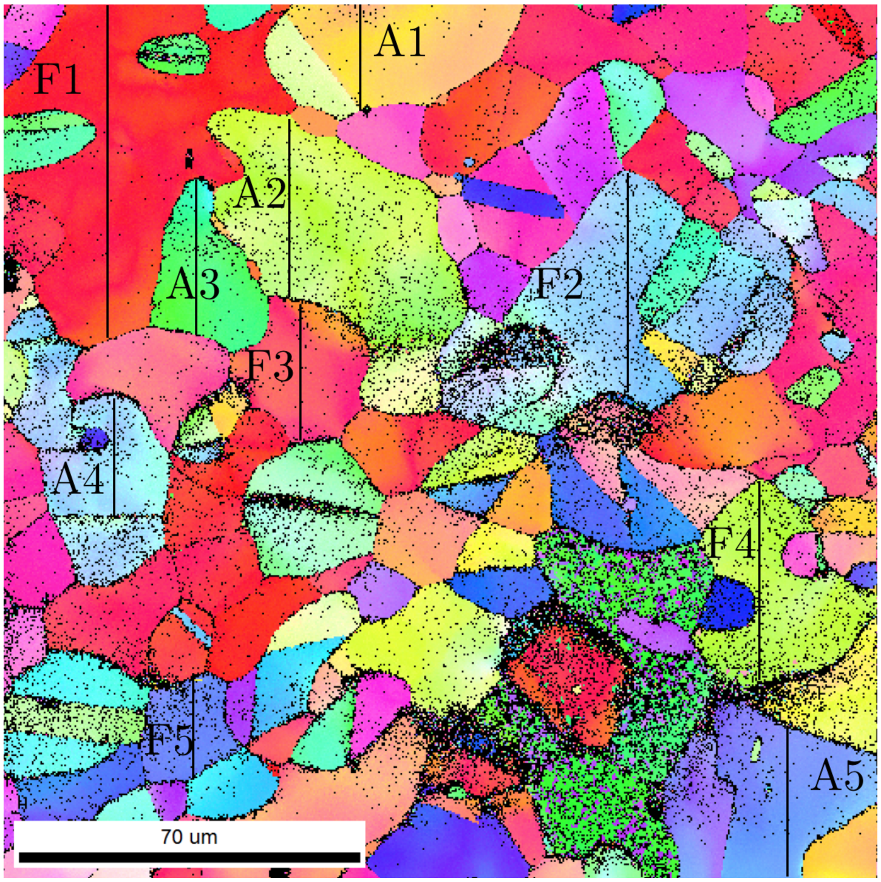

Figure 4.15: IPF from the base material after 8 % strain. The grains which where used in the misorientation study is marked from F1 to F5 and A1 to A5 for the ferrite and austenite, respectively.

Figure 4.16 shows some of the orientation gradients in selected grains before deformation. From this it can be seen that the orientation gradients before deformation are minimal. Only one austenite grain (Grain A3, Figure 4.16a) have some degree of misorientation within the grain. The rest of the orientations before deformation are given in Figure B.10, Appendix B.10.

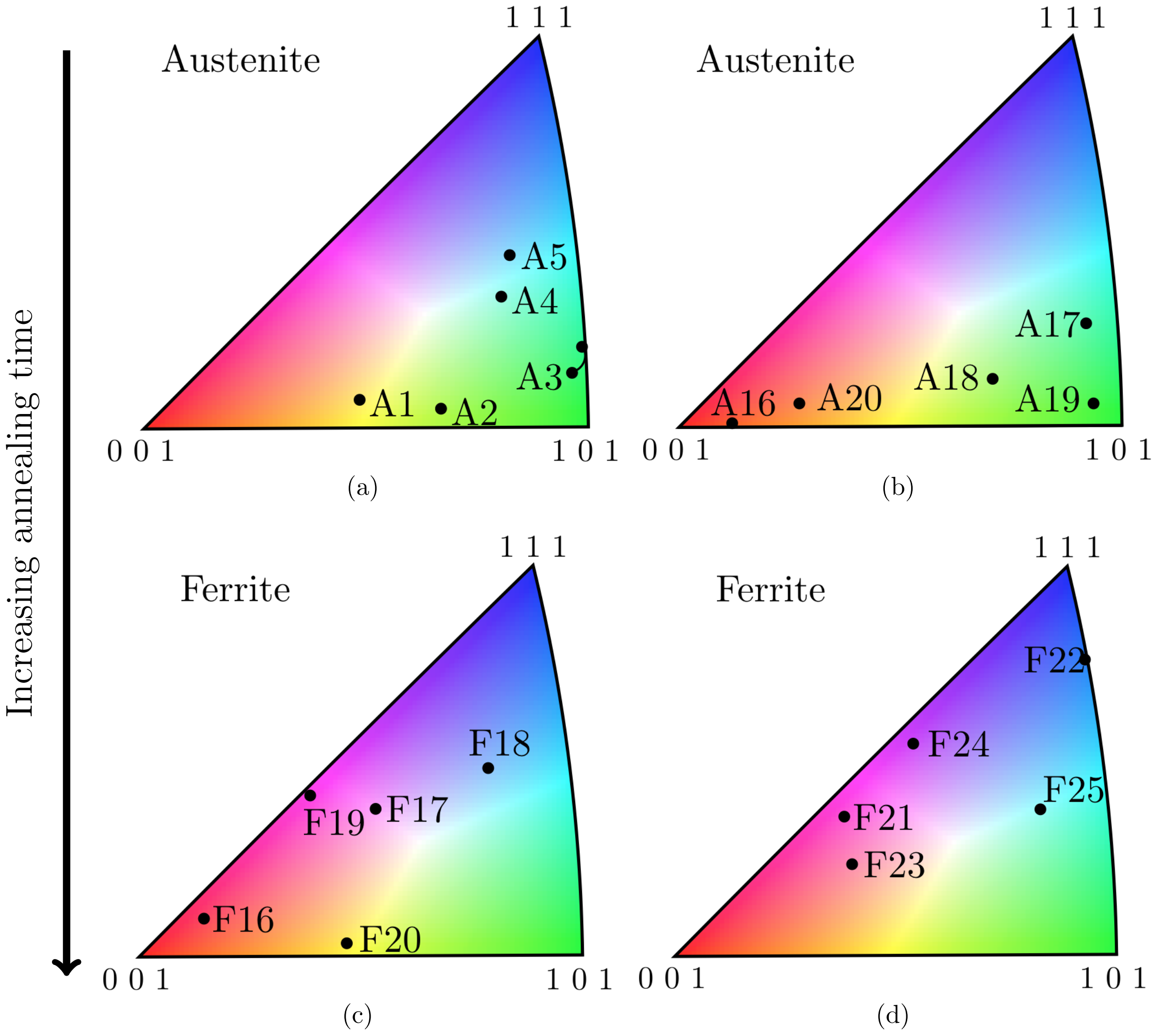

(a) (b) (c) (d)

Figure 4.16: Orientations inside selected grains before deformation. Ferrite and austenite grains are marked with F and A, respectively. The samples were annealed for (a) 0 minutes, (b,c) 20 minutes and (d) 25 minutes.

In the ferrite phase a couple of grains deviated from the others after tensile testing at 8 vol.% strain. This sample was annealed for 17 minutes at 850 °C and contains about 6 vol.% sigma. After 20 and 25 minutes with a content of 9 and 13 vol.% sigma, respectively, some degree of orientation gradients evolved. Especially in grain F16 and F18 in Figure 4.18a and also F23 in Figure 4.18c. From the figures it seems like there is a larger average misorientation in austenite than in ferrite where especially grain A3 from Figure 4.17b and A18 in Figure 4.18b show a deviation.

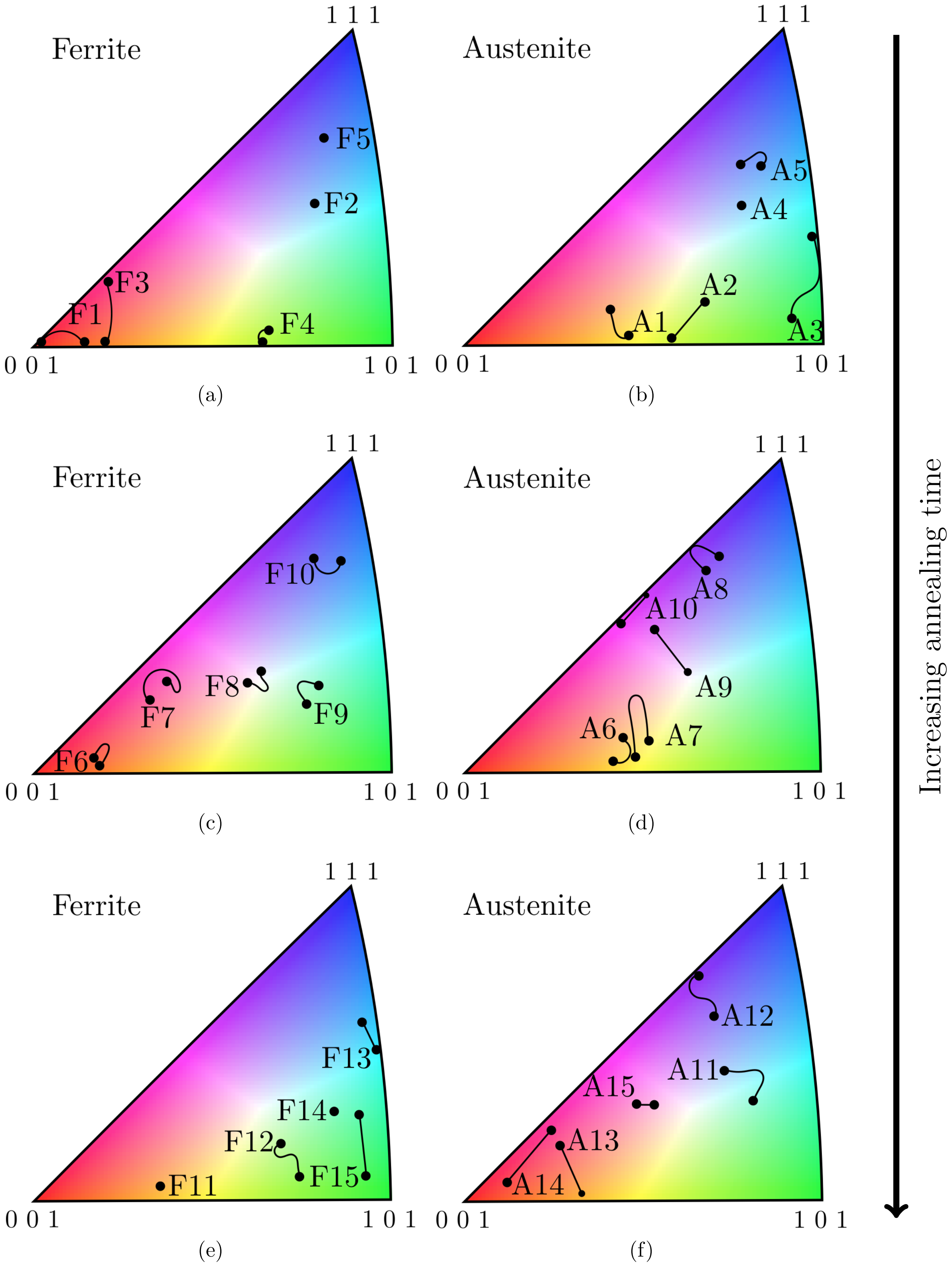

Figure 4.17: Orientation gradients inside selected grains. Ferrite and austenite grains are marked with F and A, respectively. The samples were annealed for (a,b) 0 minutes, (c,d) 14 minutes and (e,f) 17 minutes.

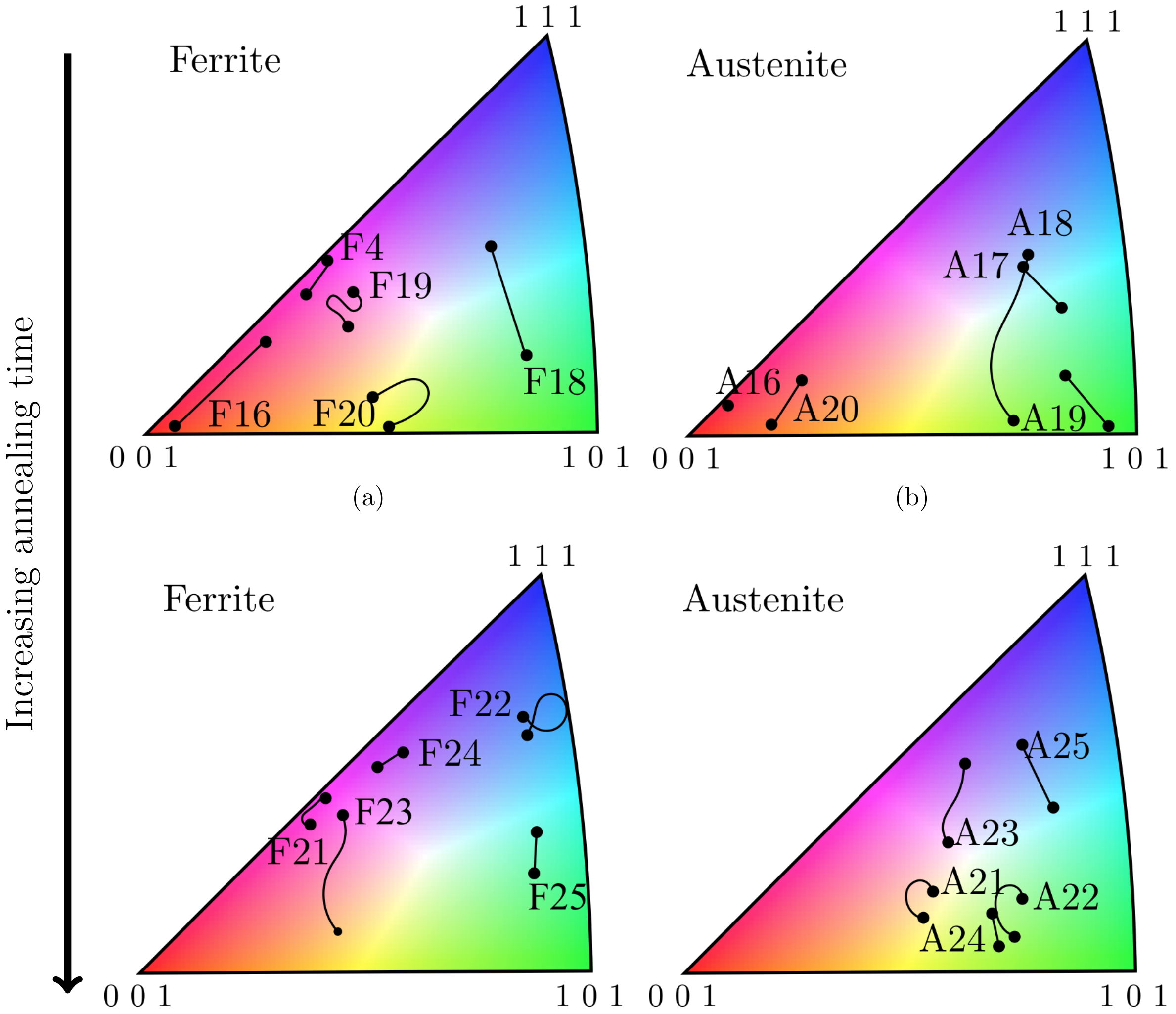

(a) (b) (c) (d)

Figure 4.18: Orientation gradients inside selected grains. Ferrite and austenite grains are marked with F and A, respectively. The samples were annealed for (a,b) 20 minutes and (c,d) 25 minutes.

From selected grains there is also included a misorientation plot. These plots were chosen from grains in which have both low and high misorientations as shown in Figures 4.17 and 4.18. As seen in the figures, large orientation gradients provide a large misorientation value across the surface (see Figure 4.19a). This value reaches 18° which corresponds to a high angle grain boundary (>15°). From the grains that consisted of small orientation gradients (see Figure 4.19b) the misorientation values did not exceed 6° between starting and finishing points.

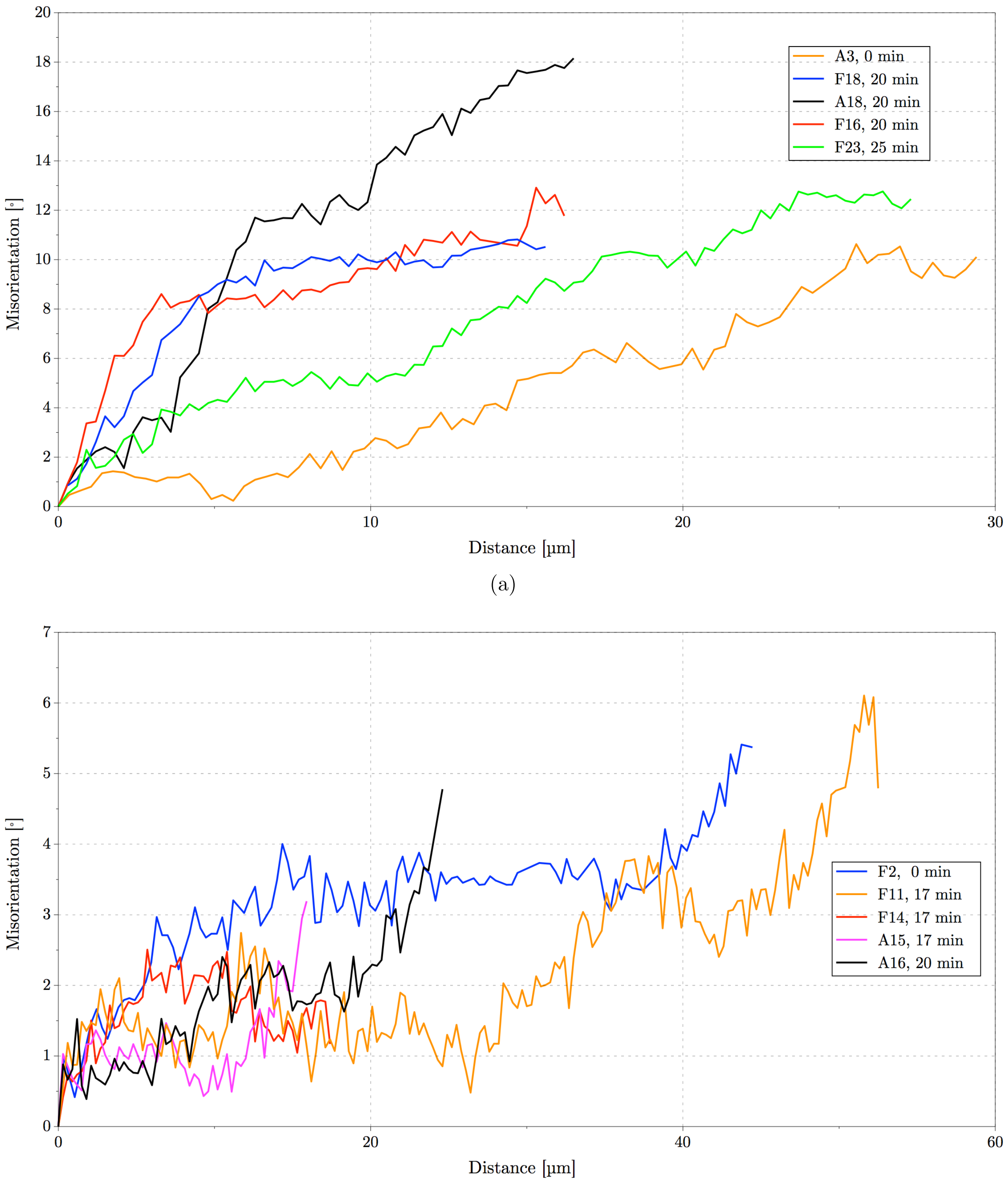

(a)

(b)

Figure 4.19: Plot of misorientation where (a) is grains with large orientation gradients and (b) is grains with small orientation gradients.

4.2.2 Grain rotation

A grain rotation study was performed and the following results are displayed in Figures 4.20 and 4.21. The grain rotation is obtained by applying a point mainly in the centre of the grain. A total number of about 210 grains from the various heat treatments for ferrite and austenite were investigated. The rotation before and after tensile testing at 8 % strain is plotted in an IPF where the ferrite phase is given in Figures 4.20a, 4.20c, 4.21a, 4.21c and 4.21e and the austenite phase is given in Figures 4.20b, 4.20d, 4.21b, 4.21d and 4.21f. From the figures it can be seen that the austenite phase rotates from the [101] direction towards the [111] direction or the area that connects the [111] direction and the [001] direction. Ferrite tends to rotate against the [101] direction.

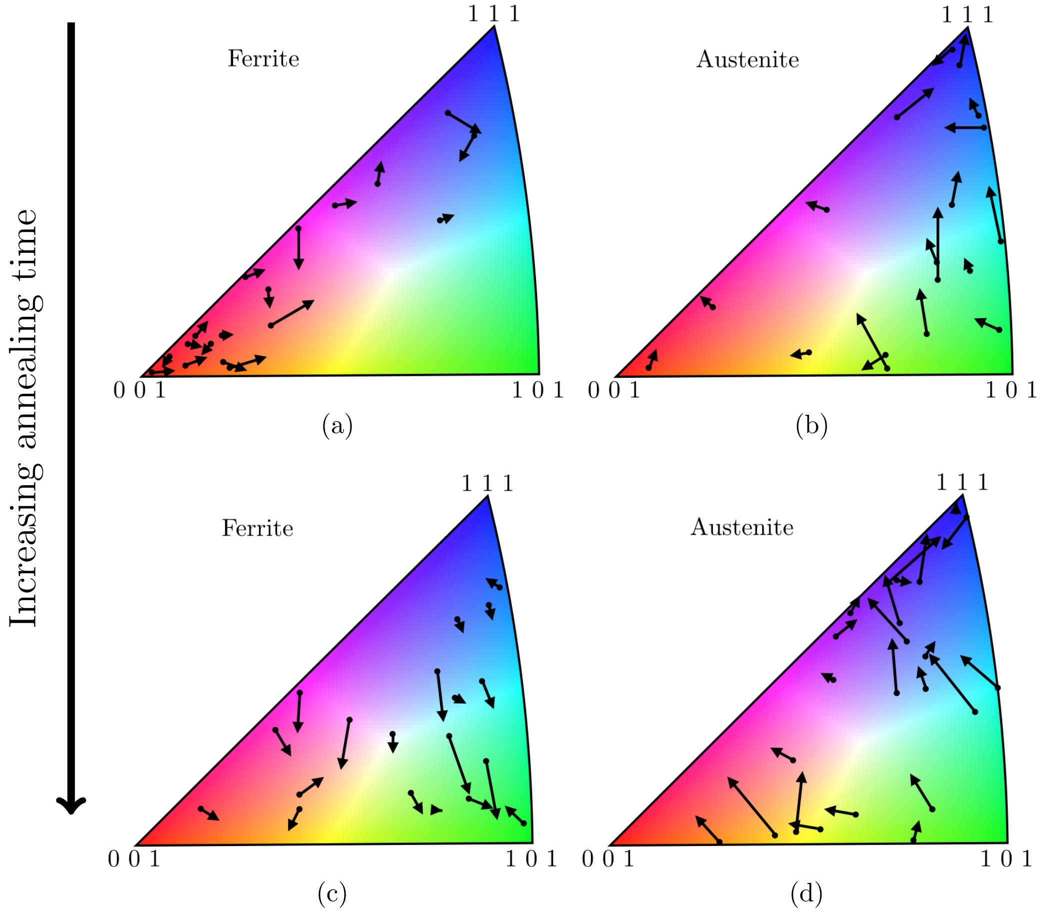

Figure 4.20: Grain rotation in the ferrite and austenite phase before and after tensile testing at 8 % strain. The samples were annealed for (a,b) 0 minutes and (c,d) 14 minutes.

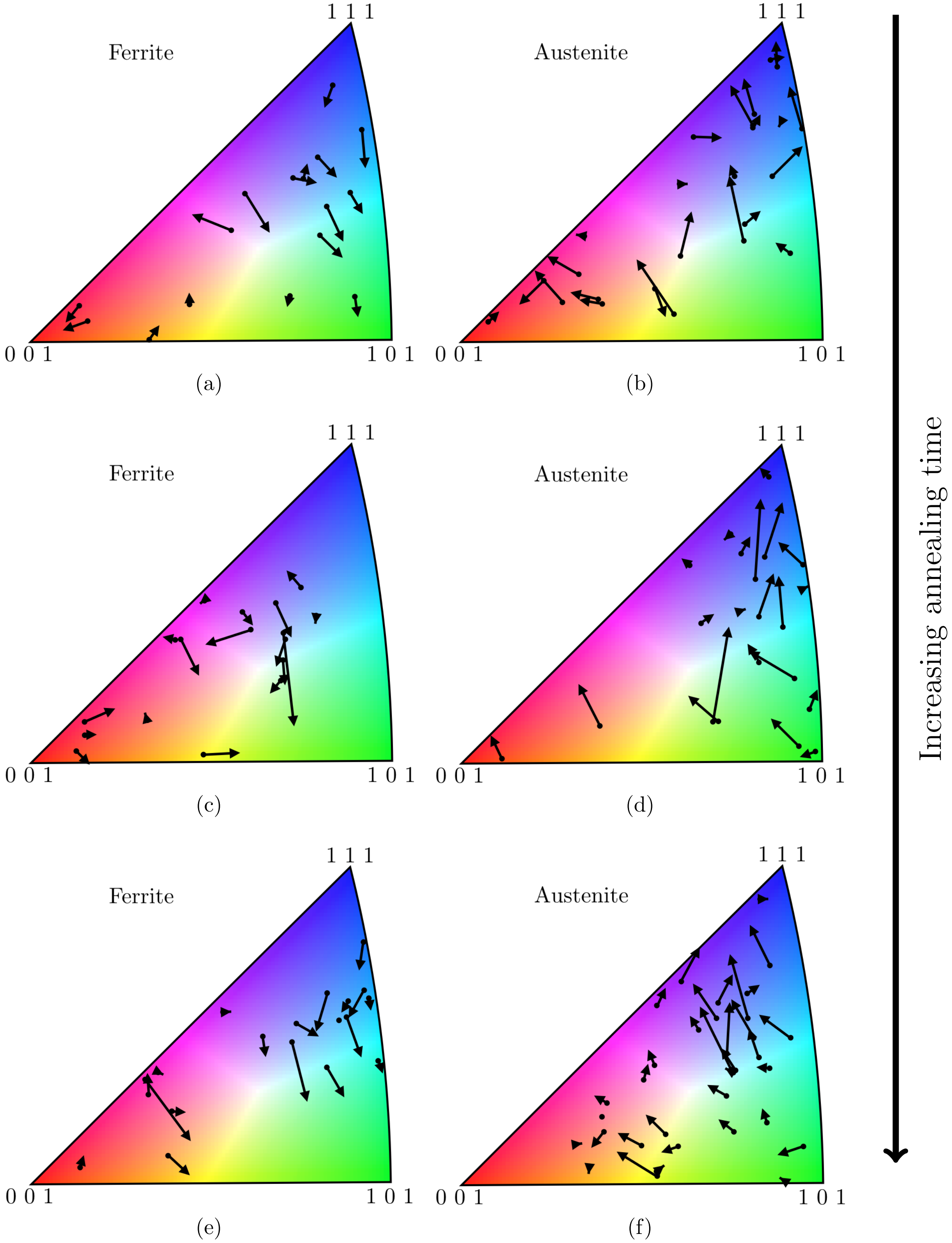

(a) (b)

(c) (d)

(e) (f)

Figure 4.21: Grain rotation in the ferrite and austenite phase before and after strain. The samples were annealed for (a,b) 17 minutes, (c,d) 20 minutes, (e,f) 25 minutes.

4.2.3 Slip

Figure 4.22 shows a SEM image after tensile testing at 8 % strain of the base material. The red square illustrates the ROI used during EBSD investigations. Some interesting slip lines are indicated with red and green arrows for ferrite and austenite, respectively. The slip in the ferrite is of interest and will be discussed in section 5.2.3.

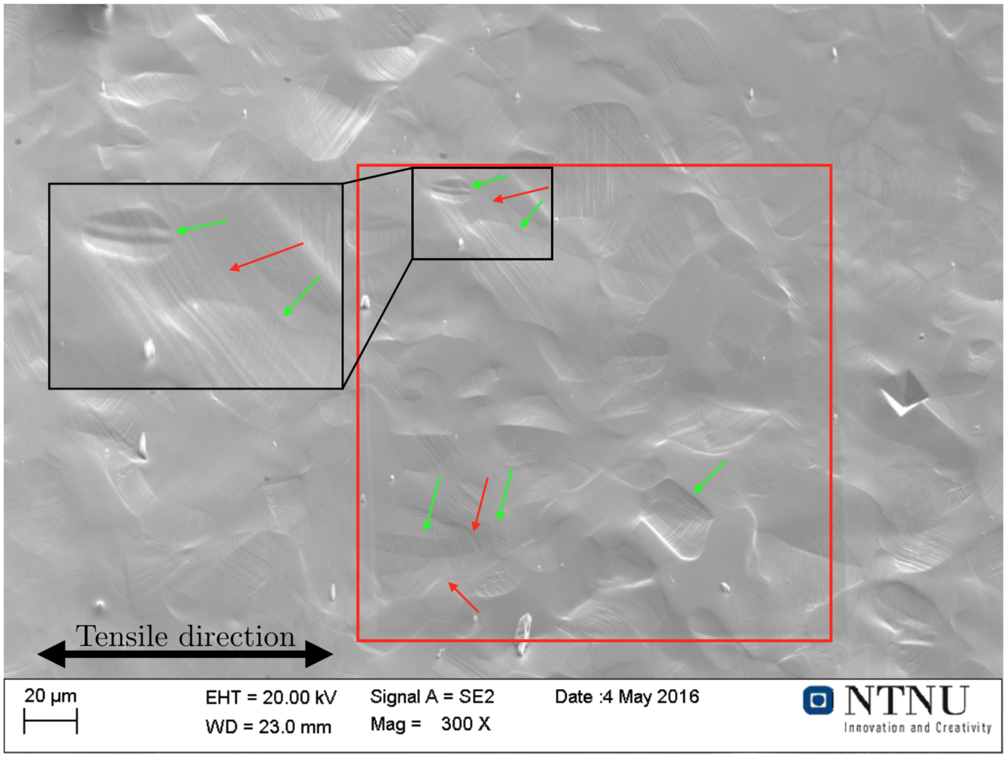

Figure 4.22: SEM image showing slip after 8 % strain in the base material with slip lines indicated with red and green arrows for ferrite and austenite, respectively.

There was observed slip mainly in the austenite as shown in the IQ maps combined with phase maps in Figures 4.23 and 4.24. These maps are hereby only referred to as IQ maps. These IQ maps are from the base material and the material annealed for 25 minutes. At arrow 1 in Figure 4.23e it can be seen slip lines inside the twin in the austenite (green colour). These slip lines continue into the ferrite marked by red colour (see arrow 2). Arrow 3 also shows something that may be a slip line in the ferrite. The rest of the subfigures in Figures 4.23 and 4.24 also show slip lines preferably in the austenite. Some of the most prominent slip lines in the austenite are marked with white arrows in Figure 4.24e.

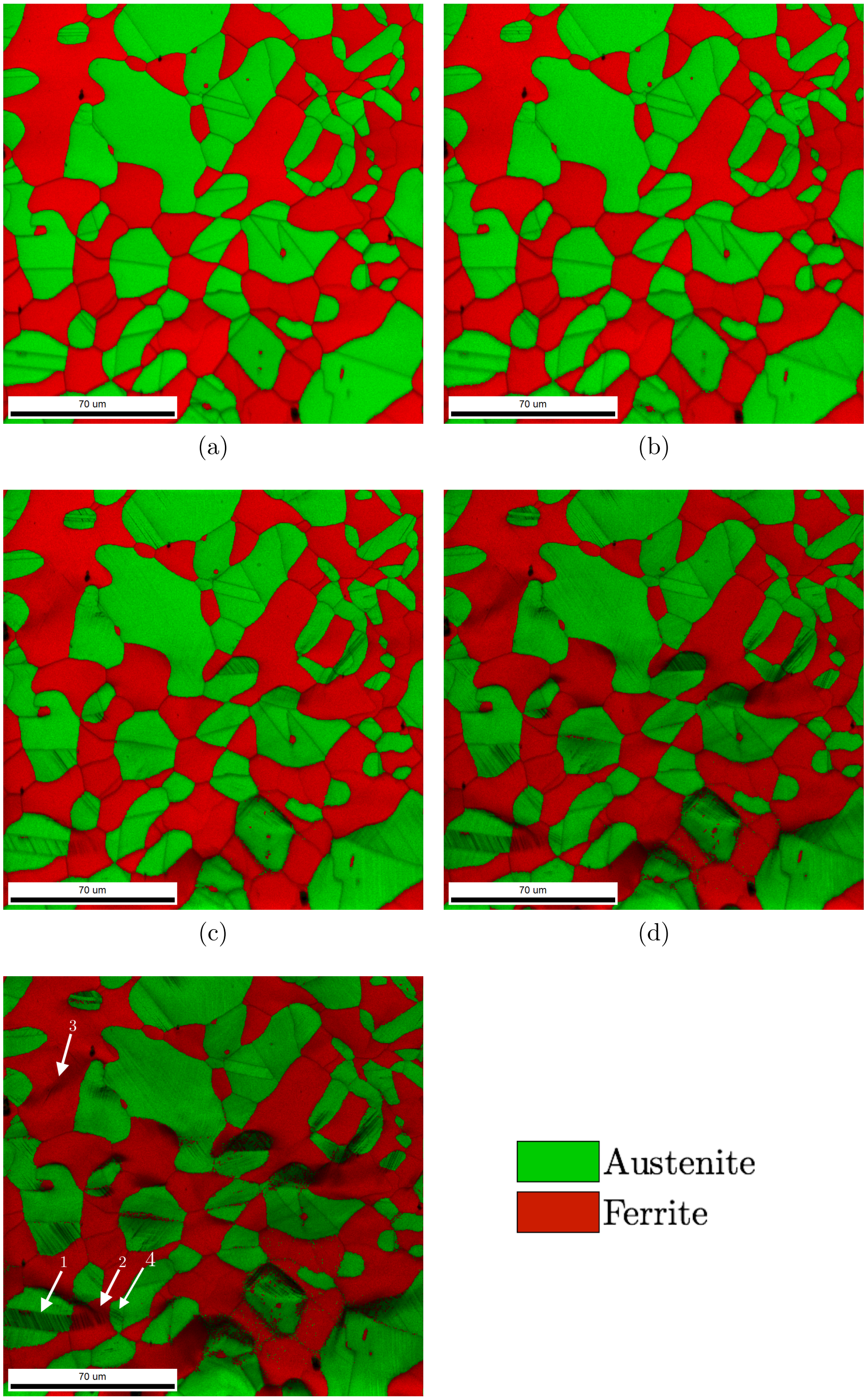

(a) (b)

(c) (d)

(e) (f)

Figure 4.23: IQ maps of the base material with increasing strain where (a) 0 %, (b) 2 %, (c) 4 %, (d) 6 %. (d) 8 % and the legend is given in (f).

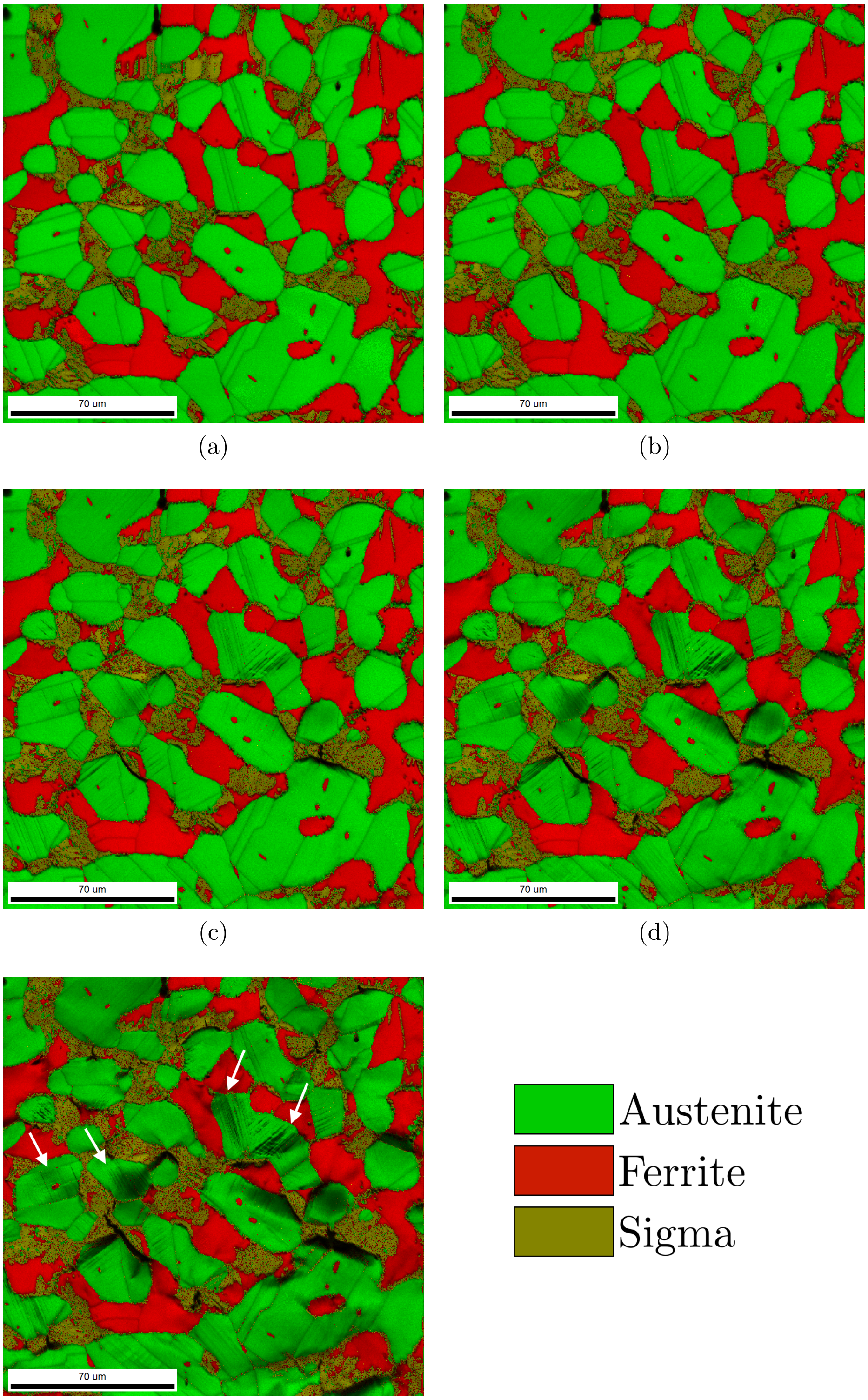

(a) (b)

(c) (d)

(e) (f)

Figure 4.24: IQ maps of the material annealed for 25 minutes containing approximately 13 vol.% sigma with increasing strain where (a) 0 %, (b) 2 %, (c) 4 %, (d) 6 %, (d) 8 % and the legend is given in (f).

4.2.4 Crack initiation

In this section there will be presented some SEM images that show the crack initiation in the material. One sample is presented in this section and the others are presented in Appendix B.11. Figure 4.25 displays SEM images before and after tensile testing at 8 % strain. The tensile direction is in the horizontal direction as indicated with the arrows. The cracks in this specimen are perpendicular to the tensile direction, i.e. vertical cracks in the picture, see highlighted areas. The corresponding IQ map to the cracks in Figure 4.25b is given in Figure 4.24e. From this it can be seen that the cracks propagate in the sigma phase or at the phase boundaries between sigma phase and austenite.

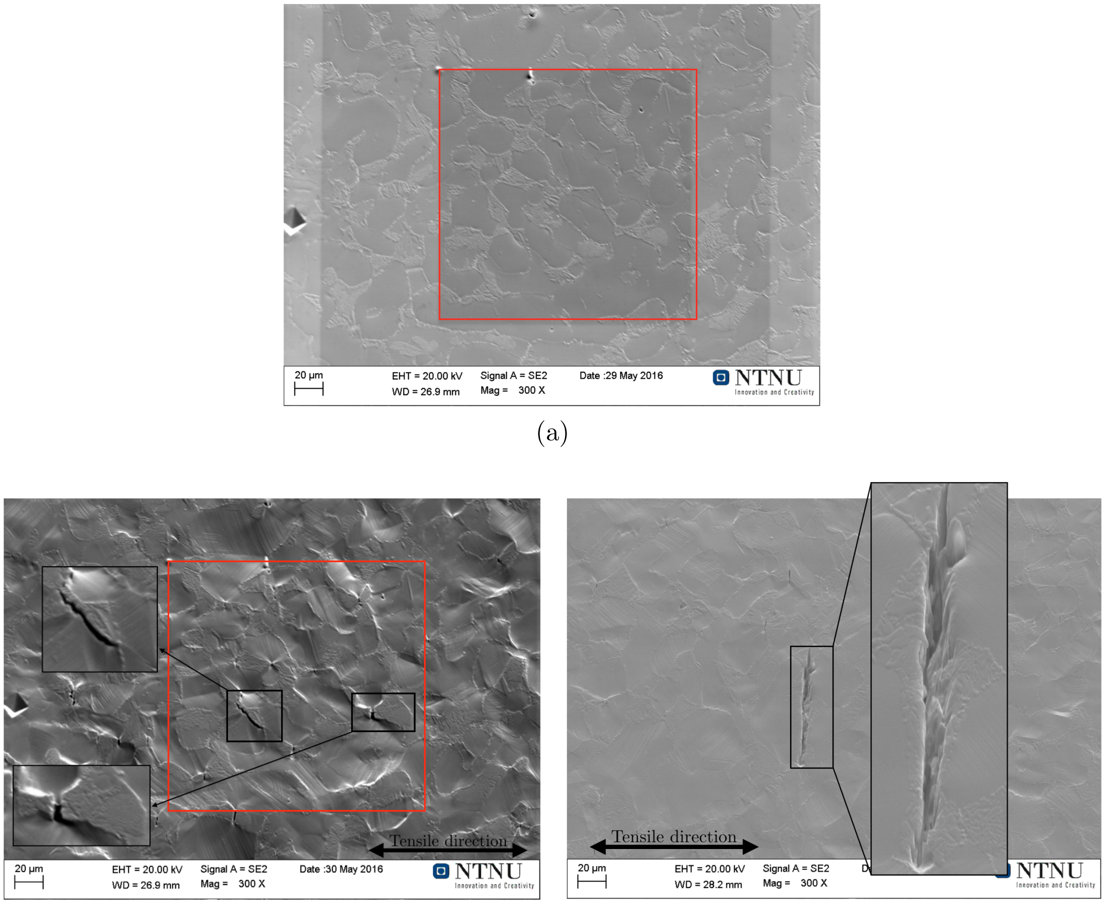

(a)

(b)

(c)

Figure 4.25: SEM image showing specimen surface before (a) and after (b) tensile testing at 8 % strain for the sample annealed for 25 minutes. In (c) one crack for the same material outside the ROI is presented.

5 Discussion

In this part of the thesis the results will be discussed and compared with theory and previous research and investigations. In the first part the material will be thoroughly characterised in regards to the base material in addition to the heat treated material containing sigma phase. The sample preparation is also reviewed along with the effects of parameters in the Hough transformation. The main part of the discussion will concern the in situ tensile testing part primarily focusing on orientation gradients, grain rotation, slip and crack initiation.

5.1 Characterisation of the material

5.1.1 Heat treatment

Heat treatment was performed to characterise the sigma phase in this steel before the in situ examinations, see Figure 4.5. From the figure, it is shown that the sigma phase preferably grows from the ferrite-austenite interface and into the ferrite replacing it. This is in good compliance with the theory presented since the ferrite is richer in Cr and Mo, i.e. ferrite stabilisers. From the theory presented in section 2.1.1 regarding sigma phase formation (Figure 2.5b), the surrounding areas will be depleted of both Cr and Mo. With longer annealing times (Figure 4.5b) the large amount of the ferrite is consumed leaving a structure with larger amounts of austenite and sigma phase. The larger amount of austenite is a result of the formation of secondary austenite during the heat treatment. As presented in the theory this can come from either the direct transformation from ferrite to austenite, or by the eutectoid reaction in Equation 2 in section 2.1.1. This secondary austenite usually contain a lower amount of chromium and is therefore prone to corrosion attacks [10].

From the SEM image before tensile testing given in Figure 4.25a it is evident that the morphology documented in this thesis differs from that reported in an investigation by Pohl et al. (section 2.1.1) [11]. It should be noted that the investigations done in this thesis do not emphasise the different morphologies. As earlier presented in section 2.1.1 the sigma phase morphology is dependent on both annealing time and temperature. The annealing in this thesis was conducted at 850 °C, which should give a morphology similar to Figure 2.6b. However, the sigma phase in this thesis seemed to have multiple nucleation points where the growth from these were coral shaped and quite similar to the one Pohl et al. found, as shown in Figure 2.6 at 750 °C. It should be noted that the annealing time differs between this thesis and investigations performed by Pohl et al. Additionally, it seems like the examination directions differ between the investigations in this these and those performed by Pohl et al. The elongation indicate that the deformation direction is used while this thesis uses examine the transverse direction.

Figure 4.4 shows a plot of the entire heat treatment progress. From the equal initial amount of ferrite and austenite, the ferrite was almost fully consumed after 60 minutes while the austenite content grew to 70 vol.% and approximately 26 vol.% for the sigma phase. The performed area scan (Figure 4.6) indicated that the distribution of sigma was fairly homogeneously distributed in the material. The distribution can become important in deciding the ROI during in situ tensile testing and strongly affects the mechanical properties in the material. The sigma phase has low quality as can be seen from the IQ map in Figure 4.5d where the dark areas indicate sigma phase. This low quality IQ map did most likely come from the sample preparation since there due to the significant difference in pattern quality. Figure 4.9 show how substantial this quality difference is, shows Figures 4.9a and 4.9b are patterns from the austenite and sigma phase, respectively.

5.1.2 Sample preparation

As already mentioned in the theory, sample preparation is very important since the electrons interact close to the surface (20 nm). Two different finalising preparation techniques were tested to improve the pattern quality of sigma phase. In addition to electropolishing with two different electrolytes, chemical mechanical polishing with different suspensions and time is carried out. The electropolishing methods gave a slightly better result when comparing preparation techniques with both IPF maps and IQ maps (Figure 4.8 and Figure A.1). The pattern quality still remained poor after the sample preparation. It is worth to mention that the analysis was not performed on the same sample and had different amounts of sigma phase. This introduce another variable to consider for a finalising preparation technique.

From Figures A.1a, A.1c and A.1d in Appendix A.2 some degree of topography can be seen. This is especially eminent in Figures A.1c and A.1d. These IQ maps were a result of the most chemical active suspension. A reason for the topography can be selective etching of one or more of the phases. In the figures green is austenite, red is ferrite and dark yellow/brown is sigma phase. From this either the ferrite and sigma is experiencing selective etching, or the austenitic phase does not react with this suspension. Some degree of topography can also be seen in the austenitic phase when the sample is electropolished with A2, but not as eminent as with CMP with OP-S suspension. It is also worth mentioning that the OP-S suspension is made for very ductile materials like refractory metals and other non-ferrous metals [32] it can greatly affect the result.

The plotted CI in Figure 4.10 also shows a slight advantage when electropolishing, especially by applying A3 electrolyte. The upper part of the plot contains a total average of all the phases (marked by red circles), the lower part is containing the sigma phase (marked by blue squares). From the figure it can be seen that A3 electrolyte possesses the highest CI in regards to both sigma phase and total average. Since there is not a significant difference in the CI it is not possible to make a strong conclusion, but this may serve as an indication.

5.1.3 Optimisation of parameters

Since the sigma phase experienced low pattern quality the parameters were optimised. As shown in Figures 4.11b and 4.11c the indexing is more reliable after optimisation of the Hough parameters. Both the old and new Hough settings are given in Table 4.2. The most important adjustments done here are the peak count, peak magnitude, peak distance and peak symmetry. These setting strongly influence the indexing time and results

The peak count is adjusted from a minimum and maximum level of 3/7 to 3/14, respectively. To index patterns a minimum of three peaks is needed, i.e. three lines. When setting a maximum value, e.g. 14 peaks the software is allowed to detect more peaks and this setting is very dependent on crystal structure. From the TSL OIM DC software it is stated that for cubic materials seven lines give an acceptable value, but for a monoclinic material it would be normal to detect ten to twelve peaks [27].

The minimum peak magnitude was lowered from five to one. The peak magnitude sets a minimum necessary magnitude for the peak in Hough space to be detected as a peak. This means that since this value is lowered, more peaks will be considered as potential peaks in the Hough space. The minimum peak distance sets the required distance between detected peaks in the Hough space, given in pixels. Since the peak distance was lowered, the Hough transformation will require shorter distances between potential peaks. The peak symmetry decides how symmetric the peaks need to be, where a lower value demands more symmetric peaks. Since the peak symmetry was increased from 0.50 to 0.70 the Hough transformation allows less symmetric peaks.

5.2 In situ tensile testing

In this section the performed in situ tensile testing will be thoroughly discussed focusing on orientation gradients, grain rotations and slip activity. These characteristics will be discussed and compared with relevant theory and also previous investigations performed on other materials with a similar crystal structure.

Table 4.3 shows an overview of the amount of sigma phase in the specimens used during the in situ tensile testing. All of these specimens were heat treated at 850 °C and the corresponding temperature vs. time curve is shown in Figure 4.12. The steel needed some minutes to reach the precipitation temperature. Since the amounts of sigma, ferrite and austenite are given in this thesis this can neglected.

The stress strain curves from the tensile testing are given in Figure B.8, Appendix B.8. The offset yield stress and the calculated Young's modulus are given in Table 4.4. The offset yield stress and Young's modulus were found to be around 60 MPa and 30 GPa, respectively. From this it is evident that the offset yield stress differs from the material's standards presented in Table 2.1 which is supposed to be 550 MPa and 200 GPa, respectively. From the stress strain curve it can be seen that the yield point is located at approximately 2 % strain which corresponds to a factor of 10 displacement. There was performed measurements of the elongation, and these were correct. One possible cause for these measurements may be a software related issue.

5.2.1 Orientation gradients

Figure 4.13 shows IPF maps of the base material with increasing amounts of strain. From Figure 4.13a some degree of misindexing can be seen inside the green grain marked with a white arrow. This phenomena is called pseudo-symmetry. The orientation difference between the purple orientation and the green orientation is 30° around the [111] axis. This is also characteristic for pseudo-symmetry [35, 36]. This pseudo-symmetry can occur when the solid angle gets too small and the <111> zone axis is in the middle of the pattern. For the remainder of the thesis this problem was minimised by increasing the working distance and moving the EBSD detector closer to the specimen. From the other IPF maps there are only some misindexing in the sigma phase which is caused by pattern quality and not a pseudo-symmetry problem.

From the IPF map of the base material in Figure 4.13, which does not contain any sigma phase, one example of misorientation can be seen. Close to the [111] direction (red colour in the IPF) marked with black circles, formation of some degree of orientation gradients is observed. This is characterised by colour changes within the grains in the IPF. When comparing this IPF map with the IQ map in Figure 4.23 it can be stated that orientation gradient formation come from both the austenitic phase and the ferritic phase. These orientation gradients are not applicable only for these directions and may also occur for other directions.

After the formation of sigma phase in the steel (see Figure 4.14), it seems like there are more orientation gradients. The black circles in Figure 4.14e indicate areas which contain the most prominent orientation gradients in the sample annealed for 25 minutes containing 13 vol.% sigma after tensile testing. As known from the theory, grains in metals experience heterogeneous strain. One reason for larger amounts of orientation gradients in the presence of sigma phase may be caused of the heterogeneous strain is enhanced by the hard and brittle sigma phase. This is only a visual observation and cannot be quantified at this time since there is not enough data to perform quantified analysis. Figures 4.19b and 4.19a present a plot of some misorientation measurements. These misorientation plots quantify how significant the misorientations within the grains can be.

Figures 4.17 and 4.18 give a closer look of the orientation gradients within selected grains. In these plots the lines indicate orientations referred to the IPF. A further description of the areas in which the misorientations are extracted form is given in Appendix B.9. The orientation gradients does not decide alone the degree of deformation. As can be seen in Figure 4.19b the misorientations are measured for the grain in which did not contain a significant amount of orientation gradients. Grain F11, annealed for 17 minutes (see Figure 4.17e) reaches a misorientation of 6°. This is however significantly lower than for the grains with large orientation gradients, but indicate that there is a formation of internal misorientations.

From the base material there are more orientation gradients within the austenitic grains, especially for the [101] direction in austenite. Since austenite experiences more orientation gradients, it can be assumed that it gets more deformed than the ferritic phase. This is in good compliance with the theory since the lattice structure in austenite is more densely packed, i.e. more operable slip systems. From investigations done on aluminium, which consist of the same crystal structure as austenite (FCC), the crystals tend to obtain certain orientation configurations.

In an investigation by Bjerkaas [21] performed on aluminium showed that the [001] and [111] directions parallel to the tensile direction tend to rotate against the poles of the IPF, while the [101] direction parallel the tensile direction was stated as an unstable configuration. The [101] direction tend to rotate against the [001] and [111] directions, but also against $[\bar{1}12]$ direction. From the base material it can seem like there is a connection to the rotation behaviour between the similar crystal structures.

It is important to ascertain the grain positions before the tensile testing. Figure 5.1a shows the grain orientation for the austenitic phase in the base material after tensile testing. Grain

A3 (marked with red colour before tensile testing) shows some misorientation within the grain before tensile testing and this can affect the results. From the misorientation plot in Figure 4.19a this grain is further investigated and achieve a misorientation of 10° from the original misorientation measurements in the grain. However, it can be seen that the grain does not tend to obtain a certain orientation configuration as shown by the white arrows. These arrows are drawn as an illustration.

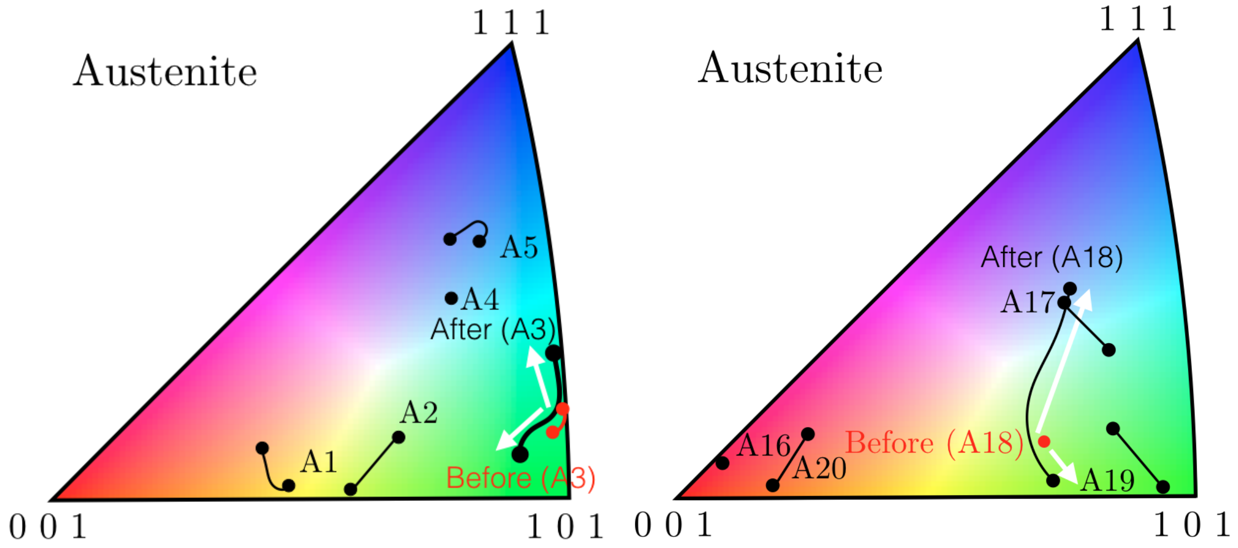

(a) (b)

Figure 5.1: Orientation gradients inside selected grains after tensile testing with grain of interest before tensile testing was conducted.

In the austenitic phase for the sample annealed for 20 minutes (see Figure 4.18b) a different correlation can be seen. Figure 5.1b shows the orientation distribution after tensile testing with the grain of interest (A18, marked with red colour before tensile testing). From this it is evident that the rotations within the grains are leaving the [101] area and are directed towards the [111] direction which is shown by the white arrows. These arrows are drawn as an illustration. This is in accordance with the investigations from Han et al. [1] on aluminium. This grain is also included in the misorientation plot in Figure 4.19a where it achieve the highest misorientation measured. The misorientation from one side to another in the grain almost reached 20° which corresponds to a high angle grain boundary (>15°). Common for the investigation for both grains is that they are both close to the [101] direction which is characterised as an unstable direction for FCC crystal structures.

It should be noted that this is just the misorientation within the grains and should not be mistaken with grain rotation. Before tensile testing the misorientation in the grain is close to zero, but after tensile testing the misorientation in the grain changes which shows the effect of heterogeneous strain. There are also only a couple of grains used in this misorientation analysis (10 grains from each sample). The actual grain rotation study is evaluated in section 5.2.2, but the knowledge of the misorientation within the grain is important which will be discussed during the section.

In ferrite the misorientation within the grains are not as prominent as in austenite. This is also in good compliance with theory since ferrite (BCC) contains fewer operable slip systems. Since plastic deformation mainly occurs by slip the misorientation will be reduced. Hence less plastic deformation. There is however some grains that clearly get deformed. Especially grain F18 in Figure 4.18a undergoes a large deformation where there is a misorientation between blue and red which corresponds to 11° from start to end. Figure 5.2a provides a better illustration of the misorientation profile. Grain F18 (marked with red colour before tensile testing) has an internal rotation from the [111] direction and towards the [101] direction as can be seen by the white arrows. These arrows are drawn as an illustration. This is the opposite rotation behaviour of the FCC crystal structure (Figure 2.12b) of that described in theory.

Grain F16 in this sample also undergoes a certain deformation, (see Figure 4.18a) and experiences 13° misorientation from start to end. This grain is further investigated in Figure 5.2a. The blue spot in the figure indicates the orientation position before tensile testing. From the drawn white arrows it can be stated that the grain rotates in two directions, i.e. towards [001] and [111]. This is however a bit strange behaviour that the grain tend to rotate from the stable [001] direction. The overall rotation direction cannot be described since the grain ”bends” in two directions. With further deformation it can be assumed that the grain will split in two or more grains, i.e. subgrains. Grain F23 in Figure 4.18c also shows large misorientations. When comparing with the orientation before tensile testing (marked with red colour in Figure 5.2b) it can be stated that the grain rotates in two directions. This is the same correlation as with grain F16 in Figure 5.2a.

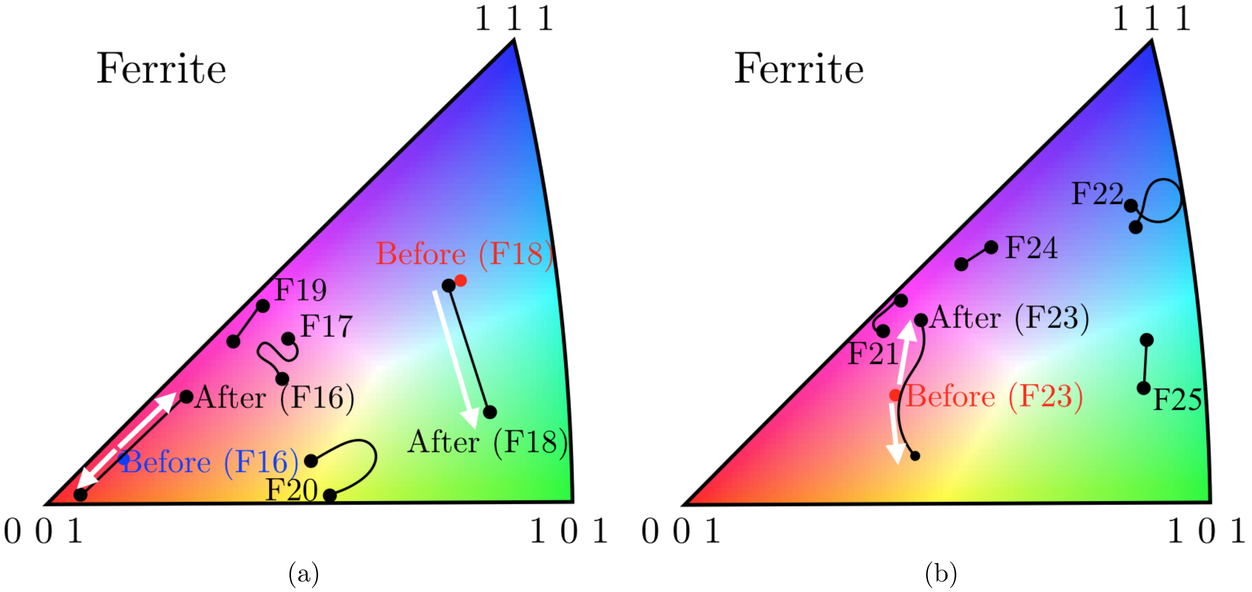

(a) (b)

Figure 5.2: Orientation gradients inside selected grains after tensile testing with grain of interest before tensile testing.

As already stated this concerns the misorientation within the grains, but this gives an indication of how the grains tend to rotate. There are various factors that decide the rotation behaviour of polycrystalline materials such as steel and aluminium the initial orientation, grain size and also neighbouring grains serve as some examples. It is well established that austenite is more ductile than ferrite. From an investigation presented by Bjerkaas [21] it is stated that polycrystalline materials are able to consist of both soft and hard grains. The soft grains have to compensate for the lack of plastic deformation in the hard grains. This deformation effect can explain the amount of plastic deformation in the austenite when compared with ferrite.

5.2.2 Grain rotation

The grain rotation study gives viable information and describes how the grains rotate during tensile testing. This study is different from the misorientation study since grain rotation focuses on the overall rotation before and after tensile testing where internal rotations are not considered. In this study mainly one spot in the grain is reviewed. However, as orientation gradients developed the orientation from multiple places were used, but mainly one point in the middle of the grain was used as a reference. Similar investigations have also been carried out in a previous master's thesis performed by Randi Mørkved [37]. This was however performed on aluminium alloys.

The results from the grain rotation study performed in this thesis are given in Figures 4.20 and 4.21. From this it can be seen that the austenitic phase rotates from the [101] pole towards the [111] direction or the area that connects the [111] and the [001] directions, i.e. $[\bar{1}12]$. On the other hand, ferrite tend to rotate from [001] and [111] directions against the [101] direction. This correlation was not very notable but somehow visible in the misorientation study, but there is a more prominent relationship when studying the overall grain rotation.

From the austenitic phase in Figures 4.20 and 4.21 there is a clear correlation between aluminium alloys and the austenite. Investigations from Han et al., Bjerkaas and Mørkved [1, 21, 37] all showed the following grain rotation correlation:

- Grains with a [001] direction contain a stable orientation that does not rotate and other orientations tend to rotate against this orientation.
- Grains with [101] direction tend to rotate towards the $[\bar{1}12]$ pole.
- Grains around the $[\bar{1}12]$ pole tend to rotate towards the [111] direction.

Figure 5.3 compares the investigations done in this thesis with the sample annealed for 25 minutes (Figure 5.3a) and investigations done by Han et al. (Figure 5.3b). There is a clear correlation between these two investigations which were performed on two different materials (aluminium alloy 1050 and SDSS). The white arrows in Figure 5.3a indicate the correlation in which the rotation tend to rotate towards the $[\bar{1}12]$ and [111]. It is important to note that the white arrows is not the grain rotation but an estimated correlation. These rotations show a good accordance to what Han et al. discovered and also the theoretical rotation in a FCC single crystal (Figure 2.12a). In this sample there was not any grains oriented in the [001] direction. This can be found in Figure 4.20d where the sample was annealed for 14 minutes. From the figure it cannot be seen any clear correlation for this crystal direction, but like aluminium there is no big rotation close to the [001] direction. There is not enough data to determine the rotation behaviour in close proximity of the [001] direction.

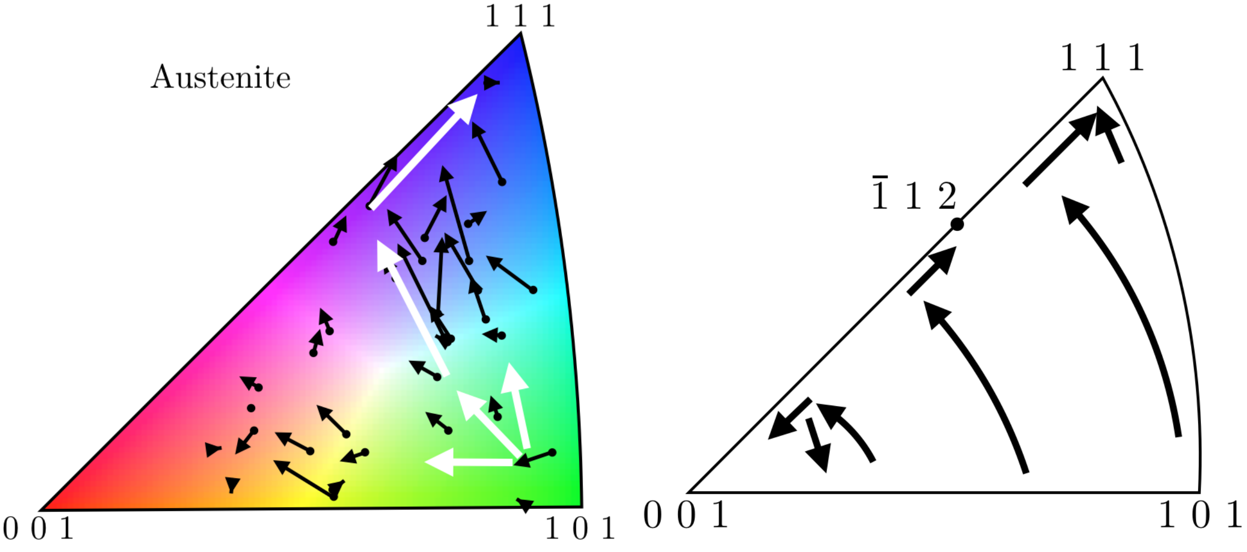

(a) (b)

Figure 5.3: Grain rotation study performed in (a) the austenitic phase in this thesis and (b) the study by Han et al.[1]

This rotation behaviour was not observed in the ferrite. The rotation in the ferritic phase is given in Figures 4.20 and 4.21. It can be seen that the rotation behaviour in ferrite is the opposite of austenite and aluminium. Both austenite and aluminium tended to rotate from the [101] direction and towards [111] and [$\bar{1}$12] directions while ferrite tended to rotate towards the [101] direction. Figure 5.4 summarises these investigations with two different annealing times. In Figure 5.4a the rotations in the base material are given where it can be seen that there were mostly [001] orientations. The grains tended to rotate from the [001] direction (see white arrow). Figure 5.4b shows that the rotation from the [111] direction tended to rotate against the [101] direction which indicate that the rotation behaviour in BCC materials also is very dependent on initial orientation. From investigations performed on both austenite and ferrite it can be seen that the rotation behaviour is dependent on both the initial orientation and the crystal structure which also is the case for aluminium.

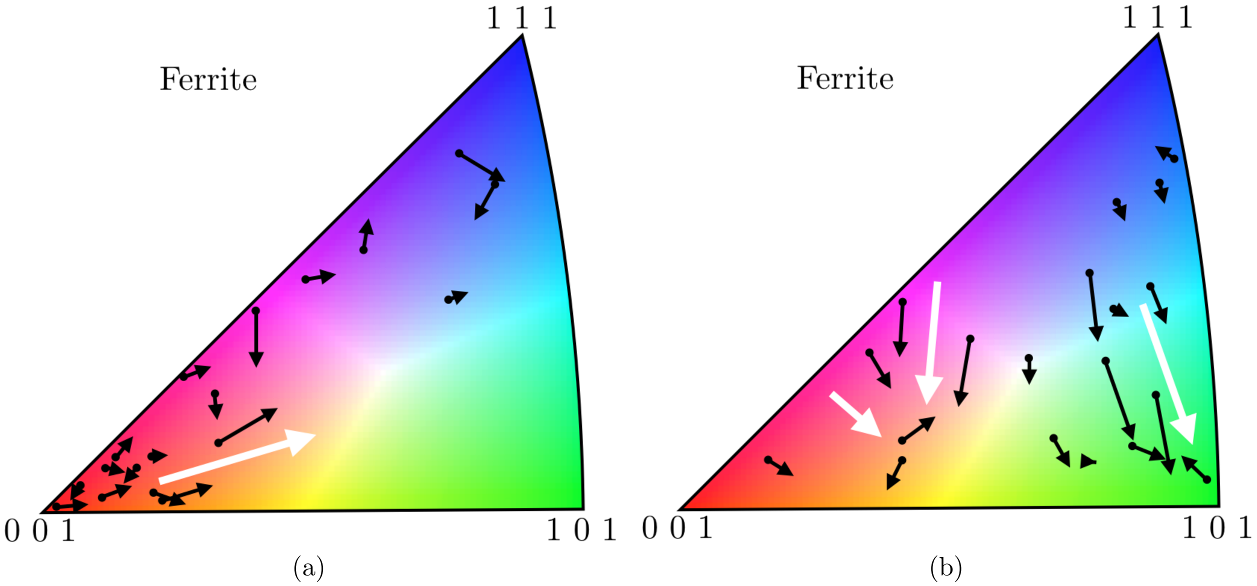

Figure 5.4: Grain rotation study performed in the ferritic phase in (a) base material and (b) material annealed for 14 minutes.

5.2.3 Slip

Figures 4.23 and 4.24 show IQ maps of the base material and the material annealed for 25 minutes with 0 vol.% and 13 vol.% sigma, respectively. From these figures there are shown many slip lines which occur mainly in the austenite, but a few also occur in the ferrite. The arrows in Figure 4.24 show prominent slip lines preferably in the austenite. Slip is important for understanding the deformation behaviour in materials since plastic deformation mainly occurs by slip. Arrow 3 in Figure 4.23e shows something that can be a slip line in ferrite. As known from the theory ferrite has fewer operable slip systems than austenite, which counteract the plastic deformation. With the use of plane trace in EDAX/TSL OIM Analysis the location of a slip plane is possible to trace. From this it may seem like the slip takes place at the (211) plane. To determine whether this is a slip in the (211) or not, there is need for more investigations at higher strains than examined in this thesis.

From Figure 4.23e slip inside a twin in the austenite phase can be seen, indicated by arrow 1. This slip continues across the grain boundary and through the ferritic phase, only with a change of direction and further into a new austenite grain, see arrow 2 and 4. In Figure 5.5 this area is cropped and a plane trace is given for the (111) and (211) planes in Figure 5.5a and Figure 5.5b, respectively. The slip in the new austenite grain (arrow 4, Figure 4.23e) is not presented, but slip in the (111) plane is indicated by applying trace analysis.

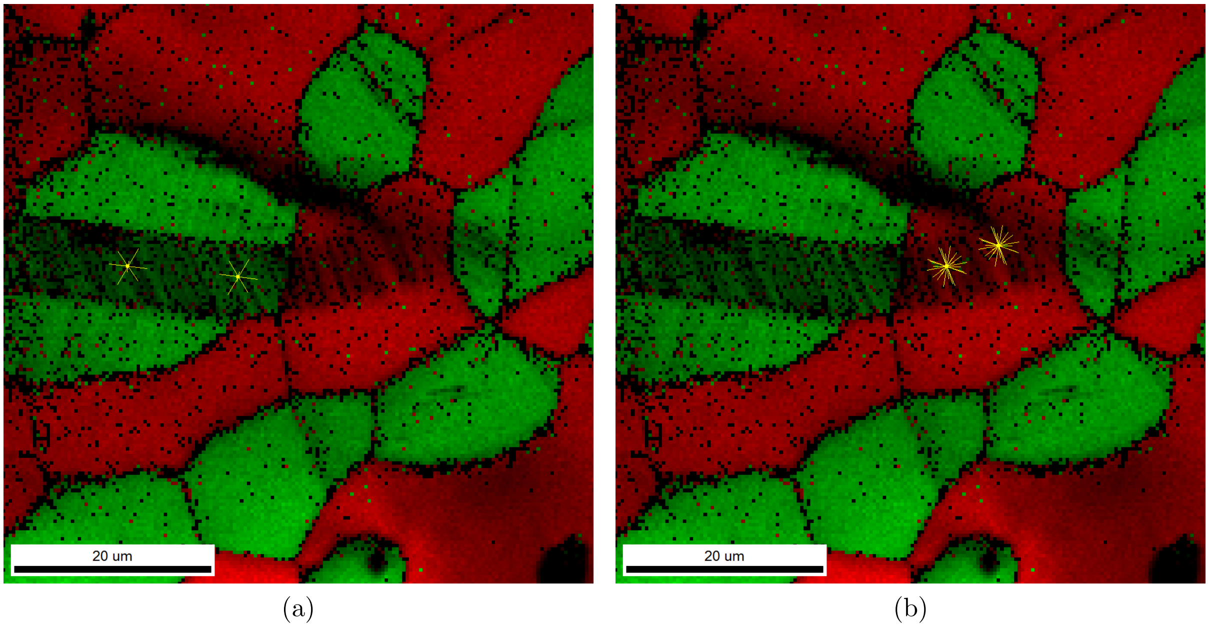

(a) (b)

Figure 5.5: Slip trace analysis in the austenite and ferrite where (a) shows the (111) plane and (b) shows the (211) plane.

The plane trace presented in Figure 5.5 shows the (111) and (211) plane trace in the IQ map. This plane trace gives an indication on whether the slip is in the actual plane, but can give several solutions. In order to state that this is the correct plane, more investigations are necessary. Previous experiments by Fréchard et al. [18] have shown that in DSS the austenite experiences slip even at low levels of strain where these evolved to be homogeneously distributed with increasing strain. For ferrite, only a few signs of plastic deformation were documented. However, when there was induced plastic deformation in the ferritic phase two mechanisms were detected:

- Dislocation pile up at the phase boundary which creates local shear stresses. This further generated dislocations in the ferrite which lead to plastic deformation.
- Neighbouring austenite grains can cause a shearing effect in ferrite when dislocations accumulate in the austenite.

From Figure 5.5 the slip is transferred across phase boundaries from austenite → ferrite → austenite. The mechanism behind this slip activity in both austenite and ferrite is not known, but can consist of one of the theories listed above. This also occurs at multiple places in the base material. In addition to the slip indicated by arrows 2 and 3 in Figure 4.23 there is found slip lines in the SEM image (Figure 4.22). In the figure, the green lines are slip in austenite and the red lines are slip in the ferrite. These were not visible in the EBSD scan. Therefore, no further investigation by plane trace in EDAX/TSL OIM Analysis was possible. Figure 5.6 shows a cropped picture of the SEM image in Figure 4.22 and the corresponding IQ map which made phase indication possible. These slip lines show the same phenomena as presented in Figure 5.5.

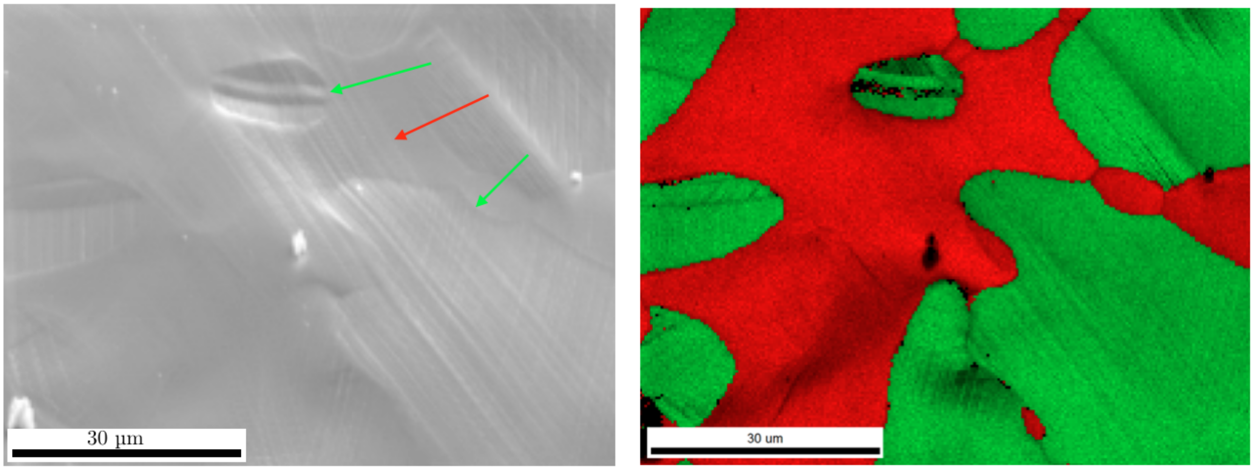

(a) (b)

Figure 5.6: Cropped SEM image from Figure 4.22 and a cropped IQ map from Figure 4.23. The SEM image shows slip in austenite and ferrite, while the IQ map gives the corresponding phase distribution.

This only occurred in the base material which did not contain any sigma phase. One reason may be that since the sigma phase grows in close proximity of the ferrite and tend to crack at large deformation, it is conceivably that the tensions in the ferrite are reduced. When the tensions in the ferrite are reduced the few dislocations which form are not sufficient to cause plastic deformation and slip. It should be done more investigations on the base material to to obtain a deeper understanding of the difference in slip with and without sigma phase.

From this it can be seen that the deformation in the ferrite is less prominent, i.e. reduced grain rotation and misorientation. From this it can be assumed that the austenite experiences more deformation than the ferrite, which also is supported by basic materials science.

5.2.4 Crack initiation

There were performed investigations of the cracks in the material after the in situ tensile testing. Figure 4.25 shows an example for the specimen annealed for 25 minutes. Before tensile testing (Figure 4.25a) there were not observed any cracks. After tensile testing (Figure 4.25b) cracks evolved inside the ROI. Figure 4.25c also shows a crack in the same specimen at another location. This crack was measured to be 85 μm. Common for all of the cracks after tensile testing was that they propagated in or around the sigma phase since the sigma phase is brittle, which has been covered in the theoretical background, see section 2.1.1. This is shown with the corresponding IQ map in Figure 4.24e. The crack in Figure 4.25a does not have any IQ map, but from the morphology shown in the SEM image strongly indicate that this crack is in the sigma phase.

There are given SEM images of the surface after tensile testing in Appendix B.11. From this it can be seen that the sigma phase preferably cracks perpendicular to the tensile direction, which also is consistent with brittle fractures. The corresponding IQ map for the cracks in Figures B.11a and B.11b is given in Figures B.6 and B.7, respectively. From this it can be stated that the cracks propagate in the sigma phase. However, one of the cracks is located outside the ROI, but the morphology strongly indicates that this takes place in the sigma phase. The indexed sigma phase has a poor pattern quality, and hence the crack initiation cannot be examined in detail. It would have been exiting to establish if the deformation behaviour in the ferrite and austenite affect the crack propagation in the sigma phase. Furthermore, it would have been interesting to examine the effect of grain size and the grain orientation for the cracking behaviour.

5.3 Further Work

- Extensive work on the nucleation and growth of the sigma phase. With the available in situ heating equipment this can be accomplished.
- There is need for more extensive work on the sample preparation issue for indexing of the sigma phase. Ion sputtering and vibratory polishing can be a solution. Vibratory polishing has previously given better results on the indexing of sigma phase [38]. This was however not a technique present at the department when this project was carried out.
- There is need to improve the tensile equipment used in this thesis. The stress-strain relationship in this thesis differ from material standards. When calculating the Young's modulus there was an error of almost a factor of 10 difference between data sheets and the calculated value. One possibility can be the elongation measurement since there was not performed any quantified measurements in this thesis. However, the measurements done indicated that the elongation was correct. Another possibility can be a software related issue.
- There is a need for more extensive investigations on the deformation mechanisms during tensile testing. More investigations are needed to state the effect of grain size and neighbouring grains. Also, with an indexable sigma phase, the crack propagation can be examined, e.g. initiation in austenite or ferrite, effect of grain size and neighbouring grains etc. The different mechanisms for occurrence of slip in austenite and ferrite may be of interest for further investigations.
- Slip in the austenite occurred at low levels of strain for all the specimens, but slip in the ferrite only occurred in the not heat treated base material. The slip activity in the base material can be further investigated to determine the effect of sigma phase for slip in the ferrite.

6 Conclusions

In the present thesis SDSS containing sigma phase has been investigated. The main objective has been to investigate and understand the deformation behaviour in SDSS with and without sigma phase. This knowledge has been obtained by discussing the experimental investigations and by comparison with previously performed experiments. Based on the experimental procedures these conclusions can be drawn:

- There were found significant differences for the deformation behaviour in the austenitic and ferritic phases.
  - The deformation in SDSS was strongly dependent on its crystal structure.
  - The amount of observed deformation was higher in the austenite than in the ferrite.
- The grain rotations was found to be most dependent on the initial orientation during simple tensile in the tensile direction.
  - The grain rotation in austenite tended to follow the rotation behaviour of a FCC single crystal and similar rotation behaviour found in other FCC structures, e.g. aluminium. The rotation in the austenite phase tended to rotate from the [101] direction and towards the [$\bar{1}$12] and [111] directions.
  - Ferrite did not follow the same rotation behaviour as austenite. Ferrite tended to rotate against the [101] direction.
- Slip occurred across phase boundaries during tensile testing. The slip discussed in the base material crossed boundaries in the order austenite → ferrite → austenite.
- The crack propagation in the material was investigated. There were only found cracks in the sigma phase and not in the ferrite or austenite. The cracks in the material followed a classical brittle nature and propagated perpendicular to the tensile direction.
- The sigma phase appeared to have multiple nucleation points and seemed to grow with a coral like behaviour from these nucleation points.
- There were not found a optimal sample preparation technique and further investigations are required. Both chemical mechanical polishing and electropolishing did not seem to be suitable for indexing the sigma phase.

7 References

[1] Jun-Hyun Han, Kwang-Koo Jee, and Kyu Hwan Oh. Orientation Rotation Behavior During In Situ Tensile Deformation of Polycrystalline 1050 Aluminum Alloy. *International Journal of Mechanical Sciences*, 45(10):1613 – 1623, 2003. 6th Asia-Pacific Symposium on Advances in Engineering Plasticity and its Applications.

[2] International Molybdenum Association. Practial Guidelines for the Fabrication of Duplex Stainless Steels. Technical report, International Molybdenum Association, 2014.

[3] Langley Alloys Super Duplex UNS S32760, May 2016.

[4] Harry Bhadeshia and Robert Honeycombe. *Steels - Microstructure and Properties (3rd Edition)*. Elsevier, 2006.

[5] M. Rosso, I. Peter, and D. Suani. About Heat Treatment and Properties of Duplex Stainless Steels. *Journal of Achievements in Materials and Manufacturing Engineering*, 50(1):26–36, July 2013.

[6] Yoon-Jun Kim. *Phase Transformations in Cast Duplex Stainless Steels*. PhD thesis, Iowa State University, 2004.

[7] Jorge L. Garin and Rodolfo L. Mannheim. Rietveld Quantitative Analysis of Super Duplex Stainless Steels. *JCPDS-International Centre for Diffraction Data 2012*, 2012.

[8] Chih-Chun Hsieh and Weite Wu. Overview of Intermetallic Sigma (σ) Phase Precipitation in Stainless Steels. *International Scholarly Research Network ISRN Metallurgy*, 2012.

[9] Zbigniwe Stradomski and Dariusz Dyja. Sigma Phase Precipitation in Duplex Phase Stainless Steels.

[10] J-O Nilsson. Super Duplex Stainless Steels. *Materials science and technology*, 8(8):685–700, 1992.

[11] Michael Pohl, Oliver Storz, and Thomas Glogowski. Effect of Intermetallic Precipitations on the Properties of Duplex Stainless Steel. *Materials Characterization*, 58(1):65 – 71, 2007.

[12] M Schwind, J Källqvist, J.-O Nilsson, J Ågren, and H.-O Andrén. σ-Phase Precipitation in Stabilized Austenitic Stainless Steels. *Acta Materialia*, 48(10):2473 – 2481, 2000.

[13] K.H. Lo, C.H. Shek, and J.K.L. Lai. Recent Developments in Stainless Steels. *Materials Science and Engineering: R: Reports*, 65(4–6):39 – 104, 2009.

[14] Yutaka S Sato and Hiroyuki Kokawa. Preferential Precipitation Site of Sigma Phase in Duplex Stainless Steel Weld Metal. *Scripta Materialia*, 40(6):659 – 663, 1999.

[15] T. Børvik, H. Lange, L.A. Marken, M. Langseth, O.S. Hopperstad, M. Aursand, and G. Rørvik. Pipe Fittings in Duplex Stainless Steel With Deviation in Quality Caused by Sigma Phase Precipitation. *Materials Science and Engineering: A*, 527(26):6945 – 6955, 2010.

[16] William D. Callister and David G. Rethwisch. *Materials Science and Engineering*. John Wiley & Sons Ltd, 2011.

[17] Thomas H. Courtney. *Mechanical Behavior of Materials*. McGraw-Hill Science/Engineering/Math, 1999.

[18] S. Fréchard, F. Martin, C. Clément, and J. Cousty. AFM and EBSD Combined Studies of Plastic Deformation in a Duplex Stainless Steel. *Materials Science and Engineering: A*, 418(1–2):312 – 319, 2006.

[19] Valerie Randle and Olaf Engler. *Introduction to Texture Analysis: Macrotexture, Microtexture and Orientation Mapping*. CRC Press, 2000.

[20] P. Chen, S.C. Mao, Y. Liu, F. Wang, Y.F. Zhang, Z. Zhang, and X.D. Han. In-situ EBSD Study of the Active Slip Systems and Lattice Rotation Behavior of Surface Grains In Aluminum Alloy During Tensile Deformation. *Materials Science and Engineering: A*, 580:114 – 124, 2013.

[21] Hans Bjerkaas. *Characterisation and Plasticity in Extruded Al-Mg-Si Profiles engaging In-situ EBSD*. PhD thesis, Norwegian University of Science and Technology (NTNU), June 2007.

[22] R Sedláček, W Blum, J Kratochvil, and Samuel Forest. Subgrain Formation During Deformation: Physical Origin and Consequences. *Metallurgical and Materials Transactions A*, 33(2):319–327, 2002.

[23] Adam J. Schwartz, Mukul Kumar, Brent L. Adams, and David P. Field. *Electron Backscatter Diffraction in Materials Science*. Springer, 2010.

[24] Jarle Hjelen. Scanning Electron-Mikroskopi. Kompendie, Metallurgisk institutt, NTH, August 1989.

[25] Oxford instruments. Electron Backscatter Diffraction Explained. 2004.

[26] Dejan Stojakovic. Electron Backscatter Diffraction in Materials Characterization. *Processing and Application of Ceramics*, 2012.

[27] Edax. *OIM DC 7.2*.

[28] EDAX. *OIM Analysis Tutorials*. EDAX.

[29] Kim Ronny Elstad, Børge Sognnæs Andresen, Morten Karlsen, Ida Westermann, and Jarle Hjelen. The Effect of Sample Preparation on Quantification of Retained Austenite in Supermartensitic Stainless Steel Studied by EBSD and XRD. *International Society of Offshore and Polar Engineers*, 2016.

[30] Kim Ronny Elstad. Effekt av ionesputtering og kjemisk mekanisk polering på kvantifisering av restaustenitt i SMSS ved EBSD og XRD. Specialization project, Department of Materials Science and Engineering, NTNU, December 2015.

[31] G.L. Wynick and C.J. Boehlert. Use of Electropolishing for Enhanced Metallic Specimen Preparation for Electron Backscatter Diffraction Analysis. *Materials Characterization*, 55(3):190 – 202, 2005.

[32] Struers. *Oxide Polishing Suspensions for Your Final Polishing Needs.* Struers.

[33] Yingda Yu, Torkjell Breivik, L.A. Marken, and Jarle Hjelen. EMC 2016.

[34] Kim Ronny Elstad, Rene de Kloe, Yingda Yu, Morten Karlsen, Ida Westermann, Torkjell Breivik, and Jarle Hjelen. EBSD Characterization of Sigma Phase in SDSS by ROI Extraction and Optimization of Hough Parameters. SCANDEM - The Nordic Microscopy Society, 2016.

[35] Rene de Kloe. Personal Communication.

[36] T. Karthikeyan, M.K. Dash, S. Saroja, and M. Vijayalakshmi. Evaluation of Misindexing of EBSD Patterns in a Ferritic Steel. *Journal of Microscopy*, 249:26–35, 2013.

[37] Randi Mørkved. In-situ undersøkelser i SEM av anisotrope Al-legeringer. - Teksturutvikling, kornrotasjoner og slipaktivitet. Master's thesis, Norwegian University of Science and Technology (NTNU), 2005.

[38] J Michalska and B Chmiela. Phase Analysis in Duplex Stainless Steel: Comparison of EBSD and Quantitative Metallography Methods. In *IOP Conference Series: Materials Science and Engineering*, volume 55, page 012010. IOP Publishing, 2014.

A Characterization of the material

A.1 Table with phase distribution and confidence index

Table A.1: Phase distribution and confidence index for the different times at 850 °C.

Time [min]	Phase	CI	Ferrite [vol.%]	Austenite [vol.%]	Sigma [vol.%]
6	$\alpha + \gamma + \sigma$	0.91	54.0	45.9	0
	σ	0.01			
12	$\alpha + \gamma + \sigma$	0.91	52.0	47,7	0.3
	σ	0.18			
15	$\alpha + \gamma + \sigma$	0.86	44.6	51.0	4.5
	σ	0.37			
22	$\alpha + \gamma + \sigma$	0.82	33.2	57.1	9.5
	σ	0.43			
30	$\alpha + \gamma + \sigma$	0.51	32.7	58.3	9.1
	σ	0.12			
45	$\alpha + \gamma + \sigma$	0.69	16.9	62.9	20.3
	σ	0.23			
60	$\alpha + \gamma + \sigma$	0.69	0.60	68.4	25.5
	σ	0.36			

A.2 Sample Preparation, IQ maps

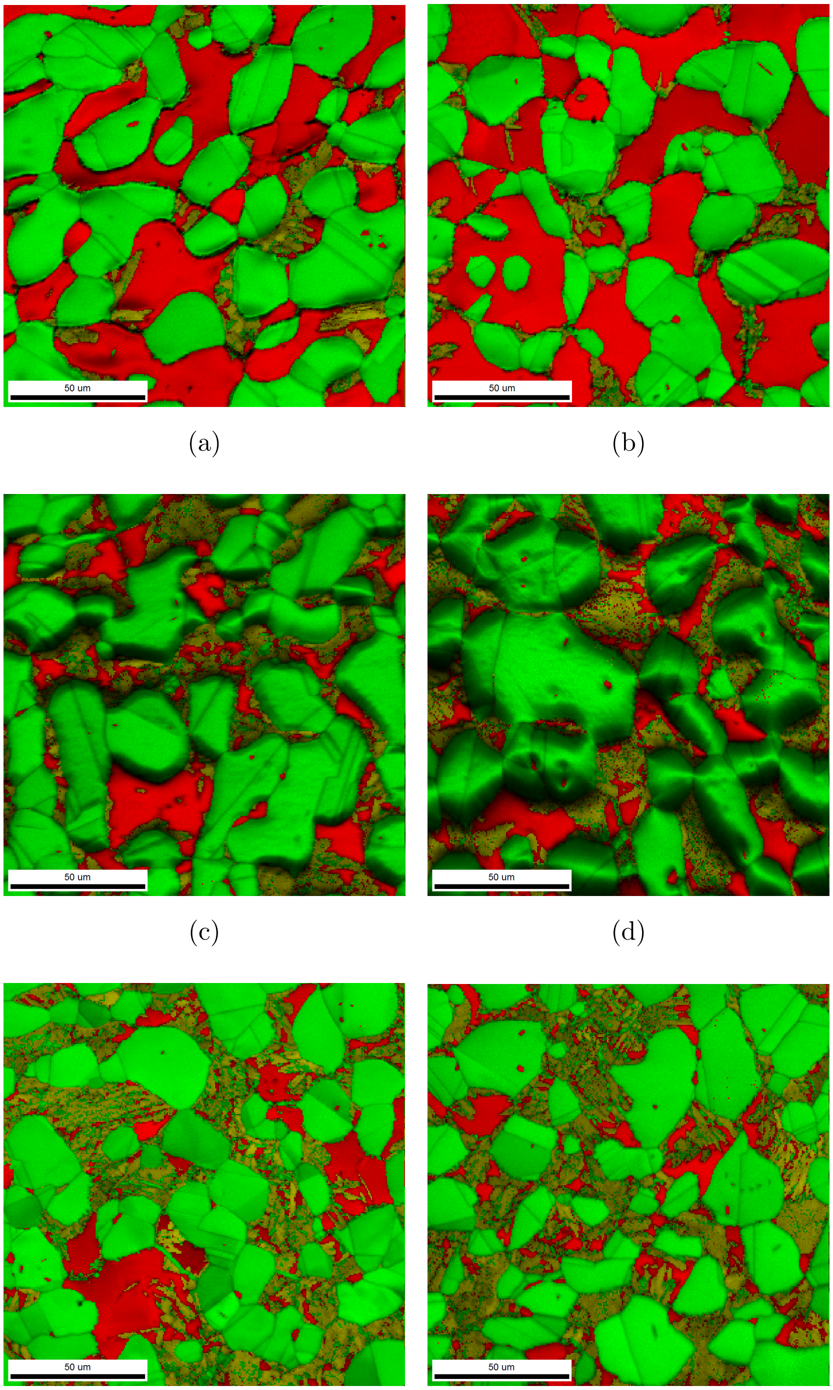

(a) (b)

(c) (d)

(e) (f)

Figure A.1: IQ maps for (a) A2, (b) A3, (c) OP-S 3 minutes, (d) OP-S 9 minutes, (e) OP-U 3 minutes, (f) OP-U 9 minutes.

B In-Situ Tensile Testing

B.1 IPF raw maps of the base material

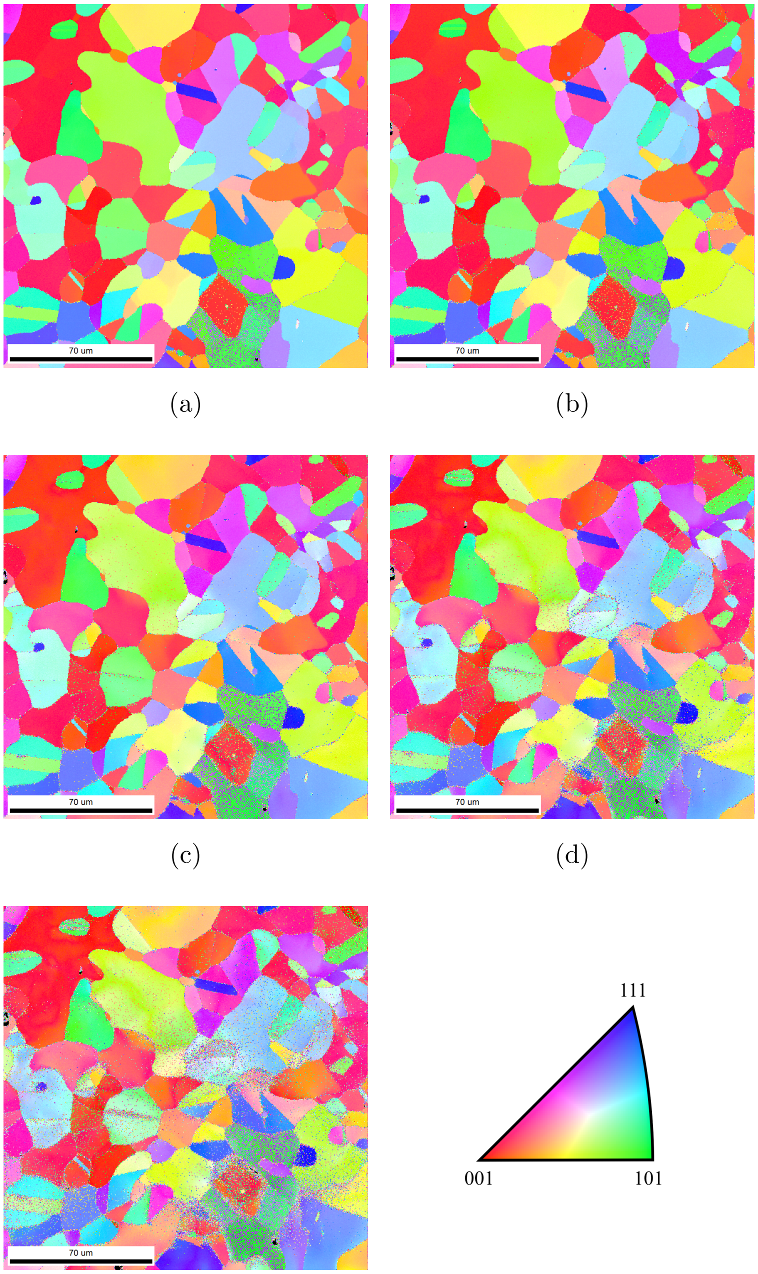

(a) (b)

(c) (d)

(e) (f)

Figure B.1: IPF maps of the base material with increasing strain where (a) 0 %, (b) 2 %, (c) 4 %, (d) 6 %, (e) 8 %.

B.2 IPF maps after 14 minutes

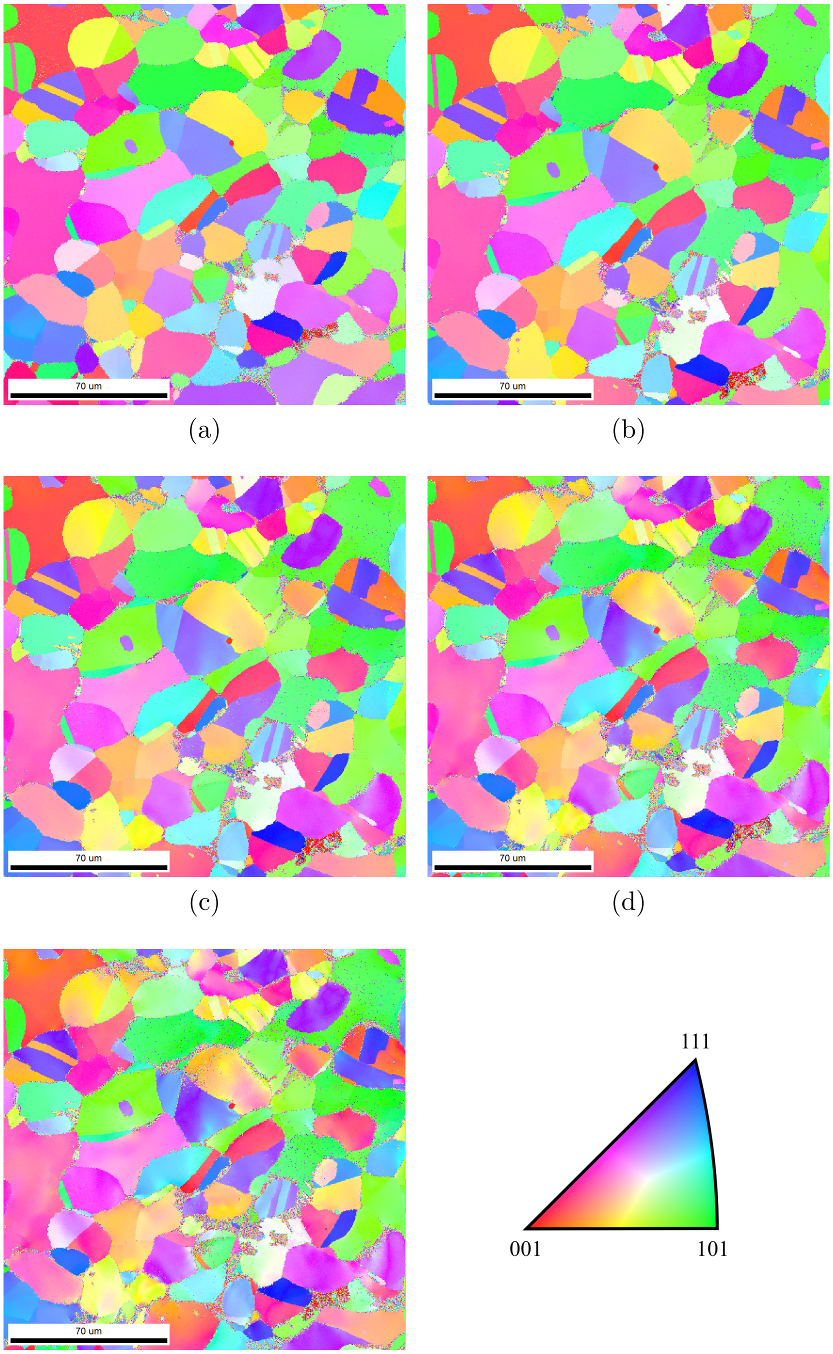

(a) (b)

(c) (d)

(e) (f)

Figure B.2: IPF maps of the material annealed for 14 minutes containing approximately 3 vol.% sigma with increasing strain where (a) 0 %, (b) 2 %, (c) 4 %, (d) 6 %, (e) 8 % and the legend is given in (f).

B.3 IPF maps after 17 minutes

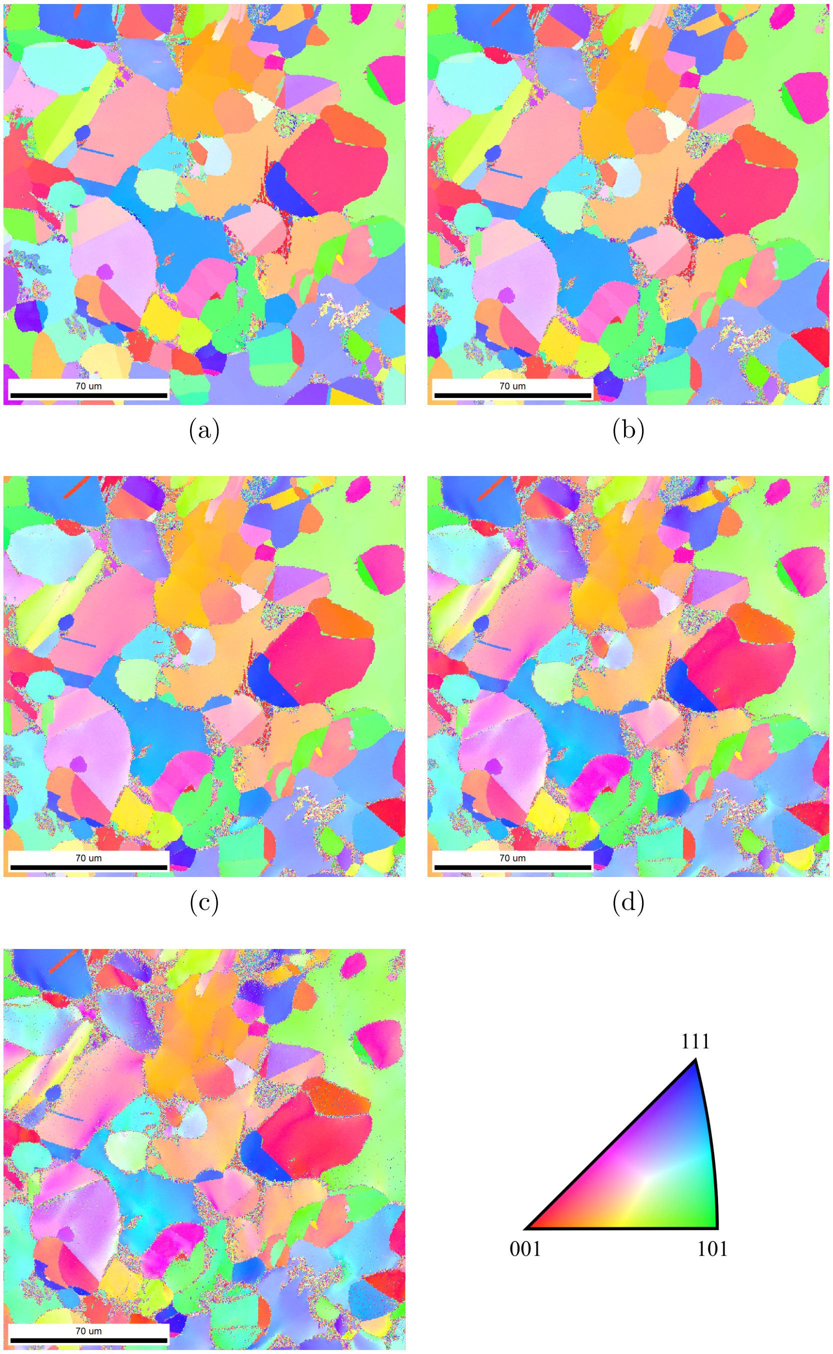

(a) (b)

(c) (d)

(e) (f)

Figure B.3: IPF maps of the material annealed for 17 minutes containing approximately 6 vol.% sigma with increasing strain where (a) 0 %, (b) 2 %, (c) 4 %, (d) 6 %, (e) 8 % and the legend is given in (f).

B.4 IPF maps after 20 minutes

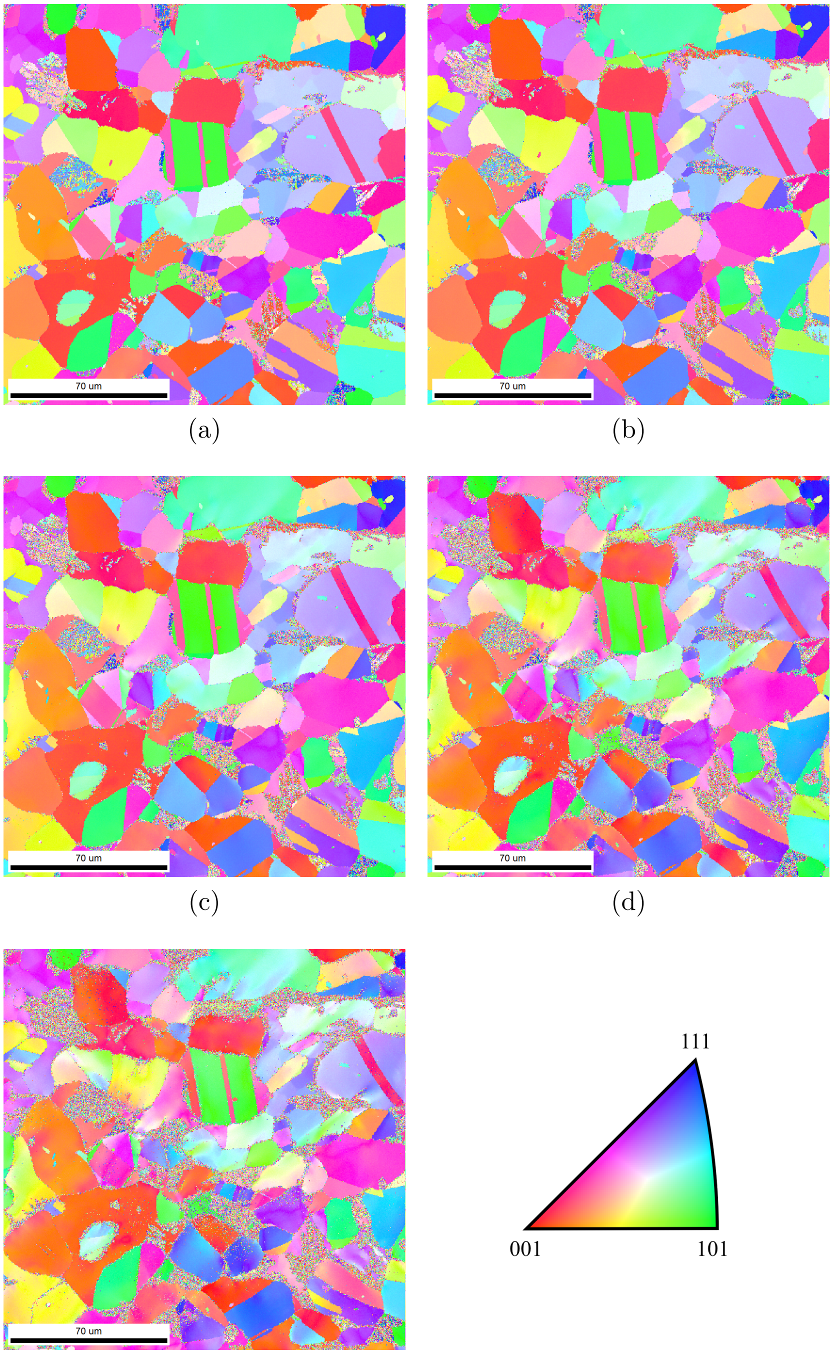

(a) (b) (c) (d) (e) (f)

Figure B.4: IPF maps of the material annealed for 20 minutes containing approximately 9 vol.% sigma with increasing strain where (a) 0 %, (b) 2 %, (c) 4 %, (d) 6 %, (e) 8 % and the legend is given in (f).

B.5 IQ maps after 14 minutes

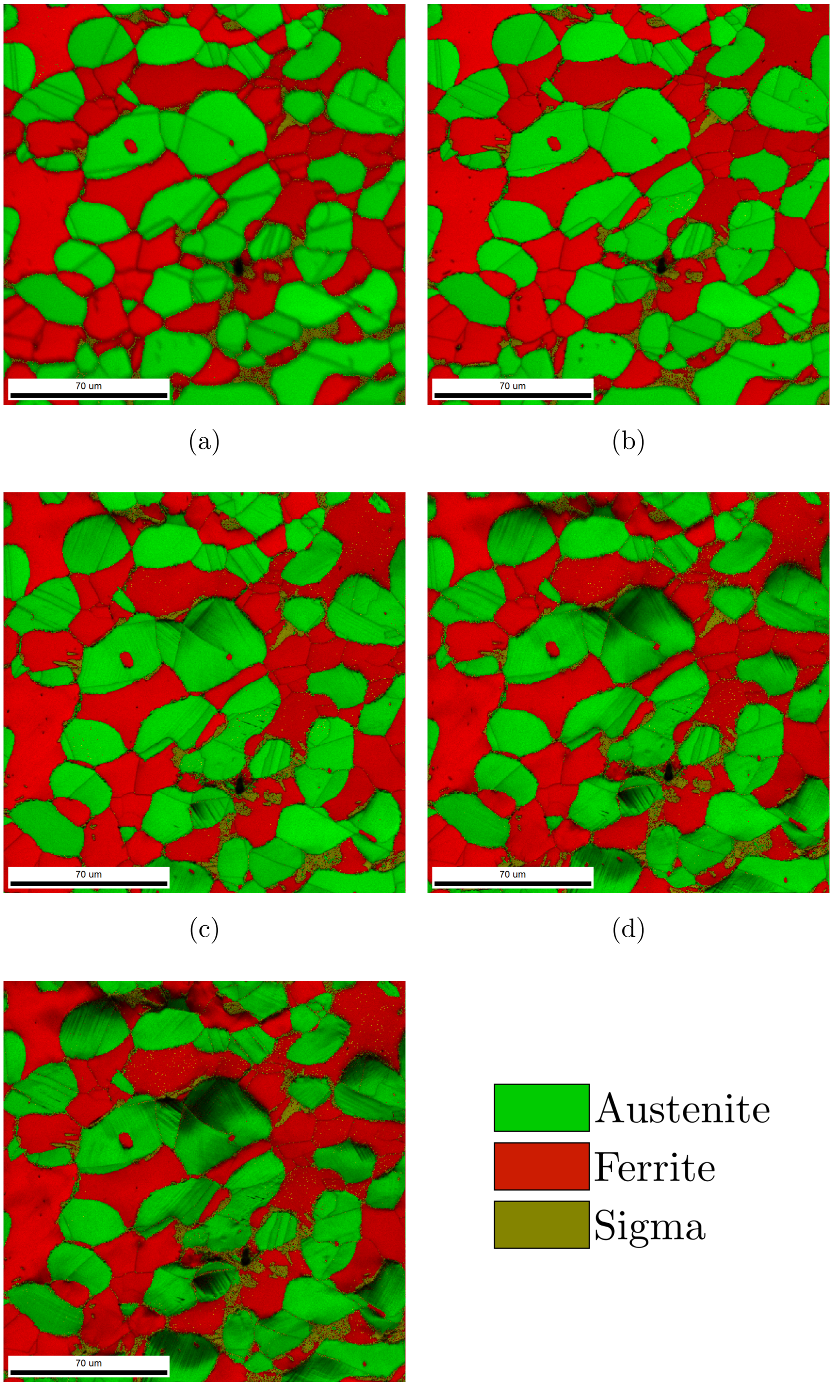

(a) (b)

(c) (d)

(e) (f)

Figure B.5: IQ maps of the material annealed for 14 minutes containing approximately 3 vol.% sigma with increasing strain where (a) 0 %, (b) 2 %, (c) 4 %, (d) 6 %, (e) 8 % and the legend is given in (f).

B.6 IQ maps after 17 minutes

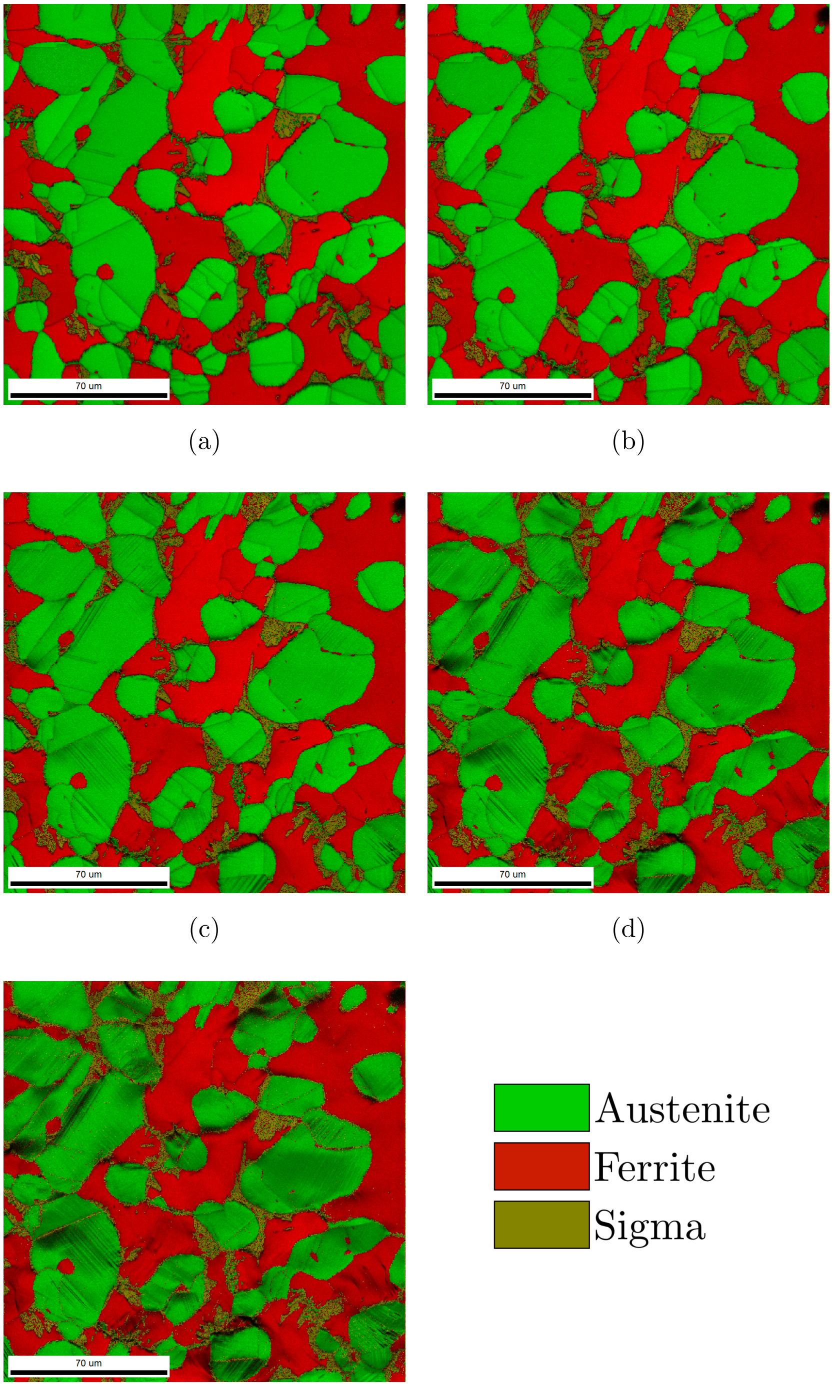

(a) (b)

(c) (d)

(e) (f)

Figure B.6: IQ maps of the material annealed for 17 minutes containing approximately 6 vol.% sigma with increasing strain where (a) 0 %, (b) 2 %, (c) 4 %, (d) 6 %, (e) 8 % and the legend is given in (f).

B.7 IQ maps after 20 minutes

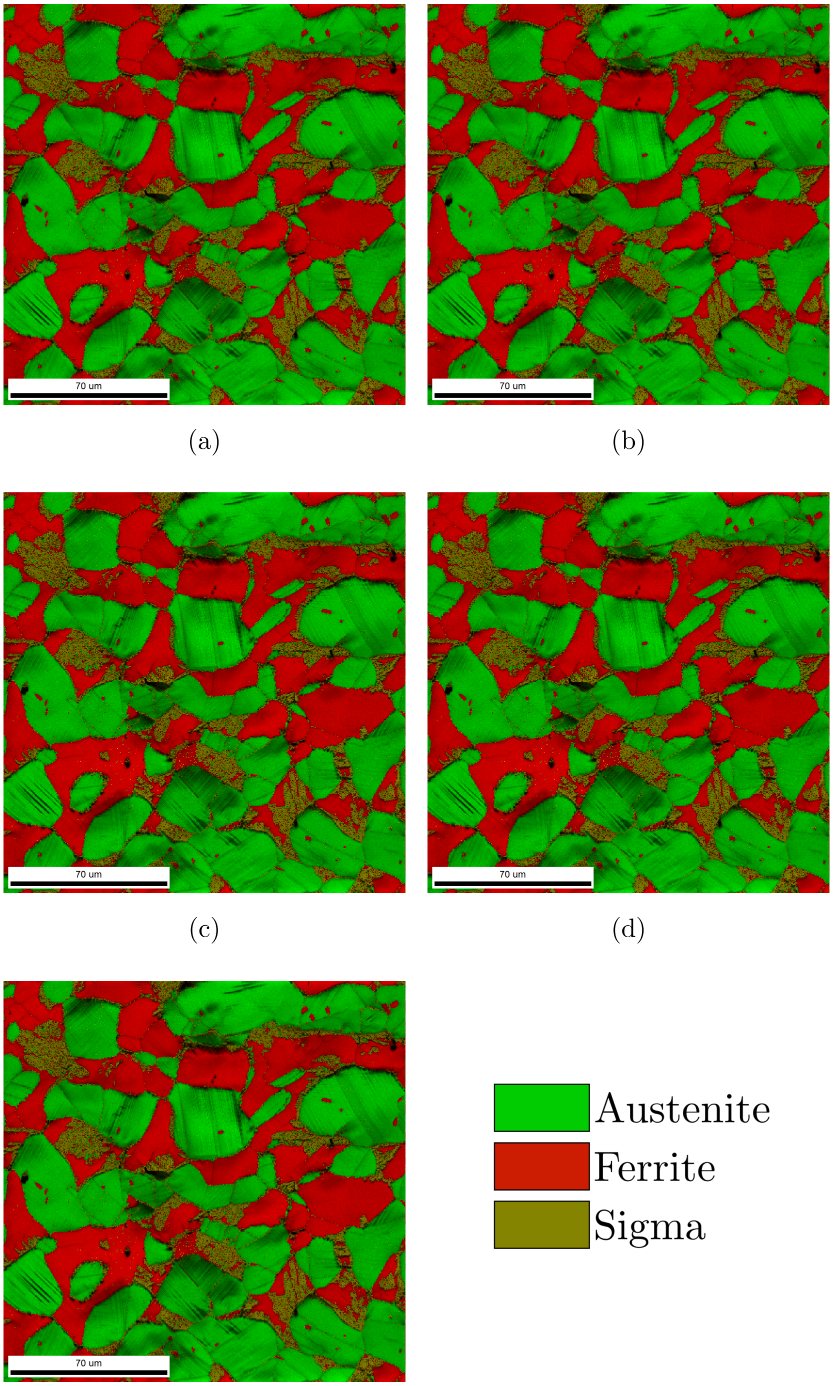

(a) (b)

(c) (d)

(e) (f)

Figure B.7: IQ maps of the material annealed for 20 minutes containing approximately 9 vol.% sigma with increasing strain where (a) 0 %, (b) 2 %, (c) 4 %, (d) 6 %, (e) 8 % and the legend is given in (f).

B.8 Stress-strain curves

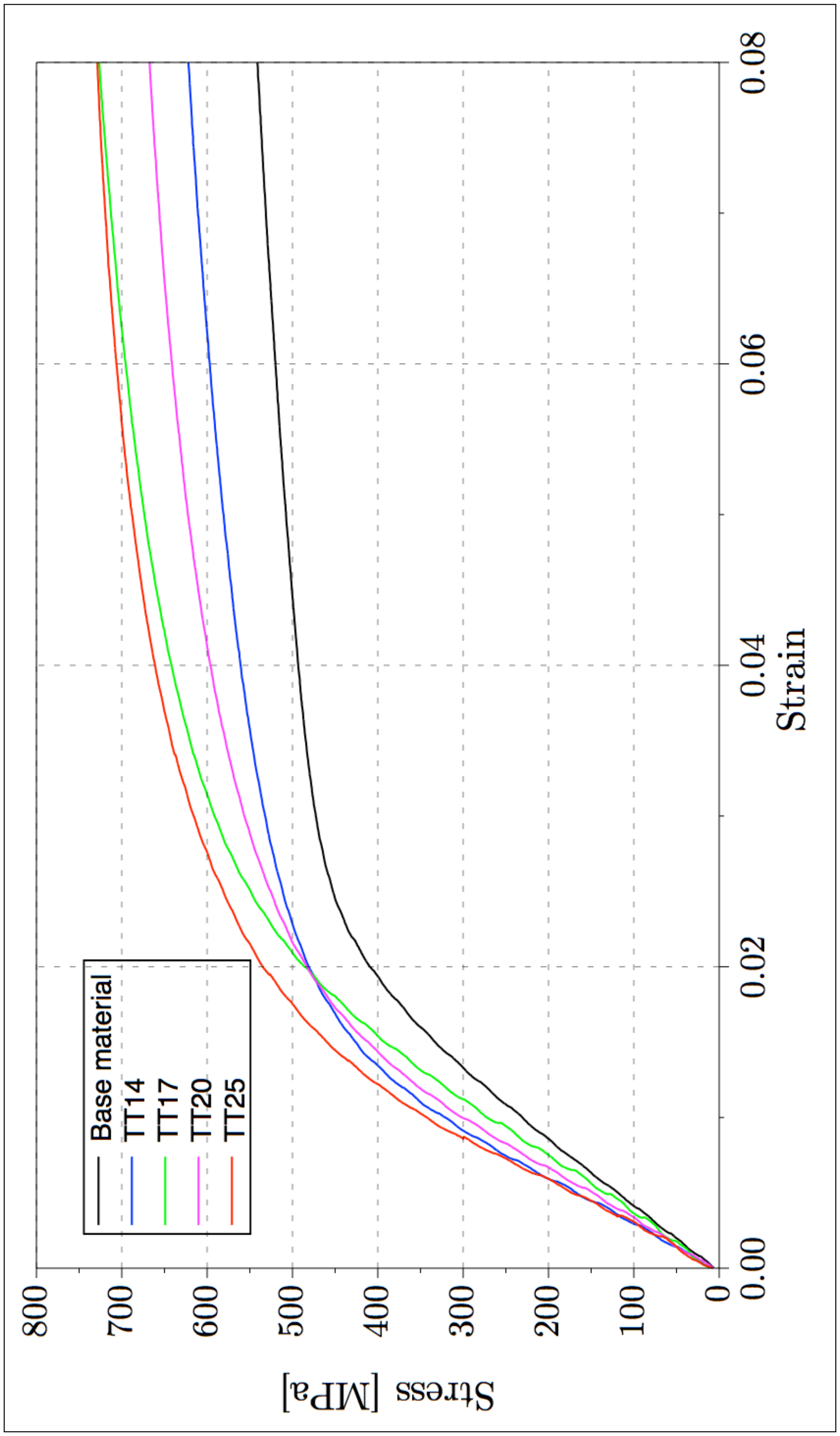

Figure B.8: Stress strain curves.

B.9 IPF maps used during rotation study

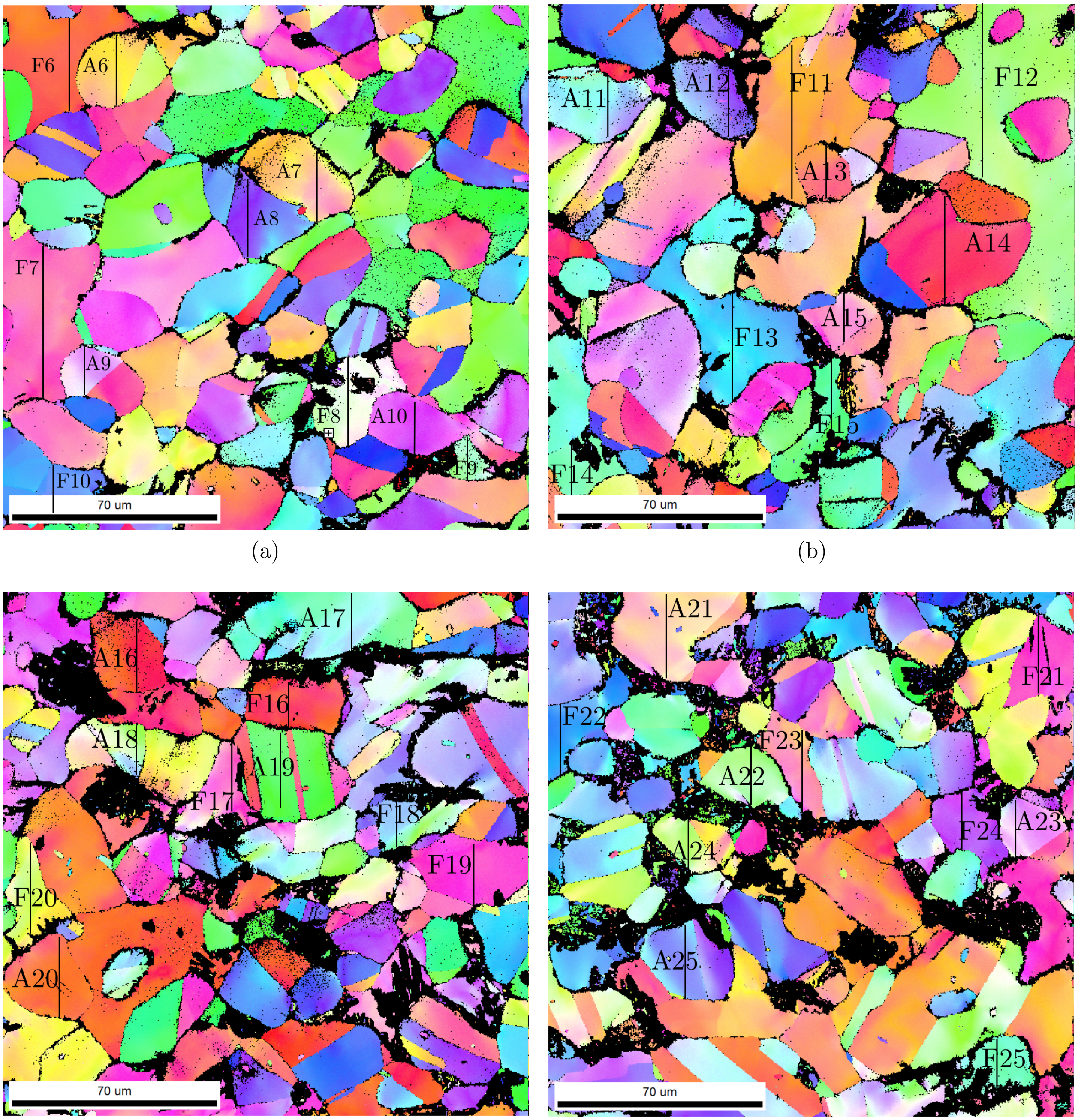

(a) (b)

(c) (d)

Figure B.9: IPF after tensile testing at 8 % strain for the different annealing times where (a) 14 minutes, (b) 17 minutes, (c) 20 minutes and (d) 25 minutes. The grains which were used in the misorientation study is marked with F and A for the ferrite and austenite, respectively.

B.10 Orientation gradients before tensile testing

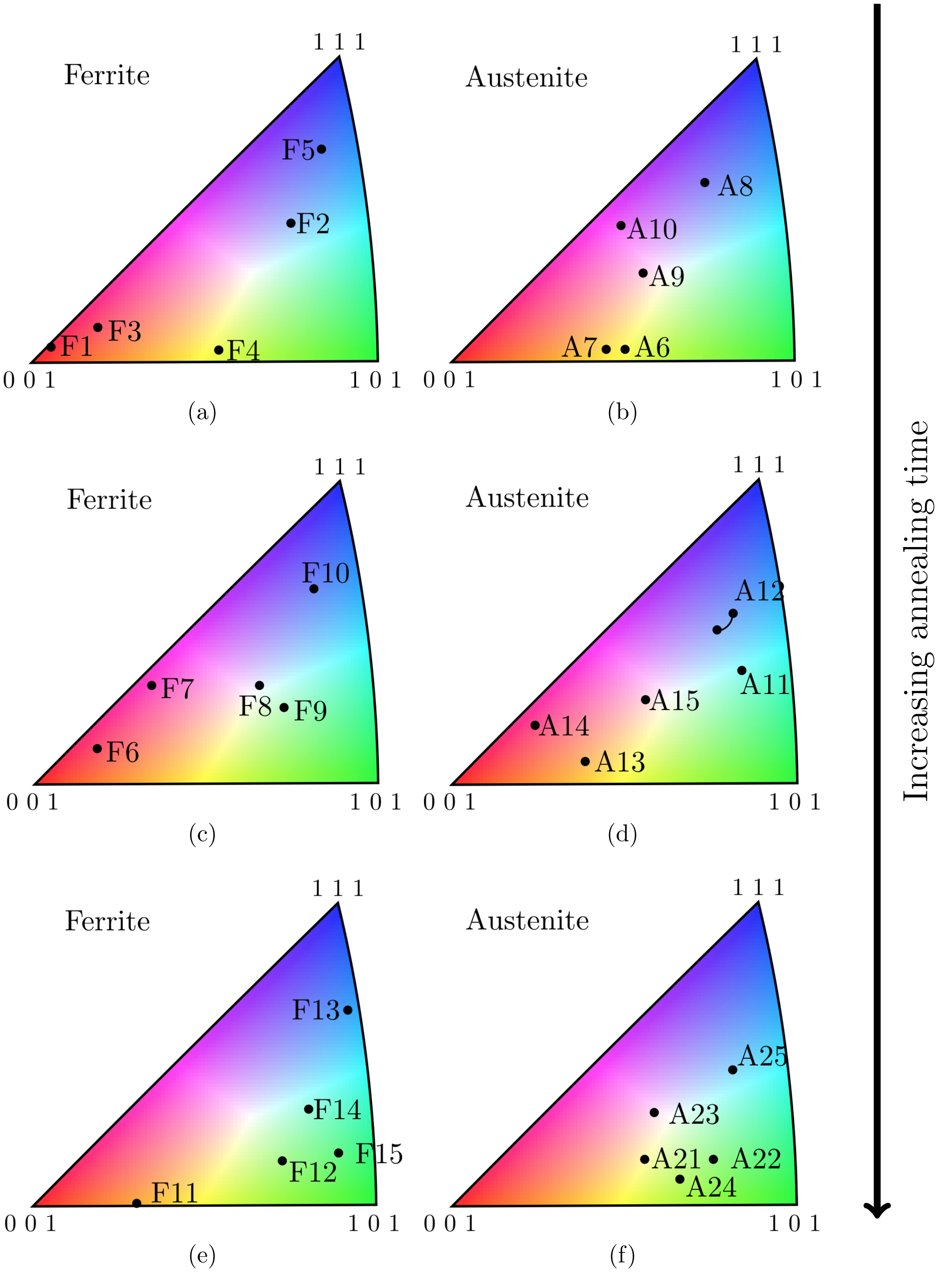

Figure B.10: Orientation inside selected grains before deformation. Ferrite and austenite grains are marked with F and A, respectively. The samples were annealed for (a) 0 minutes, (b,c) 14 minutes, (d,e) 17 minutes and (f) 25 minutes.

B.11 SEM images of surface

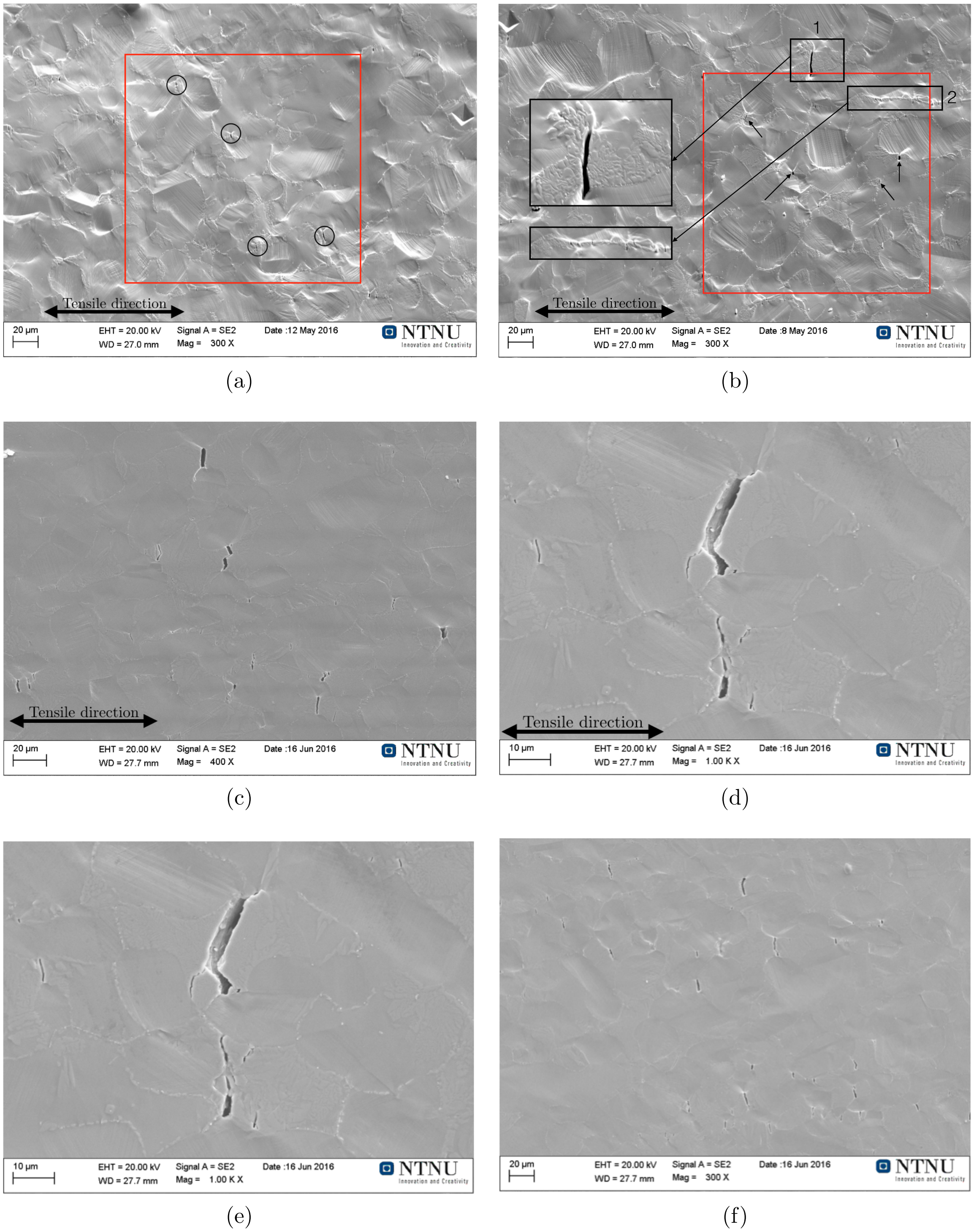

(a) (b)

(c) (d)

(e) (f)

Figure B.11: SEM images of the surface after tensile testing at 8 % strain with annealing times where (a) 17 minutes, (b) 20 minutes and (c,d,e,f) is after 25 minutes.

C Manuals

C.1 Change from sample normal to tensile direction

During the continuos EBSD mapping in this thesis the direction of interest is the tensile direction. TSL OIM Analysis automatic uses the sample normal as standard direction. To select the tensile direction, generate an IPF map. Then right click on the map and choose properties this will cause the map properties menu to appear. Then click on the edit button as shown with a red arrow in Figure C.1a.

The sample direction menu will appear as shown in Figure C.1b, which shows the different axis to choose from. The standard setting is axis 3, and axis 2 correspond to the tensile direction. There is also possible to rotate the whole specimen, but this will not be shown here.

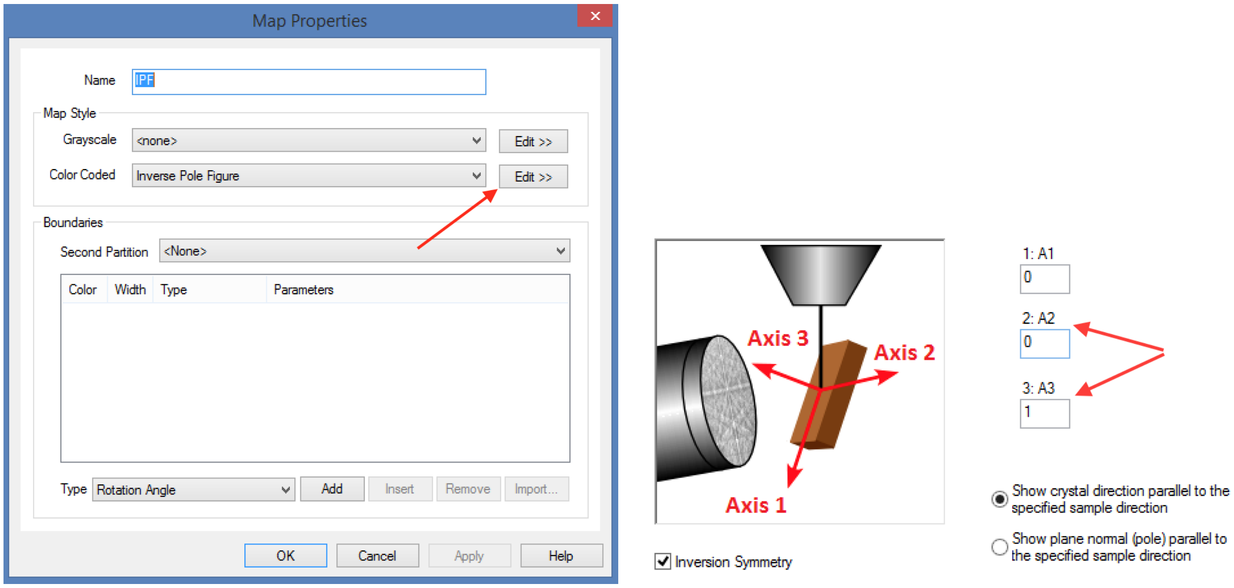

Name: IPF

Grayscale: <none>

Color Coded: Inverse Pole Figure

Second Partition: <None>

Type: Rotation Angle

1: A1: 0

2: A2: 0

3: A3: 1

● Show crystal direction parallel to the specified sample direction

○ Show plane normal (pole) parallel to the specified sample direction

☑ Inversion Symmetry

(a) (b)

Figure C.1: The map properties menu in TSL OIM Analysis.

C.2 Construction of orientation study

In this Appendix the method used to construct the grain rotation and misorientation study are presented. This methology is important since it makes the results reproducible. First the data is processed. This is done by a grain CI standardisation with a grain tolerance angle of 2 and a minimum grain size of 5. Further, a new partition is added where every point with CI less or equal to 0.05 (≤ 0.05) is removed.

To determine both the grain rotations and the orientation gradients similar procedures were used. The difference between these was that during the grain rotations a point in the middle of the grain was used with the point tool in TSL OIM Analysis, while with the orientation gradients the profile vector is used. This allowed a line to be mapped through the grain. The following steps were used to create the orientation study:

- Create an IPF map with the desired direction of interest (see Appendix C.1).
- Right click, navigate to ”Show” and enable ”Show highlighting”.
- Use either the point tool or the profile vector dependent on what information that is of interest and select the point/points desired.
- These points is further exported to a new partition or dataset. When right clicking on the map and navigating to ”Send point to” multiple options appear. With this either highlighted point, or non-highlighted points may be sent to new a partition or dataset. Since it is desirable to investigate the highlighted points select either send highlighted points to partition or dataset, respectively.

C.3 NORDIF extraction software

The NORDIF Extraction software is a new developed software with state of the art technology for supplement during characterisation and optimisation of EBSD scans. With NORDIF Extraction single patterns can be extracted, extract a new ROI or thin the files which will increase the step size and decrease the Pattern.dat file size. The multiple functions of NORDIF Extraction is are given in the following sub sections where the common step for every function is the loading of the scan. In this manual the NORDIF Extraction software version 1.0.14 is used.

C.3.1 Loading of the file

To load your file, click the file tab on the top left corner and choose "Open" and the following menu appears, see Figure C.2.

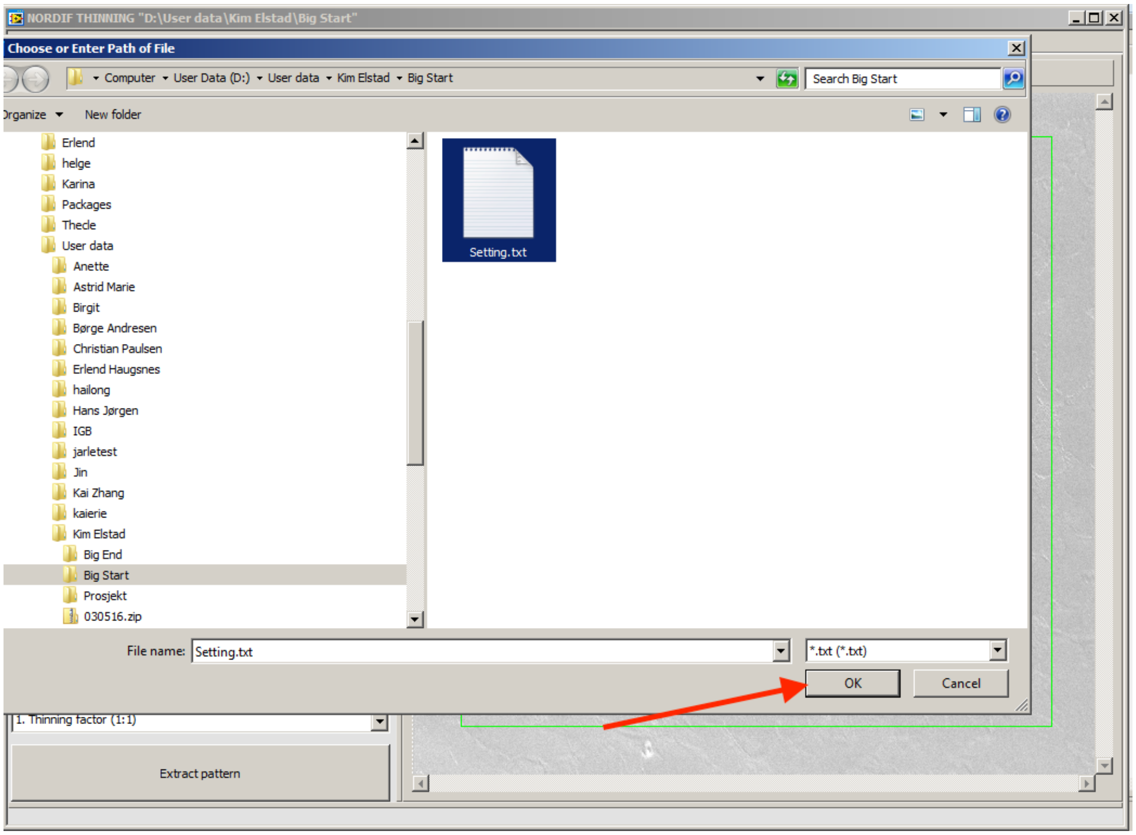
NORDIF THINNING "D:\User data\Kim Elstad\Big Start"

Choose or Enter Path of File

Computer ▸ User Data (D:) ▸ User data ▸ Kim Elstad ▸ Big Start

File name: Setting.txt

.txt (.txt)

1. Thinning factor (1:1)

Figure C.2: Loading of file.

Navigate to the folder of interest and choose the setting file, usually named Setting.txt. Then press ”Ok” and the file is loaded to the program which will cause the following to appear.

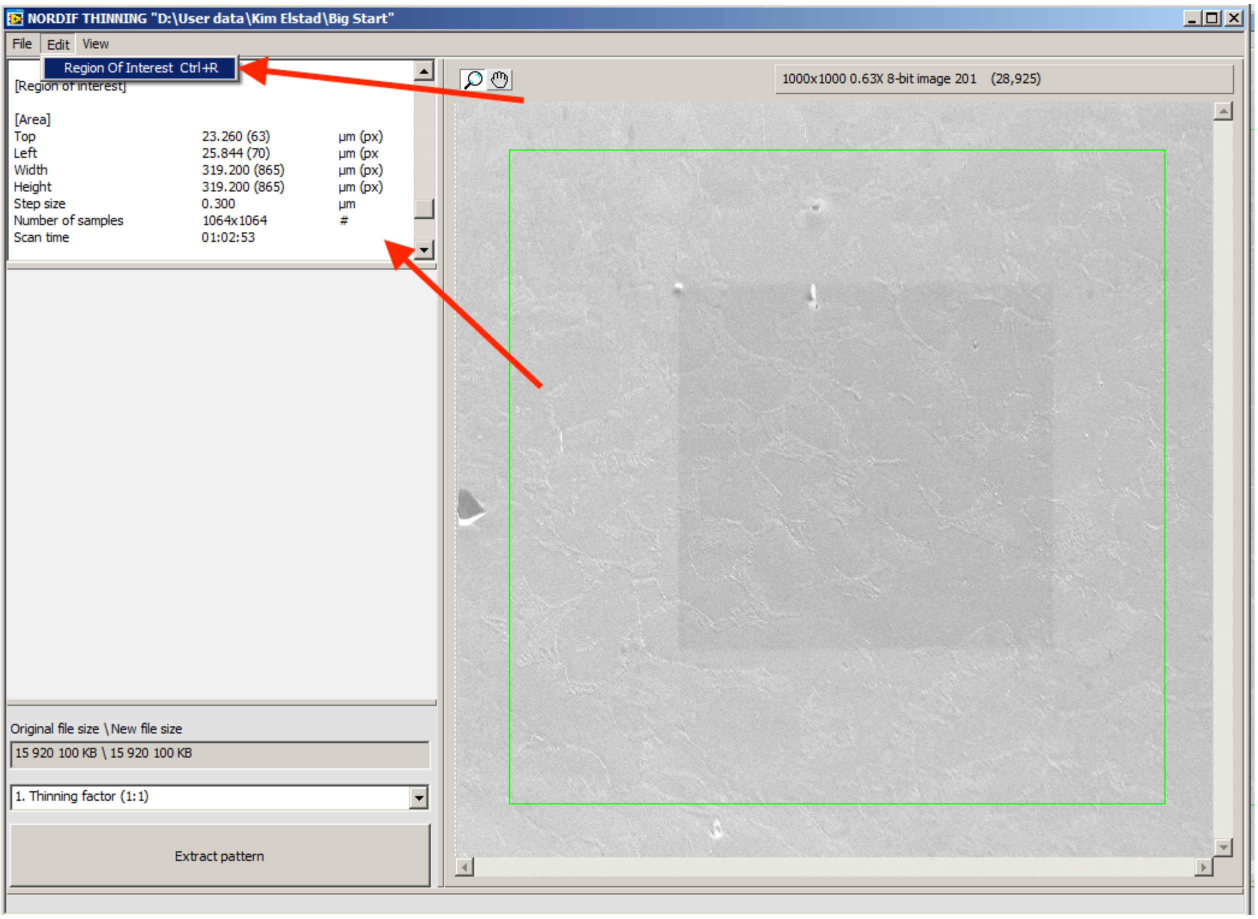

```
[Region of interest]

[Area]
Top                  23.260 (63)     µm (px)
Left                 25.844 (70)     µm (px
Width                319.200 (865)   µm (px)
Height               319.200 (865)   µm (px)
Step size            0.300           µm
Number of samples    1064x1064       #
Scan time            01:02:53
```

Original file size \ New file size
15 920 100 KB \ 15 920 100 KB

1. Thinning factor (1:1)

1000x1000 0.63X 8-bit image 201 (28,925)

Figure C.3: Loaded file showing setting and electron image.

Figure C.3 shows the loaded file in the extraction software. On the left hand side, the information from the setting file is given. When pressing the edit tab, the ”Region of Interest” button appears. Enabling this will show only the ROI and not the whole electron image. This allows more functions to be displayed, see Figure C.4.

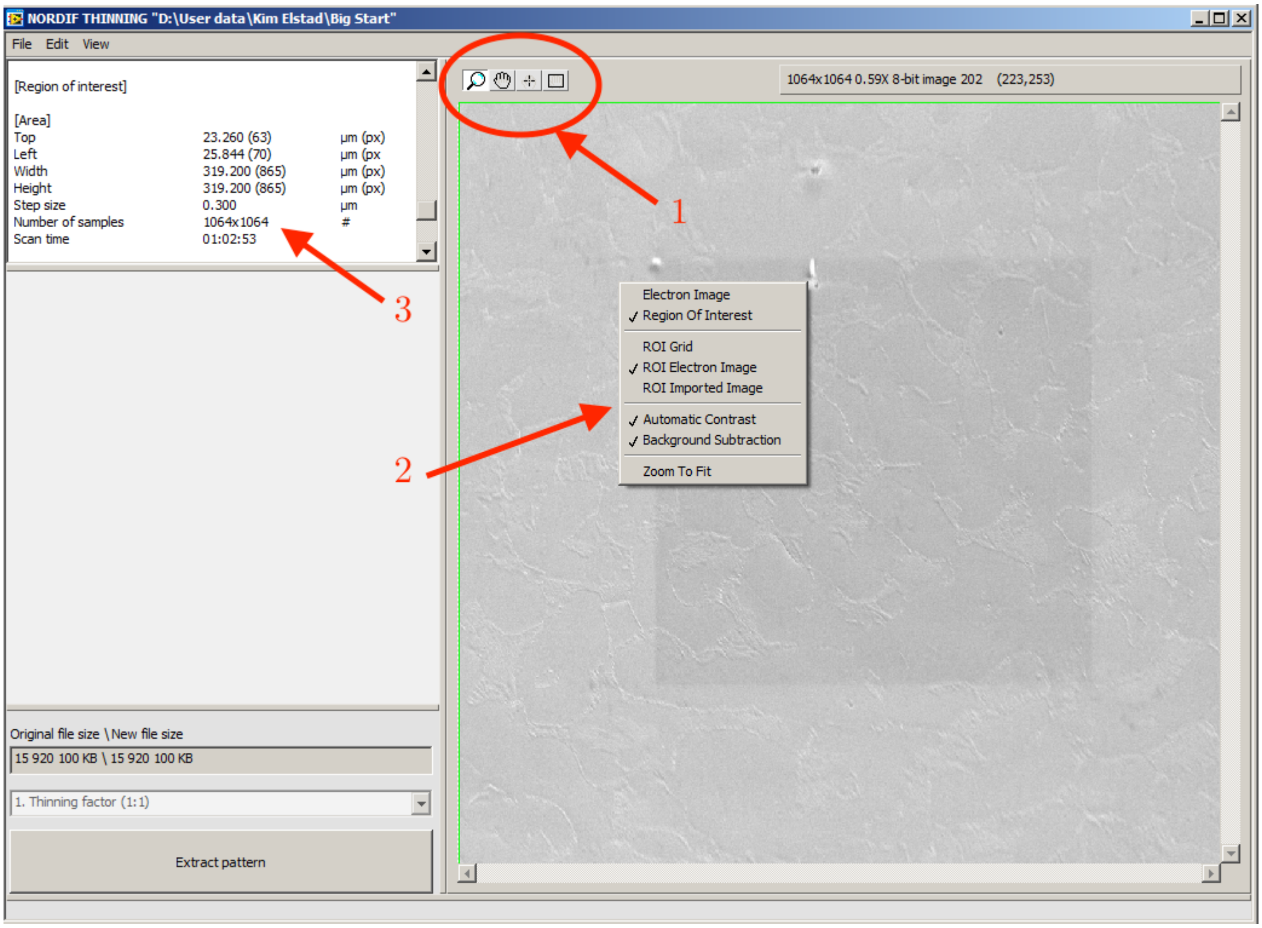

```
[Region of interest]

[Area]
Top                 23.260 (63)      µm (px)
Left                25.844 (70)      µm (px
Width               319.200 (865)    µm (px)
Height              319.200 (865)    µm (px)
Step size           0.300            µm
Number of samples   1064x1064        #
Scan time           01:02:53
```

Original file size \ New file size: 15 920 100 KB \ 15 920 100 KB

1. Thinning factor (1:1)

Figure C.4: Showing ROI with the new functions.

Arrow 1 shows the new functions, which is recognised from the NORDIF EBSD acquisition software. The ”+” open the possibility of investigating single patterns, see section C.3.3, and the rectangle open the possibility of extracting a sub ROI, see section C.3.4. When right clicking on the electron image, more options appear, see arrow 2. When choosing ”ROI Imported Image”, an EBSD map, i.e. phase map, image quality map, inverse pole figure map, etc. can be loaded. It is of great importance that the size of this map corresponds to the number of samples, see arrow 3.

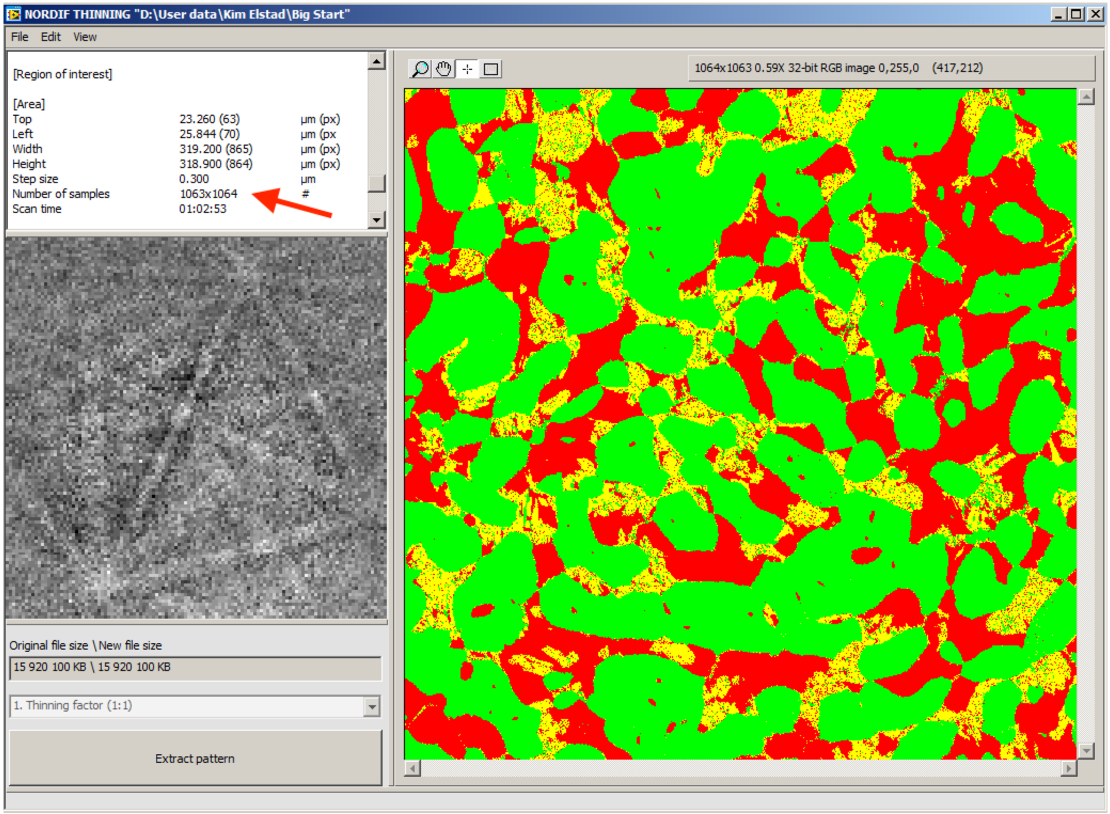

```
[Region of interest]

[Area]
Top                  23.260 (63)      µm (px)
Left                 25.844 (70)      µm (px
Width                319.200 (865)    µm (px)
Height               318.900 (864)    µm (px)
Step size            0.300            µm
Number of samples    1063x1064        #
Scan time            01:02:53
```

1064x1063 0.59X 32-bit RGB image 0,255,0 (417,212)

Original file size \ New file size

15 920 100 KB \ 15 920 100 KB

1. Thinning factor (1:1)

Figure C.5: Loaded pattern instead of electron image.

In Figure C.5 above a phase map is imported in to NORDIF Extraction. The red arrow show that there was need for an adjustment in the setting since the NORDIF Extraction and the TSL OIM Analysis does not calculate the pixels the same way. This will be fixed in the following versions of the software. Temporary it can be solved with the following steps:

- Open TSL OIM Analysis and choose the desired map. Further, right click and choose "Image" and "Save image".
- A menu with both "Width" and "Height" appear. These values must match with the number of samples in NORDIF Extraction. If these values don't match, the Setting.txt file needs to be changed. Therefore, these values must be written down.
  - Open the Setting.txt file, and scroll down to "Number of samples". Change the sequence of these numbers so they match the values from TSL OIM Analysis. **Note: The values must be written in the opposite order, e.g. if the values are 1064 x 1063, write 1063 x 1064 in the Setting.txt file and save.**

C.3.2 Thin file

Thinning the EBSD files can be very useful to speed up indexing for testing of e.g. the Hough parameters. When thinning files it is important that the "Region of Interest" is not selected, but the entire electron image. Figure C.6 shows the NORDIF Extraction window where the red arrow shows the multiple thinning factors. If choosing "3. Thinning factor (1:9)" the step size is increased by a factor 3, which in this case will be from 0.3 μm to 0.9 μm.

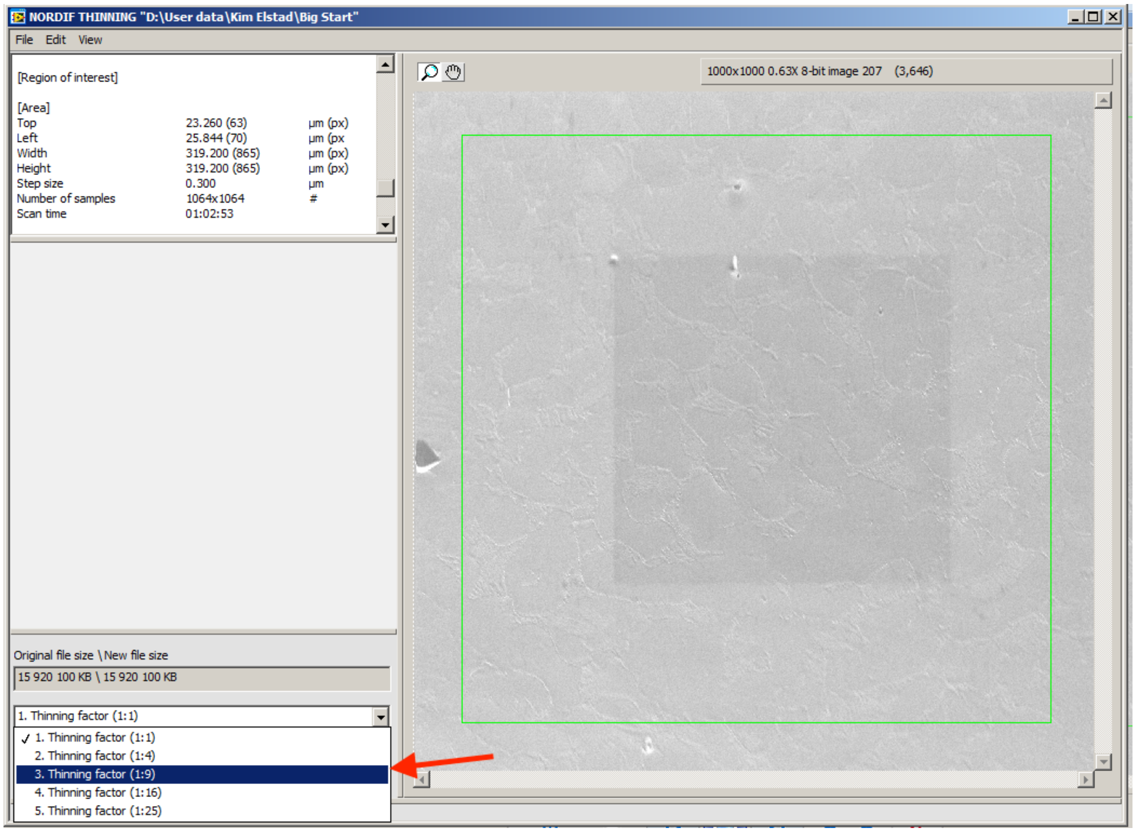

[Region of interest]

[Area]

Top	23.260 (63)	µm (px)
Left	25.844 (70)	µm (px
Width	319.200 (865)	µm (px)
Height	319.200 (865)	µm (px)
Step size	0.300	µm
Number of samples	1064x1064	#
Scan time	01:02:53	

Original file size \ New file size

15 920 100 KB \ 15 920 100 KB

1. Thinning factor (1:1)

- ✓ 1. Thinning factor (1:1)
- 2. Thinning factor (1:4)
- 3. Thinning factor (1:9)
- 4. Thinning factor (1:16)
- 5. Thinning factor (1:25)

Figure C.6: Showing the different thinning factors.

After pressing extract pattern, the following picture appears. A new sub project is created and can be found in the original folder. Arrow 1 show the new step size and arrow 2 and 3 show the original file size and new file size, respectively.

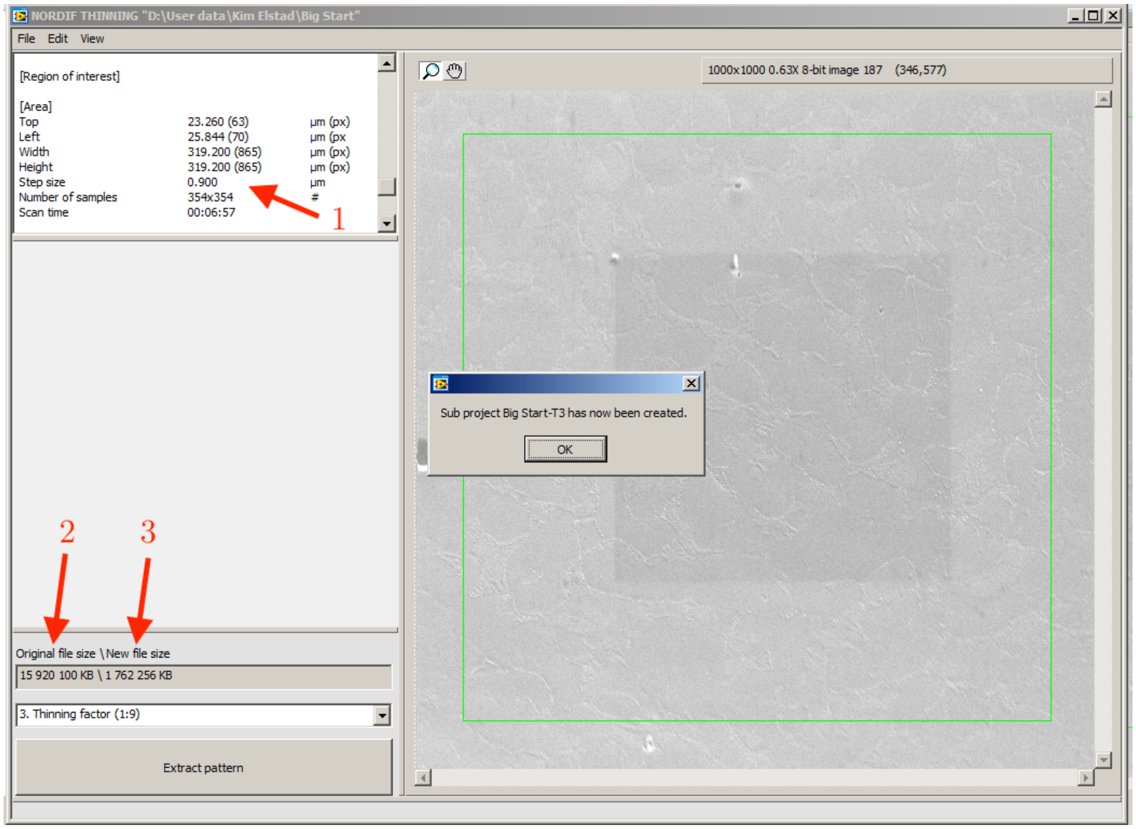
NORDIF THINNING "D:\User data\Kim Elstad\Big Start"

[Region of interest]

[Area]

Top	23.260 (63)	µm (px)
Left	25.844 (70)	µm (px
Width	319.200 (865)	µm (px)
Height	319.200 (865)	µm (px)
Step size	0.900	µm
Number of samples	354x354	#
Scan time	00:06:57	

1000x1000 0.63X 8-bit image 187 (346,577)

Sub project Big Start-T3 has now been created.

Original file size \ New file size: 15 920 100 KB \ 1 762 256 KB

3. Thinning factor (1:9)

Figure C.7: Thinned file with thin factor 3 which decreased the file size of a factor 9.

C.3.3 Extract single pattern

With NORDIF Extraction it is also possible to extract single patterns for a more thorough investigation, e.g. during optimisation of the indexing parameters. To enable the pattern extraction functions press the ”+” sign indicated by arrow 1, Figure C.8. **Note: Enable automatic contrast and background subtraction by right clicking on the electron image.** When moving the cursor around on the electron image the acquisition patterns are shown (arrow 2).

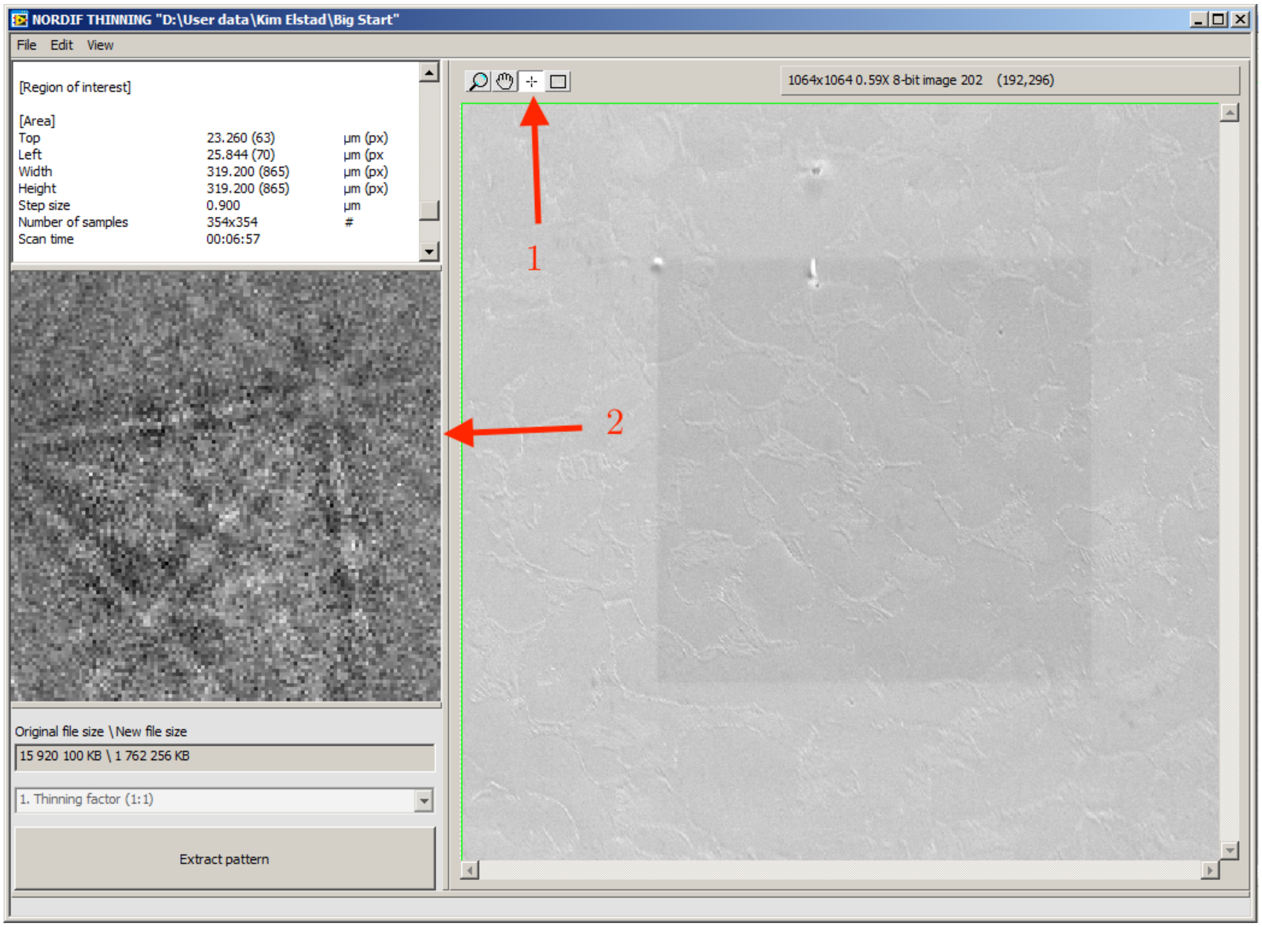

[Region of interest]

[Area]

Top	23.260 (63)	µm (px)
Left	25.844 (70)	µm (px
Width	319.200 (865)	µm (px)
Height	319.200 (865)	µm (px)
Step size	0.900	µm
Number of samples	354x354	#
Scan time	00:06:57	

Original file size \ New file size: 15 920 100 KB \ 1 762 256 KB

1. Thinning factor (1:1)

1064x1064 0.59X 8-bit image 202 (192,296)

Figure C.8: Showing the acquisition patterns which can be extracted.

When the desired pattern is found, left click to save the pattern. The following menu appears:

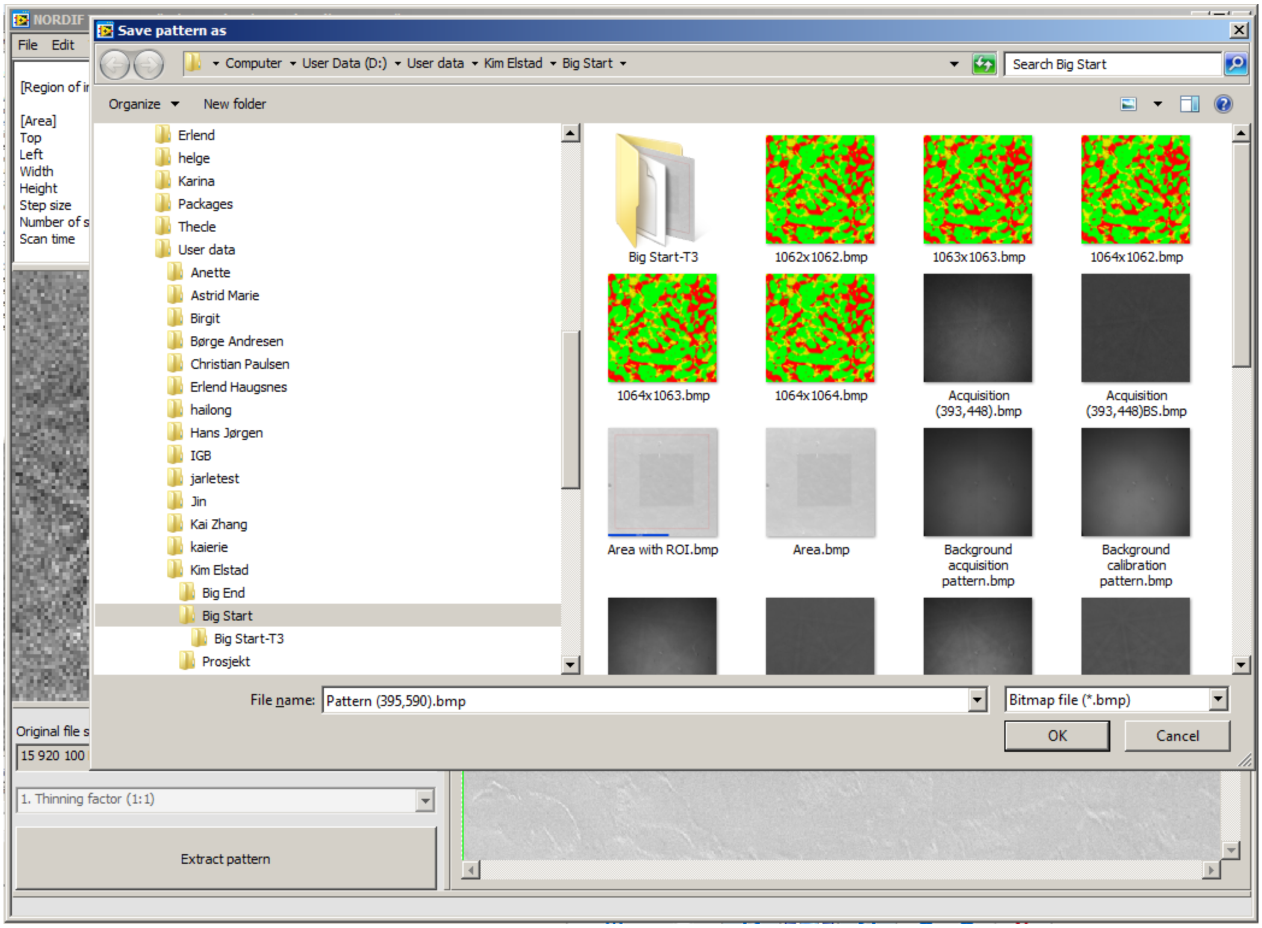
File name: Pattern (395,590).bmp

Bitmap file (*.bmp)

Figure C.9: Saving the extracted pattern.

C.3.4 Extract new ROI

With the NORDIF Extraction Software it is also possible to extract a new ROI. This is can be very helpful when you want to investigate a part of the scan, or during optimisation of parameters to check if the settings are successful. Start with a loaded file and choose a rectangle of interest, see arrow 1 in Figure C.10. The ROI is chosen the same way as in the NORDIF EBSD acquisition software (hold down left mouse button and choose the desired size).

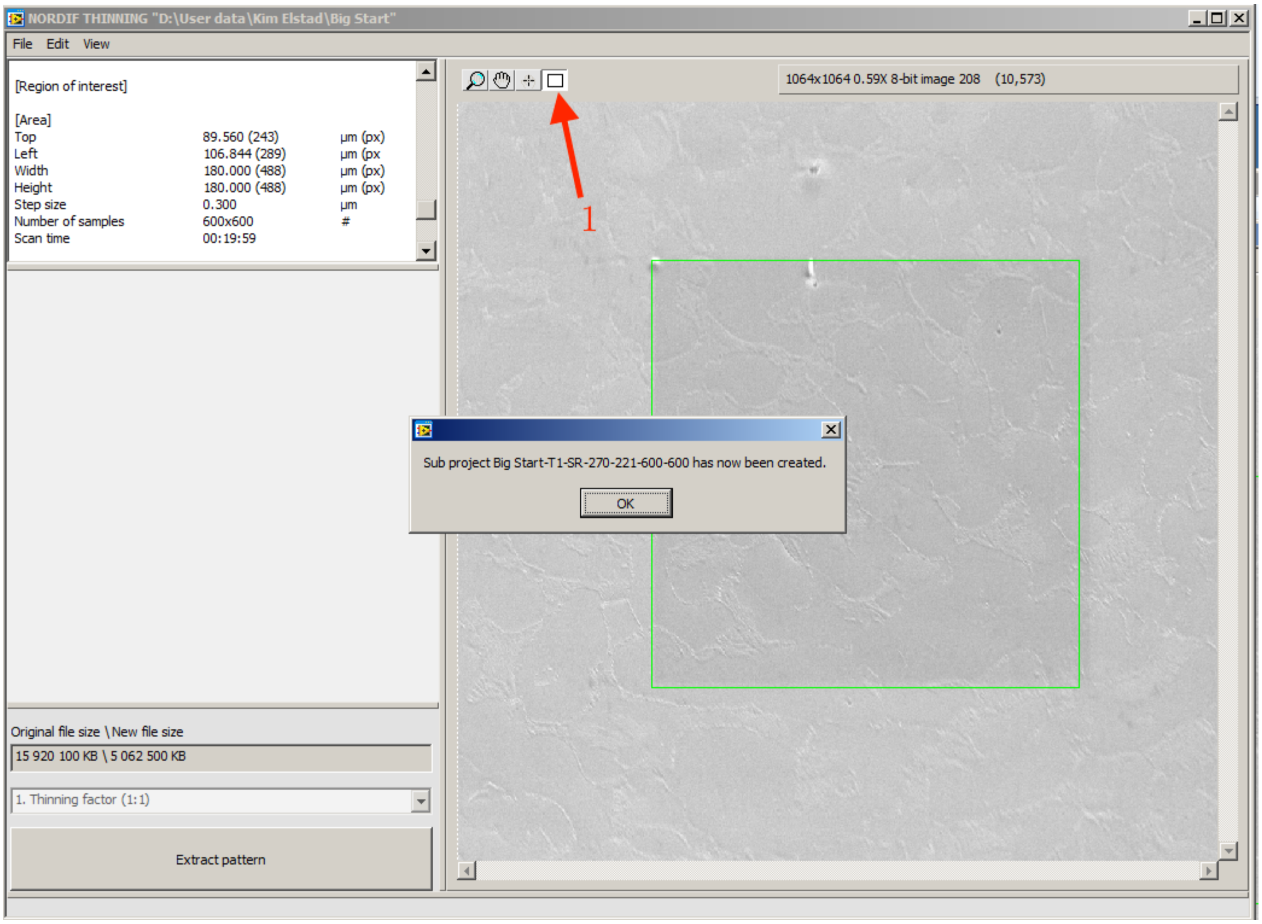

[Region of interest]

[Area]

Top	89.560 (243)	µm (px)
Left	106.844 (289)	µm (px
Width	180.000 (488)	µm (px)
Height	180.000 (488)	µm (px)
Step size	0.300	µm
Number of samples	600x600	#
Scan time	00:19:59	

Original file size \ New file size
15 920 100 KB \ 5 062 500 KB

1. Thinning factor (1:1)

Sub project Big Start-T1-SR-270-221-600-600 has now been created.

Figure C.10: Creating a new ROI.

The message in Figure C.10 appears and contains information on the new region of interest. The new folder is saved in the original folder and is named with <Original File Name-Thinning Factor-Sub ROI-Upper Left Coordinates-Width (pixels)-Height (pixels)>